UNIVERSITY OF Southampton

University of Southampton Research Repository
ePrints Soton

Copyright © and Moral Rights for this thesis are retained by the author and/or other copyright owners. A copy can be downloaded for personal non-commercial research or study, without prior permission or charge. This thesis cannot be reproduced or quoted extensively from without first obtaining permission in writing from the copyright holder/s. The content must not be changed in any way or sold commercially in any format or medium without the formal permission of the copyright holders.

When referring to this work, full bibliographic details including the author, title, awarding institution and date of the thesis must be given e.g.

AUTHOR (year of submission) "Full thesis title", University of Southampton, name of the University School or Department, PhD Thesis, pagination

http://eprints.soton.ac.uk

UNIVERSITY OF SOUTHAMPTON

Optically Nonlinear Spatial and Spectral Processes in Semiconductor Microcavities

by

Alastair J. D. Grundy

A thesis submitted in partial fulfillment for the degree of Doctor of Philosophy

in the

Faculty of Engineering, Science and Mathematics

School of Physics and Astronomy

March 2009

UNIVERSITY OF SOUTHAMPTON

ABSTRACT

FACULTY OF ENGINEERING, SCIENCE AND MATHEMATICS

SCHOOL OF PHYSICS AND ASTRONOMY

Doctor of Philosophy

Optically Nonlinear Spatial and Spectral Processes in Semiconductor Microcavities

by Alastair J. D. Grundy

This thesis presents experimental analysis of polariton dynamics in semiconductor microcavities. A microcavity is a monolithic structure composed of two distributed Bragg reflectors which are separated by a layer of active material. Strong coupling between excitons residing in the active layer and photons confined within the cavity leads to new eigenstates of the system, called microcavity exciton-polaritons. The dynamics of these quasi-bosons are studied using a range of optical spectroscopy techniques.

It has been shown previously that resonant injection of polaritons using a continuous wave laser allows the microcavity to operate as an optical parametric oscillator. A full study of the recovery dynamics of a transiently destabilized microcavity optical parametric oscillator is made in this thesis. Destabilization was achieved by optically injecting surplus polaritons into a system that had reached equilibrium. The dynamics of the scattering processes is theoretically described using a rate equation model.

Bose condensation and polariton lasing have recently been demonstrated at liquid helium temperatures. In this thesis, we use a hybrid bulk gallium nitride microcavity to demonstrate the operation of the first room temperature polariton laser. Polarisation measurements also show spontaneous symmetry breaking, implying observation of the first room temperature Bose-Einstein condensate.

For my wife, who offered me unconditional love and support during the course of this thesis.

Contents

List of Figures

List of Tables

DECLARATION OF AUTHORSHIP

I, Alastair James Daniel Grundy, declare that the thesis entitled 'Optically Nonlinear Spatial and Spectral Processes in Semiconductor Microcavities' and the work presented in the thesis are both my own, and have been generated by me as the result of my own original research. I confirm that:

- this work was done wholly or mainly while in candidature for a research degree at this University;
- where any part of this thesis has been previously submitted for a degree or any other qualification at this University or any other institution, this has been clearly stated;
- where I have consulted the published work of others, the source is always given. With the exception of such quotations, this thesis is entirely my own work;
- I have acknowledged all main sources of help
- where the thesis is based on work done by myself jointly with others, I have made clear exactly what was done by others and what I have contributed myself;
- parts of this work have been published, the details of which are given overleaf;

Signed:

Date:

LIST OF PUBLICATIONS

J. J. Baumberg, A. K. Kavokin, S. G. Christopoulos, A. J. D. Grundy, R. Butte,G. Christman, D. D. Solnyshkov, G. Malpuech, G. Baldassarri Hoger von Hogersthal, J. F. Feltin, and N. Grandjean. **Spontaneous polarisation build up in a room temperature polariton laser.** *Physical Review Letters*, 101:136409, 2008.

R. Butte, J. F. Carlin, E. Feltin, M. Gonschorek, S. Nicolay, G. Christmann, D. Simeonov, A. Castiglia, J. Dorsaz, H. J. Buehlmann, S. Christopoulos, G. Baldassarri Hoeger von Hoegersthal, A. J. D. Grundy, M. Mosca, C. Pinquier, M. A. Py, F. Demangeot, J. Frandon, P.G. Lagoudakis, J. J. Baumberg, N. Grandjean. **Current status of AlInN layers lattice-matched to GaN for photonics and electronics.** *Journal of Physics D - Applied Physcics*, 40:6328, 2007.

E. Feltin, G. Christmann, J. Dorsaz, A. Castiglia, J. F. Carlin, R. Butte, N. Grandjean, S. Christopoulos G. Baldassarri Hoeger von Hogersthal, A. J. D. Grundy, P. G. Lagoudakis, J. J. Baumberg. **Blue lasing at room temperature in an optically pumped lattice-matched AlInN/GaN VCSEL structure.** *Electronics Letters*, 43:924, 2007.

S. Christopoulos, G. Baldassarri Hoger von Hogersthal, A. J. D. Grundy, P. G. Lagoudakis, A. V. Kavokin, J. J. Baumberg, G. Christmann, R. Butte, E. Feltin, J. F. Carlin, N. Grandjean. **Room-temperature polariton lasing in semiconductor microcavities.** *Physical Review Letters*, 98:126405, 2007.

G. Baldassarri Hoger von Hogersthal, A. J. D. Grundy, J. J. Baumberg, D. Sanvitto, M. Skolnick. **Polariton spin dynamics in III-V semiconductor microcavities.** *Physica Status Solidi C*, 11:3864, 2005.

Acknowledgements

I would like to thank my supervisor Prof. Jeremy Baumberg for providing a superbly equipped laboratory and allowing me the freedom to learn through experience. His inexhaustible supply of energy and passion for science have been an inspiration to me. I would also like to thank Prof. Richard Harley for his continued advice and support.

Particular thanks go to Giorgio Baldassarri, with whom I spent many long nights in the lab, for his superb scientific guidance and fantastic renditions of some classic Frank Sinatra songs. It has also been a pleasure to work alongside Stavros Christopoulos. I have fond memories of a frantic week at the beginning of my PhD studies when Pavlos Lagoudakis visited the group and owe him a great deal for teaching me many of the techniques that were essential to my studies.

I thank Alexey Kavokin, Ivan Shelykh, Guillame Malpuech and Tim Liew for their help and patience when explaining the theory behind my experiments.

I am grateful for the stimulating discussions with my fellow students Otto Pursiainen, Nic Perney, Becky Pennington, Matt Markham and Tim Kelf. Unfortunately we never did decide on whether the crocodile or the shark would win!

Finally I would like to thank my wife and family for their unwavering love and support.

Chapter 1

Introduction

In this 'age of information' great importance is placed on new technology that allows faster processing of information and increased bandwidth of data transmission. World-wide optical fiber networks have been installed which allow information to be transmitted at optical frequencies, however current information encoding and processing technologies rely in silicon electronics, whose processing speed is pinned in the GHz regime. A push towards faster optoelectronic devices and even all-optical computing systems is now underway. Recent advances in the study of microcavity polaritons suggest that they could provide part of the answer [1; 2; 3]

1.1 Historical Overview

In 1951 Huang [4] published a paper describing the interaction of an electromagnetic wave with the ionic-polarizability of a solid. He found that close to the resonant frequency of a solid the nature of a photon departs from that of an electromagnetic wave and takes on a more mechanical nature. This new entity was later named a 'polariton' by Hopfield [5]. It was not until 1971 that Frohlich [6] showed the first experimental evidence of exciton-polaritons, using two-photon absorption spectroscopy to measure the polariton dispersion. The normal mode coupling of bulk excitons with the electromagnetic field imposes one-to-one coupling between exciton and photon modes having the same momentum. Therefore photoluminescence should provide direct measurement

of the polariton states. However the static nature of polaritons means that photoluminescence requires propagation to the crystal surface, making it complicated to interpret [7].

A huge advance came in 1992 when Weisbuch [8] showed strong-coupling in a semiconductor microcavity, dropping from three to two dimensions. He took the high quality planar microcavities used to produce vertical-cavity surface emitting lasers. These structures consisted of a pair of distributed Bragg reflectors, sandwiching a collection of quantum wells. The quantum wells provide the active material required for lasing, and the DBRs form a cavity to confine the photons and concentrate their emission into a small angular range. Careful design of these structures allowed complete control of the excitons and photon wavefunction. By improving the quality of the DBRs, the coupling of the photons and excitons was increased beyond that of their decay rate from the system, resulting in strong-coupling. The benefit of these two dimensional systems is the direct coupling between the polaritons and the external photon modes.

In 1996 Imamoglu [9] wrote about using the bosonic nature of a polariton to show nonlinear effects such as lasing and condensation. However, treating polaritons as bosons was a hotly debated topic and it was not until 2000 when Savvidis [10] showed the first experimental proof, that the idea became universally accepted. Savvidis used a two-beam experiment to demonstrate polariton parametric amplification via the stimulated scattering of polaritons on the lower polariton branch. The discovery of stimulated scattering was closely followed by a report of parametric photoluminescence and the operation of a microcavity optical parametric oscillator [11].

Theoretical work by Imamoglu, Porras and Malpuech [9; 12; 13] suggested that the bosonic nature of polaritons and the momentum trap inherent in their dispersion made them an excellent candidate for a new type of laser, the polariton laser. Unlike a traditional laser, which relies on stimulated emission, a polariton laser uses the spontaneous emission of coherent light from an exciton-polariton condensate. Polariton lasers are of great interest because they have no threshold linked with population inversion. In 2003 Deng [1] *et al* showed the first experimental operation of a polariton laser, however it was not proved that the condensate formed to allow lasing was a Bose-Einstein condensate

(BEC). A BEC requires thermal equilibrium and the spontaneous build-up of an order parameter. Further work by Kasprzak [2] in 2006 and later by Balili [14] and Lai [15] in 2007, demonstrated BEC in a semiconductor microcavity.

1.2 Outline

Chapter 1 as presented above.

Chapter 2 contains a brief overview of the theory of excitons and semiconductor microcavity exciton-polaritons.

Chapter 3 contains a brief overview of the theory of the polariton laser and Bose Einstein condensation.

Chapter 4 gives the details of the microcavity structures studied in this thesis.

Chapter 5 gives a description of the experimental methods used to characterize the samples and study the parameters that define their dynamics.

Chapter 6 investigates the recovery dynamics of the microcavity optical parametric oscillator. A continuous wave laser resonantly injects polaritons into the system, forming an optical parametric oscillator which operates at equilibrium. A laser pulse is then used to inject surplus polaritons into the system, destabilizing it from equilibrium. The recovery dynamics are studied by temporally resolving the photoluminesnce from the signal state. It is shown that the population of the states of the optical parametric oscillator can be controlled on timescales approaching 1 ns, despite the polaritons having a lifetime three orders of magnitude below this. A simple theoretical model is used to explain the observed dynamics.

Chapter 7 uses a high-speed imaging system providing a spatial resolution of 5 microns and temporal resolution of 5 to 10 ps to investigate the spatial-temporal dynamics of microcavity polaritons. Pulsed experiments are used to measure the temporal dynamics of the real space distribution of polaritons, allowing direct measurement of their in-plane propagation speed. This is compared to their distribution under continuous wave excitation. Further studies of the microcavity optical-parametric-oscillator recovery dynamics,

coupling the high speed imaging system to the two beam experiment of Chapter 6, show that the spatial overlap of the beams plays a significant role in the observed dynamics.

Chapter 8 studies the room temperature dynamics of a bulk GaN microcavity. A variety of experimental techniques are used to show the operation of a room temperature polariton laser. Careful studies of the polarisation of the laser emission also suggest that a Bose-Einstein condensate is formed at room temperature.

Chapter 9 summarizes the main results of this thesis and suggests further experimental studies.

Chapter 2

The Theory of Semiconductor Microcavities

In this chapter the basic concepts of semiconductor exciton polaritons are reviewed. The first part of the chapter introduces the exciton, and is followed by a description of the effect of confinement on both excitons and photons. The second part introduces strong coupling and the concept of the polariton, with comparisons made between three dimensional and two dimensional systems. There are many excellent books and review papers that cover many of these subjects in great detail, for example [16].

2.1 Excitons in 3D

The attractive Coulomb interaction between an electron and a hole allows the formation of a bound state. This bound state is called an 'exciton' and has an associated binding energy E_b. As well as the optical transitions for photon energies larger than the energy band gap, $\hbar\omega \geq E_g$, there are some additional, discrete transition resonances with energies, $\hbar\omega = E_g - E_b$. The reverse process can also occur, with a photon (radiative recombination) or phonon (non-radiative recombination) being emitted when an exciton annihilates with the recombination of a bound electron-hole (e-h) pair. Excitons are typically classified by their radius; in molecular crystals excitons are tightly bound

(Frenkel)[17], whereas in the semiconductors used here their radius is typically much larger than the interatomic spacing and as such they can be described by a two particle effective-mass equation (Wannier-Mott)[18].

2.1.1 Wannier-Mott Excitons

Although the physical scales of the exciton are different to those of the hydrogen atom, the fact that they are both a bound state of positive and negative charge, means that the physics describing them is similar. Atomic physics was well established before the discovery of the exciton, and so many properties of the exciton are described using terms generally associated with atomic physics. For example, by replacing the proton mass with the reduced electron-hole mass, ($\frac{1}{\mu} = \frac{1}{m_e} + \frac{1}{m_h}$), and the electronic charge by $\frac{e}{\epsilon}$, it is possible to use the Bohr hydrogen model to describe an exciton [19]. Therefore, the energy of an exciton state is given by the modified exciton Rydberg energy:

$$E_{ex} = E_g - E_b + \frac{\hbar^2 K^2}{2M} \tag{2.1}$$

where, for the n_s state,

$$E_B^{3D} = \frac{\hbar^2}{2\mu a_{ex}^2 n^2} \tag{2.2}$$

and

$$\alpha_{ex} = \frac{\hbar^2 \epsilon}{e^2 \mu} \tag{2.3}$$

is the exciton Bohr radius, ϵ is the dielectric constant, n is the principal quantum number and $K = k_e + k_h$, $M = m_e + m_h$ are the translational wave vector and mass of the exciton respectively. The light effective masses of the carriers combined with dielectric screening of the Coulomb interaction, makes the exciton Rydberg energy considerably smaller, and the exciton Bohr radius considerably larger than the atomic one. In general, the exciton

radius is larger than the lattice constant and hence the 'orbits' of electron and hole around their common center of mass average over many unit cells, which justifies the effective-mass approximation. [20]

As a consequence of the small exciton Rydberg energy, in many material systems excitons are not stable at room temperature. For example in GaAs the exciton Bohr radius ~ 150Å and the exciton binding energy is 4.1 meV [21], which is much smaller than the thermal energy at room temperature ($k_BT \simeq 25$ meV). There are however some semiconductor materials (for example GaN and Cu_2O) with exciton binding energies great enough for them to survive at room temperature. Interactions between excitons lead to a decrease of optical transition energy with an increase of carrier density. This energy red-shift is called 'band gap renormalization'. Such interactions include the Coulomb screening effect and its associated screening length, which is a measure of the effectiveness of the Coulomb interaction between the electron and hole in the presence of other carriers. Phase space filling is a further effect, but of a quantum nature, arising from the fermionic nature of the electrons and holes, where Pauli's exclusion principle forbids the occupation of the same quantum state by particles with the same quantum numbers.

2.2 Exciton Optical Transition

An electrical dipole is formed by the electron and hole in an exciton and this interacts with electromagnetic fields. The interband optical transition probability is given by the product of an optical matrix element and a density of states and is given by Fermi's golden rule [16]:

$$W = \frac{2\pi}{\hbar} \sum_{f,i} |\langle f|\hat{H}_I|i\rangle|^2 \delta(E_f - E_i - \hbar\omega), \tag{2.4}$$

where i and f denotes the initial and final states with energies E_i and E_f respectively; $\hbar\omega$ is the photon energy, and $\hat{H}_I$ is the dipole interaction Hamiltonian $-e\mathbf{r}\cdot\mathbf{E}$. The

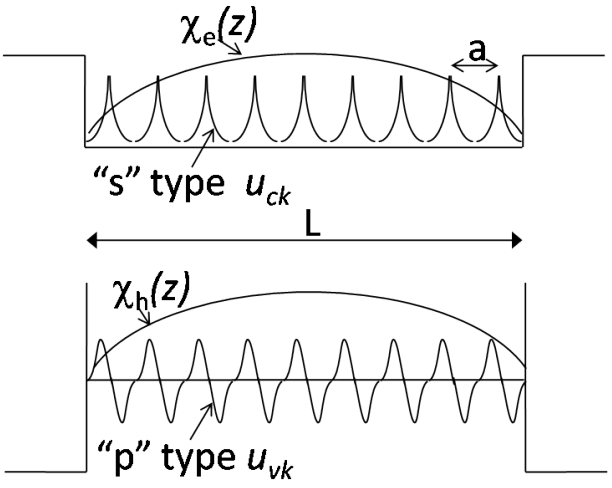

FIGURE 2.1: The electron and hole wavefunctions in a quantum well of width L are the product of the Bloch functions u_{ck_e} and v_{ck_h} with the envelope wavefunctions $\chi_e(z)$ and $\chi_h(z)$.

delta function implies that energy is conserved in the transition. The matrix element has the form:

$$M = |\langle f|\hat{H}_I|i\rangle| = \int_V \chi^*_{ck_e}(\mathbf{r})u^*_{ck_e}(\mathbf{r})e\mathbf{r}\cdot\mathbf{E}u_{vk_h}(\mathbf{r})\chi_{vk_h}(\mathbf{r}), \tag{2.5}$$

where E is the polarisation vector of light χ_{ck_e} and χ_{vk_h} are the slowly varying envelope functions of the electron and hole and u_{ck_e} and v_{vk_h} are the Bloch functions. Notice that u_{ck_e} has s-wave symmetry while u_{vk_h} has p-wave symmetry, as is shown in the schematic representation of figure 2.1.

2.2.1 Oscillator Strength of Excitons

The exciton oscillator strength, f, characterizes the exciton-photon coupling and is defined as:

$$f = \frac{2m^*\omega}{\hbar}|\langle f|\mathbf{E}\cdot\mathbf{r}|i\rangle|^2 \tag{2.6}$$

where m^* is the free electron mass and ω is the frequency. It can be shown that the reduction in Bohr radius due to 2D confinement results in an 8 fold increase in the oscillator strength per unit crystal volume [16]:

$$f_{2D} = 8f_{3D} = \frac{2m^*\omega}{\hbar}|\langle u_c|\mathbf{E}\cdot\mathbf{r}|u_v\rangle|^2\frac{8}{\pi a_B^3} \tag{2.7}$$

where $\langle u_c|\mathbf{E}\cdot\mathbf{r}|u_v\rangle$ is the valence band conduction band matrix element and a_B is the Bohr radius.

2.3 Excitons in 2D

2.3.1 Quantum confinement

Advances in semiconductor growth techniques allow materials to be fabricated to atomic monolayer precision, allowing the manufacture of quantum stuctures such 2D quantum wells (QWs), 1D quantum wires, and 0D quantum dots. A QW is a thin layer of narrow bandgap semiconductor sandwiched between two barrier layers of wider bandgap materials. The quantum well is designed to be thin enough that the motion of electrons and holes are confined perpendicular to the QW plane, leading to quantized energy levels. The 3D energy density of states (DOS) is a continuous function $\propto E^{\frac{1}{2}}$, which contrasts to the step function in 2D [16] as shown in figure 2.3. Their dispersion relation also contains a series of discrete bands (fig 2.2).

The quantum confinement also modifies the valence band structure significantly, as illustrated in figure 2.4. In 3D, a quadruplet degenerate state exists at $k = 0$, consisting of two degenerate light hole bands and two degenerate heavy hole bands. In 2D, where the translational symmetry is broken in the z-direction, the degeneracy between light and heavy holes at $k = 0$ is lifted, and the heavy-hole bands become closer to the conduction band with a lighter in-plane mass of $m_{hh\|} = \frac{m_e}{\gamma 1 - \gamma 2}$ near $k = 0$ [16].

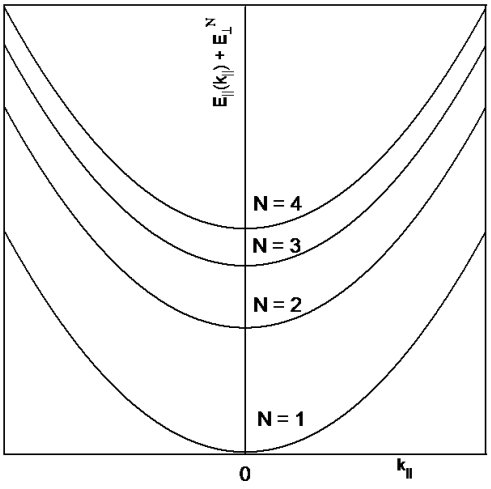

FIGURE 2.2: Confinement of excitons in a QW leads to discrete energy bands.

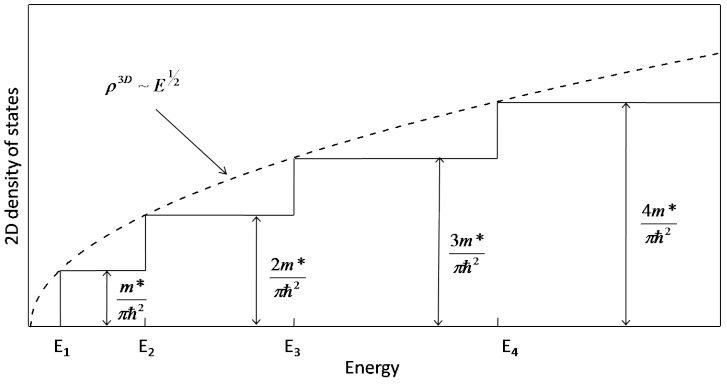

FIGURE 2.3: A comparison between the 2D and 3D density of states. Notice that the 2D density of states contains discontinuities at each energy level E_n

2.3.2 Quantum well exciton binding energy

In the limit of an exact 2D gas, the Bohr radius of an exciton becomes half of the corresponding 3D value given by equation 2.3, $a_B^{2D} = \frac{a_B^{3D}}{2}$, and the binding energy is increased by a factor of four compared to the 3D value in equation 2.2, $E_B^{2D} = 4E_B^{3D}$. More accurate values of a_B^{2D} and E_B^{2D} can be obtained by taking into account the finite QW thickness [22; 23].

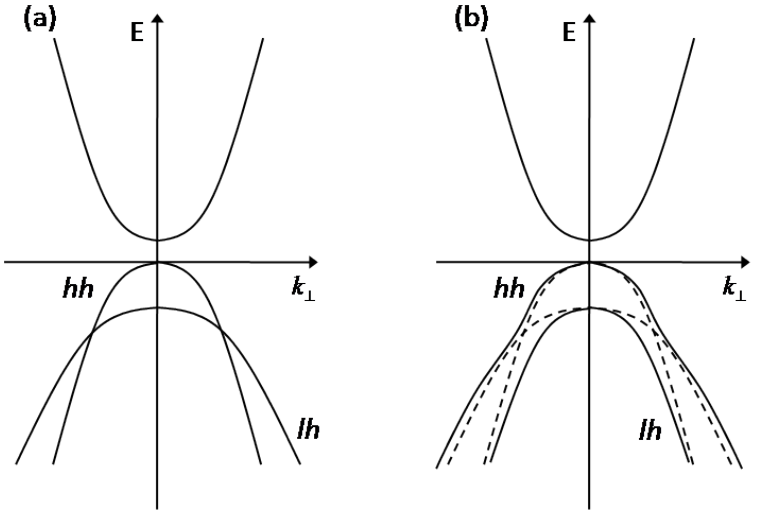

FIGURE 2.4: (a) Heavy (hh) and light (lh) hole bands in the absence of band mixing in quantum wells showing the *mass reversal* (b) The same bands in the presence of band mixing (solid curves) showing the removal of the degeneracies that are present without band mixing (dashed curves).

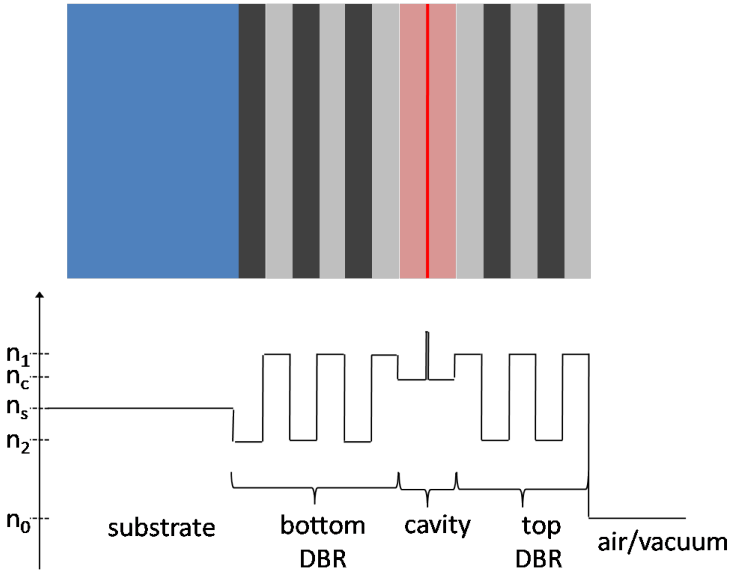

FIGURE 2.5: A schematic indicating the structure of a semiconductor microcavity. Distributed Bragg Reflectors (black and grey regions) are grown onto a substrate (blue layer) and define a cavity region (light red) that contains QWs (dark red). An indication of the relative refractive indices of the layers is shown below the schematic.

2.4 Cavities

Figure 2.5 shows a schematic of the structure of a typical semiconductor microcavity. The cavity is defined by two distributed Bragg reflectors (DBRs), separated by a cavity layer that is an integer multiple of $\frac{\lambda_c}{2}$ long, where λ_c is the wavelength of light in the cavity medium. A DBR is constructed of alternating layers of two materials having

different refractive indices. The layers are designed to have an optical thickness of $\frac{\lambda}{4}$ so that light reflected from each interface constructively interferes. This leads to the creation of a stop-band and hence for wavelengths of light within the stopband the DBR acts as a high-reflectance mirror (fig 2.6).

The maximum reflectivity, R_{max} of a DBR is at the centre of the stop band [24]. The reflectivity increases with the number of layers, N and with the refractive index contrast of the pair. If $n_c < n_1$ or n_2 and $n_s > n_1$ or n_2, as is often the case for a bottom DBR, the maximum reflection is achieved with a DBR of $2N$ layers and with $n_1 < n_2$. In the case of a top DBR, light transmits into air which has $n_t = 1$ or n_2 then maximum reflection is obtained with a DBR of $2N + 1$ layers and with $n_1 > n_2$ [25].

When two such high-reflectance DBRs are attached to a layer with an optical thickness integer times of $\frac{\lambda_c}{2}(\lambda_c \approx \lambda)$, a cavity resonance is formed at λ_c leading to a sharp increase of the transmission T at λ_c[25]:

$$T = \frac{(1 - R_1)(1 - R_2)}{[1 - \sqrt{R_1 R_2}]^2 + 4\sqrt{R_1 R_2}\sin^2(\frac{\phi}{2})} \tag{2.8}$$

where ϕ is the cavity round-trip phase shift of a photon at λ_c. If $R_1 \approx R_2 = R$, $\left(\frac{1-R}{2}\right)^2 \leq T \leq 1$ depending on ϕ. One characteristic parameter of the cavity quality is the quality factor Q defined as [24]:

$$Q = \frac{\lambda_c}{\Delta\lambda_c} \simeq \frac{\pi(R_1 R_2)^{\frac{1}{4}}}{1 - (R_1 R_2)^{\frac{1}{2}}}, \tag{2.9}$$

where $\Delta\lambda_c$ is the width of the resonance. If the cavity length is $\frac{\lambda}{2}$, Q is the average number of round trips a photon travels inside the cavity before it escapes. Figure 2.6 gives an example of the reflection spectrum of a cavity with $Q \simeq 1000$, calculated using the transfer matrix method. Figure 2.8 shows the field intensity distribution $|E(z)|^2$ of a resonant TE-mode. The field is concentrated around the centre of the cavity. Its intensity is amplified compared to the free space value, yet unlike in a metallic cavity, the field penetration depth into the DBRs is much larger. The effective cavity length is extended in a semiconductor microcavity as [25]:

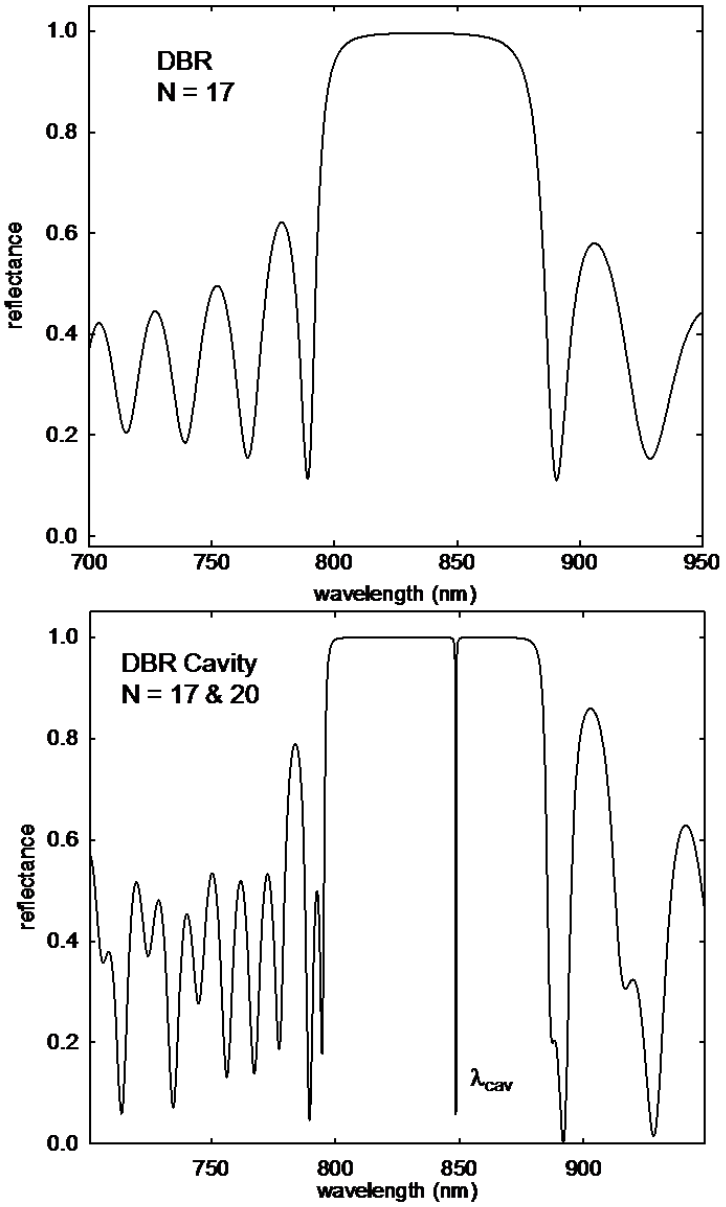

FIGURE 2.6: Top: Reflectance of a DBR calculated using the transfer matrix method, with $n_1 = 3$ and $n_2 = 3.9$, the highly reflective stop-band is easily identified. Bottom: Two DBRs have been combined to form a microcavity, with a cavity resonance at 849.5nm.

$$L_{eff} = L_c + L_{DBR} \tag{2.10}$$

$$L_{DBR} \approx \frac{\lambda_c}{2n_c} \frac{n_1 n_2}{|n_1 - n_2|}. \tag{2.11}$$

The planar DBR-cavity confines the photon field in the z-direction but not in plane. Incident light from an angle θ relative to the z-axis has a resonance at $\frac{\lambda_c}{\cos\theta}$. As a result,

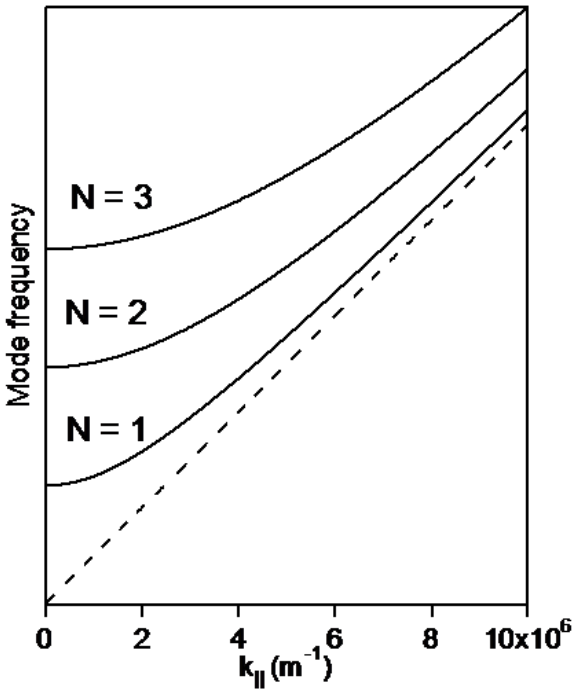

FIGURE 2.7: The dispersion curves of a cavity resonator. Modes n = 1 - 3 have been plotted. The 2D free photon dispersion is indicated by the dashed line.

the cavity has an energy dispersion vs the in-plane wavenumber $k_{\|}$ (fig 2.7):

$$E_{cav} = \frac{\hbar c}{N_c}\sqrt{k_{\perp}^2 + k_{\|}^2} \tag{2.12}$$

where $k_{\|} = n_c \frac{2\pi}{\lambda_c}$. Also there is a one-to-one correspondence between the incidence angle θ and each resonance mode with in-plane wavenumber $k_{\|}$:

$$k_{\|} = n_c \frac{2\pi}{\lambda_c} \tan\left[\sin^{-1}\left(\frac{\sin\theta}{n_c}\right)\right] \tag{2.13}$$

for $k_{\|} \ll k_{\perp} \frac{2\pi}{\lambda_c}\theta$

In the region where $k_{\|} \ll k_{\perp}$, we have:

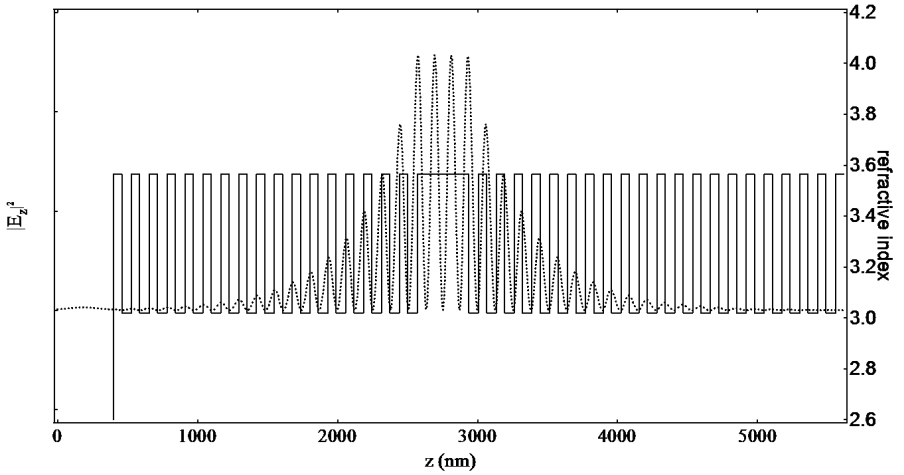

FIGURE 2.8: A simulation of the electric field distribution inside a $\frac{3}{2}\lambda$ microcavity. The field is concentrated within the cavity and QWs are placed at the antinodes for optimal light-matter coupling.

$$E_{cav} \approx \frac{\hbar c}{n_c k_\perp}\left(1 + \frac{k_\parallel^2}{2k_\perp^2}\right) \tag{2.14}$$

$$= E_{cav}(k_\parallel = 0) + \frac{\hbar^2 k_\parallel^2}{2}\left(\frac{2\pi\hbar}{\lambda_c c}\right) \tag{2.15}$$

$$= E_{cav0} + \frac{\hbar^2 k_\parallel^2}{2m_{cav}} \tag{2.16}$$

Thus the cavity photon has an effective mass of

$$m_{cav} = \frac{2\pi\hbar}{\lambda_c c} \tag{2.17}$$

2.5 Microcavity Polaritons

Exciton polaritons were first conceived by Huang [4] and later Hopfield [5]. Initial studies focussed on three dimensional systems. Due to translational symmetry, each exciton is strongly coupled to a single photon mode in an infinite crystal and the resulting coupled mode excitation, the polariton, is the true propagating mode inside the system [26]. Therefore photoluminescence should provide direct measurement of the polariton states. However the static nature of polaritons means that photoluminescence requires

propagation to the crystal surface, making it complicated to interpret [7]. The pioneering work of Weisbuch in 1992 [8] moved the study of polaritons into two dimensional systems. He placed QWs at the antinodes of the microcavity photon field to maximise the exciton photon coupling.

Using the rotating wave approximation, the linear Hamiltonian of the system is written in the second quantisation form as [26]:

$$\hat{H}_{pol} = \hat{H}_{cav} + \hat{H}_{exc} + \hat{H}_I \tag{2.18}$$

$$= \sum E_{cav}(k_\parallel, k_c)\hat{a}^\dagger_{k_\parallel}\hat{a}_{k_\parallel} + \sum E_{exc}(k_\parallel)\hat{e}^\dagger_{k_\parallel}\hat{e}_{k_\parallel} + \sum \hbar\Omega(\hat{a}^\dagger_{k_\parallel,k_c}\hat{e}_{k_\parallel} + \hat{a}_{k_\parallel,k_c}\hat{e}^\dagger_{k_\parallel}) \tag{2.19}$$

where $\hat{a}^\dagger_{k_\parallel}$ is the photon creation operator with an in-plane wavenumber $k_\parallel$ and longitudinal wavenumber k_c, determined by the cavity resonance, $\hat{e}^\dagger_{k_\parallel}$ is the exciton creation operator with in-plane waveneumber $k_\parallel$, and $\hbar\Omega$ is the exciton-photon dipole interaction given by the exciton optical matrix element M (2.5), where M is non-zero between modes with the same $k_\parallel$. Following [26] for example, the above Hamitonian can be diagonalised by the transformation:

$$\hat{p}_{k_\parallel} = X_{k_\parallel}\hat{e}_{k_\parallel} + C_{k_\parallel}\hat{a}_{k_\parallel} \tag{2.20}$$

$$\hat{q}_{k_\parallel} = -C_{k_\parallel}\hat{e}_{k_\parallel} + X_{k_\parallel}\hat{a}_{k_\parallel} \tag{2.21}$$

and $\hat{H}_{pol}$ becomes:

$$\hat{H}_{pol} = \sum E_{LP}(k_\parallel)\hat{p}^\dagger_{k_\parallel}\hat{p}_{k_\parallel} + \sum E_{UP}(k_\parallel)\hat{q}^\dagger_{k_\parallel}\hat{q}_{k_\parallel} \tag{2.22}$$

The new operators $(\hat{p}_{k_\parallel}, \hat{p}^\dagger_{k_\parallel})$ and $(\hat{q}_{k_\parallel}, \hat{q}^\dagger_{k_\parallel})$ are the eigen modes of the system. They are called the lower polariton (LP) and upper polaritons (UP), corresponding to the lower

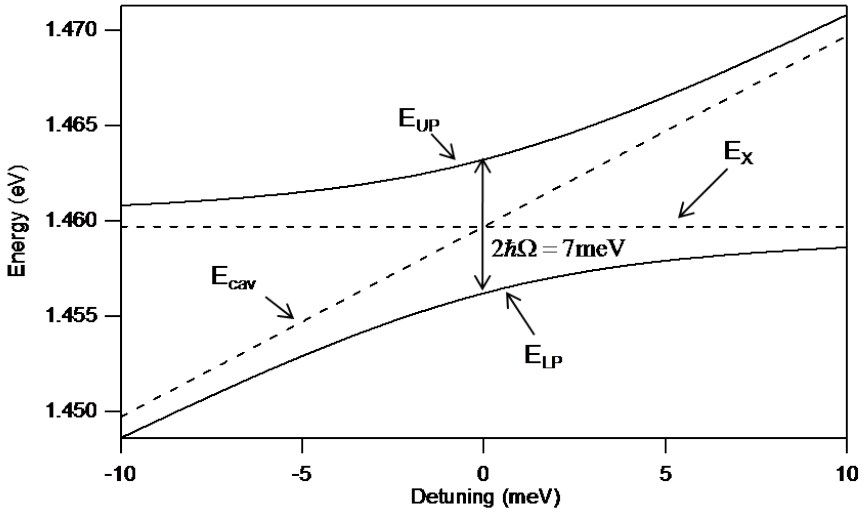

FIGURE 2.9: A calculation showing the dependence UP and LP energies on detuning, Δ

and upper branches of the eigen energies. A polariton is a superposition of an exciton and a photon with the same in-plane wavenumber $\mathbf{k}_{\|}$. The exciton and photon fractions of the lower polariton are given by the amplitude squared of $X_{k_{\|}}$ and $C_{k_{\|}}$ which are reffered to as the Hopfield coefficients [5] and must satisfy the relationship:

$$|X_{k_{\|}}|^2 + |C_{k_{\|}}|^2 = 1 \tag{2.23}$$

Defining $\Delta E(k_{\|}) = E_{cav}(k_{\|}) - E_{exc}(k_{\|}, k_c)$, $X_{k_{\|}}$ and $C_{k_{\|}}$ are given by [26]:

$$|X_{k_{\|}}|^2 = \frac{1}{2}\left(1 + \frac{\Delta E(k_{\|})}{\sqrt{\Delta E(k_{\|})^2 + 4\hbar^2\Omega^2}}\right) \tag{2.24}$$

$$|C_{k_{\|}}|^2 = \frac{1}{2}\left(1 - \frac{\Delta E(k_{\|})}{\sqrt{\Delta E(k_{\|})^2 + 4\hbar^2\Omega^2}}\right), \tag{2.25}$$

At $\Delta E = 0$,$|X|^2 = |C|^2 = \frac{1}{2}$, and the LP and UP are exactly half photon half exciton, as can be seen in figure 2.10.

The energies of the polaritons can be found by diagonalising the Hamiltonian (2.22) [26]:

$$E_{LP,UP}(k_{\|}) = \frac{1}{2}\left[E_{exc} + E_{cav} \pm \sqrt{4\hbar^2\Omega^2 + (E_{exc} - E_{cav})^2}\right] \tag{2.26}$$

When the uncoupled exciton and photon are at resonance, $E_{exc} = E_{cav}$, lower and upper polariton energies have the minimum separation $E_{UP} - E_{LP} = 2\hbar\Omega$, which is often called the 'vacuum Rabi splitting' in analogy to the atomic cavity Rabi splitting. Due to the coupling between the exciton and photon modes, the new polariton energies anti-cross when the cavity energy is tuned across the exciton energy. This is one of the signatures of 'strong coupling' (fig 2.9). When $|E_{cav} - E_{exc}| \gg \hbar\Omega$, the polariton energies reduce to the same as the photon and exciton energies due to the very large detuning between the two modes, and the polariton is no longer a useful new concept.

We define Δ as the detuning between the exciton and photon energy at $k_{\|} = 0$:

$$\Delta = E_{cav}(k_{\|} = 0) - E_{exc}(k_{\|} = 0) \tag{2.27}$$

and define

$$k_{\|c} = \sqrt{n_c k_c \frac{2\Omega}{c}} \tag{2.28}$$

for which $E_{cav}(k_{\|c}) - E_{cav}(0) \sim \hbar\Omega$. Given Δ, equation 2.26 gives the polariton energy-momentum dispersions. At $k_{\|} \ll k_{\|c}$, the dispersions are approximately parabolic:

$$E_{LP,UP}(k_{\|}) \simeq E_{LP,UP}(0) + \frac{\hbar^2 k_{\|}^2}{2m_{LP,UP}} \tag{2.29}$$

The polariton effective mass is the weighted harmonic mean of the mass of its exciton and photon components:

$$\frac{1}{m_{LP}} = \frac{|X^2|}{m_{exc}} + \frac{|C^2|}{m_{cav}} \tag{2.30}$$

$$\frac{1}{m_{UP}} = \frac{|C^2|}{m_{exc}} + \frac{|X^2|}{m_{cav}} \tag{2.31}$$

where X and C are the exciton and photon fractions given by eqns (2.24, 2.25), m_{exc} is the effective exciton mass of its centre mass motion, and m_{cav} is the effective cavity photon mass given by (2.17). Since m_{cav} is much smaller than m_{exc}:

$$m_{LP}(k_{\|} \sim 0) \simeq \frac{m_{cav}}{|C|^2} \sim 10^{-4} m_{exc} \tag{2.32}$$

$$m_{UP}(k_{\|} \sim 0) \simeq \frac{m_{cav}}{|X|^2} \tag{2.33}$$

The very small effective mass of LPs at $k_{\|} \sim 0$ determines the very high critical temperature of phase transitions for the system. At large $k_{\|} \gg k_{\|c}$, where $E_{cav}(k_{\|}) - E_{exc}(k_{\|}) \gg \hbar\Omega$, dispersions of the LP and UP converge to the exciton and photon dispersion respectively, and LP has an effective mass $m_{LP}(k_{\|} \gg k_{\|c}) \sim m_{exc}$. Hence the LP's effective mass changes by four orders of magnitude from $k_{\|} \sim 0$ to large $k_{\|}$. Figure 2.10 shows the effect of changing Δ on the polariton dispersion.

When taking into account the finite lifetime of the cavity photon and QW exciton, the eigen-energy equation (2.26) must be modified to:

$$E_{LP,UP}(k_{\|}) = \frac{1}{2}\left[E_{exc} + E_{cav} + i(\gamma_{cav} + \gamma_{exc}) \pm \sqrt{4\hbar^2\Omega^2 + [E_{exc} - E_{cav} + i(\gamma_{cav} - \gamma_{exc})]^2}\right] \tag{2.34}$$

where γ_{cav} is the out-coupling rate of a cavity photon due to imperfect mirrors, and γ_{exc} is the non-radiative decay rate of an exciton. Thus the coupling strength must be larger than half of the difference in decay rates to exhibit anti-crossing, i.e. to have polaritons as the new eigen modes. In other words, an excitation must be able to coherently transfer

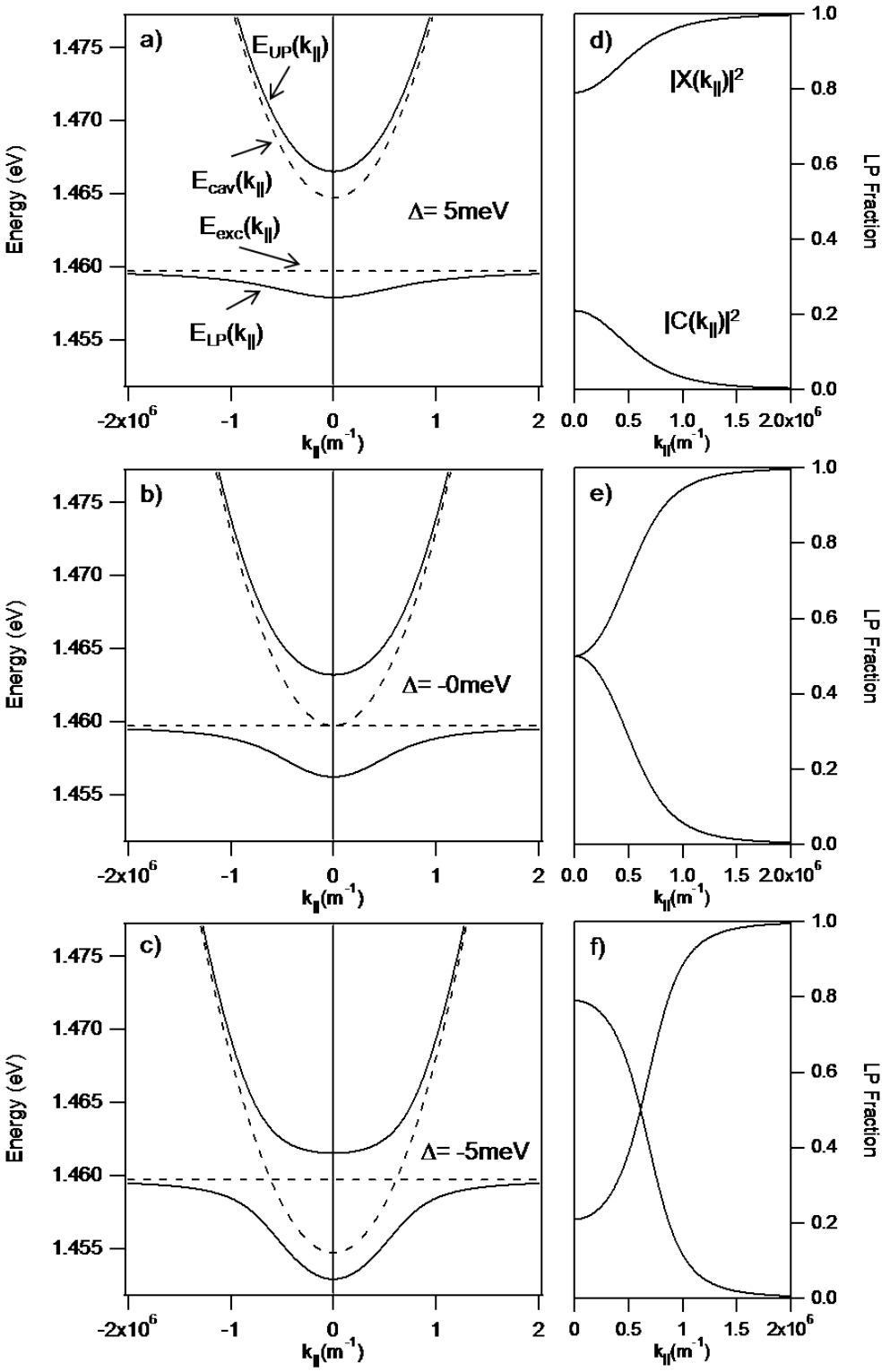

FIGURE 2.10: a) - c) LP and UP dispersions plotted for negative ($\Delta = -5meV$), zero ($\Delta = 0$), and positive ($\Delta = +5meV$) detunings. d) - f) show the corresponding Hopfield coefficients for the LP.

between a photon and an exciton at least once. When $\hbar\Omega \gg \frac{(\gamma_{cav}-\gamma_{exc})}{2}$, we describe the system as being in the strong coupling regime. In the opposite limit, when excitons and photons instead are the eigen modes, the system is said to be in the weak coupling regime, and the radiative decay rate of an exciton is given by the optical transition matrix element. We are mostly interested in microcavities with $\gamma_{exc} \ll \gamma_{cav} \ll \hbar\Omega$, hence equation (2.26) gives an accurate approximation of the polariton energies.

From their origin as a linear superposition of an exciton and a photon, the lifetime of the polaritons is directly determined by γ_{exc} and γ_{cav} as:

$$\gamma_{LP} = |X|^2\gamma_{exc} + |C|^2\gamma_{cav} \tag{2.35}$$

$$\gamma_{UP} = |C|^2\gamma_{exc} + |X|^2\gamma_{cav} \tag{2.36}$$

For the GaAs system under study in chapters 6 and 7 γ_{cav} =1∼10 ps and γ_{exc} ∼1 ns, hence the polariton lifetime is mainly determined by the cavity photon lifetime: $\gamma_{LP} \simeq |C|^2\gamma_{cav}$. Polariton decays in the form of emitting a photon with the same $k_{\|}$ and total energy $\hbar\omega = E_{LP,UP}$. The external emitted photon field carries direct information of the internal polaritons, such as the energy dispersion, population per mode, and statistics of the polaritons.

2.5.1 Comparison to bulk polaritons

In bulk semiconductors, the coupling strength between exciton and photon is relatively large due to the full overlap of their three dimensional wavefunctions. This results in polaritons being eigen modes of the system. However, in bulk systems, a polariton has the same wavenumber as that of its exciton and photon constituents: $k \sim \frac{n_{bulk}E_{exc}}{\hbar c} \sim k_c$, rather than $k_{\|} \sim \sqrt{k^2 - k_c^2} \ll k_c$ in the case of a QW microcavity polariton. It is vulnerable to various dephasing channels and the thermal equilibrium state of the system consists of mostly $k \sim 0$ photon-like modes, rather than $k_{\|} \sim 0$ LPs in the case of a QW-microcavity.

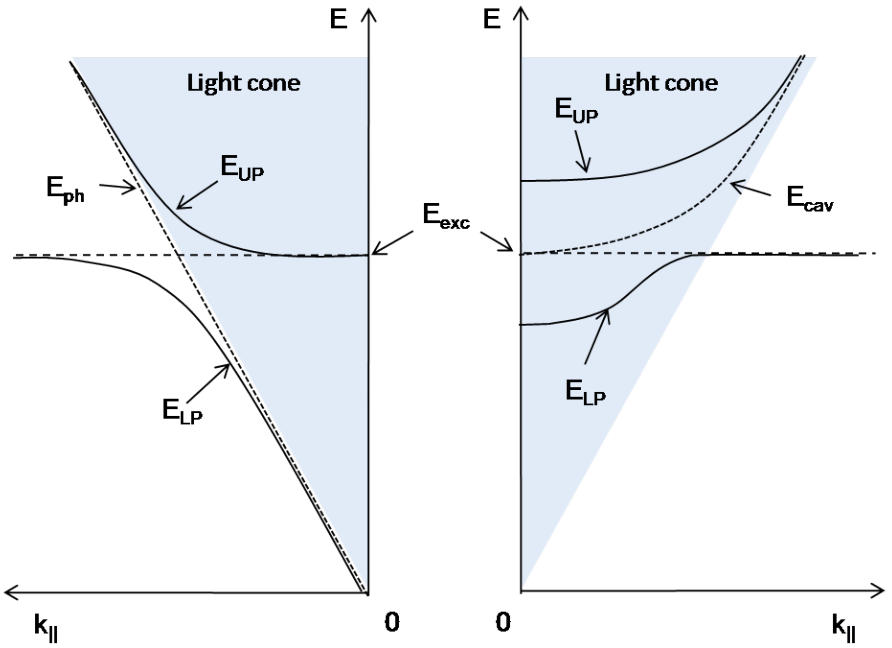

FIGURE 2.11: A comparison between the dispersions of microcavity and bulk polaritons. Notice that in the bulk regime the LP is outside of the light cone.

Inside the bulk, the LP is outside of the optical cone 2.11 and does not directly couple to light. Furthermore, a bulk polariton does not couple out of the system until it hits the surface of the crystal and is subject to scattering by crystal defects and impurities as well as other excitons and polaritons. All of these factors make studying polaritons in bulk material extremely difficult.

Chapter 3

The Theory of Polariton Lasing and Bose-Einstein Condensation

Bose-Einstein condensation (BEC) is the interesting phenomenon where bosons accumulate in the same degenerate quantum state. The first theoretical application of BEC was by London in 1938 [27], where he used it to explain a phase transition seen in liquid helium, right after the discovery of superfluidity in the same system [28; 29]. In 1962 Moskalenko [30] suggested that BEC of excitons was possible in the solid state. Huge effort was put into demonstrating this experimentally and in 1995 Wolfe appeared to demonstrate BEC of the ortho-excitons in bulk Cu_2O. However it was later found that the system had not been able to reach its critical density [31; 32; 33]. In the same year, the first unambiguous realization of BEC was achieved in dilute atomic gases [34; 35; 36]. A year later, in 1996, Imamoglu and Ram [9] proposed that exciton-polaritons, could exhibit BEC in a solid state system. With huge potential for new physics and interesting opto-electronic devices, such as the polariton laser (pLaser), great effort was spent working to realise a polariton BEC and in 2006 Kasprzak et al [2] successfully observed BEC in a CdTe semiconductor microcavity at 5 K. Since then there have been further reports of polariton BEC at low temperature [14; 15].

The small mass of the polariton means that critical temperatures exceeding 300 K should be achievable and our work has focussed on observing BEC at room temperature, along

with the operation of the first room-temperature pLaser. In order to put our work in context, this chapter reviews the basic concepts of BEC. Many comprehensive reviews of BEC are available in the literature [37; 38].

3.1 BEC of an Ideal Bose Gas

The following derivation follows, for example [37; 38; 39]. BEC of an ideal Bose gas results directly from quantum statistics. In a grand canonical ensemble, at thermal equilibrium, the probability of a configuration with M_r particles and energy E_s is given by:

$$P_{r,s} = \frac{e^{\beta(\mu M_r - E_s)}}{Z(\beta,\mu)}, \tag{3.1}$$

where $\beta = \frac{1}{k_B T}$,T is the temperature of the reservoir and μ is the chemical potential, where $-\mu$ is the energy needed to add a particle to the system. $Z(\beta,\mu)$ is the grand partition function:

$$Z(\beta,\mu) = \sum_{N_i}^{\infty} \sum_{s} e^{\beta(\mu M_r - E_s)} \tag{3.2}$$

Applied to an ideal gas of indistinguishable particles distributed in '*microstates i*' of energy ϵ_i and occupation number N_i in each state:

$$Z(\beta,\mu) = \sum_{M_r} e^{\beta(\mu \sum_i N_i - \sum_i \epsilon_i N_i)} = \prod_i \sum_{N_i} e^{\beta(\mu-\epsilon_i)N_i}. \tag{3.3}$$

In a Bose gas, $N_i = 0, 1, 2, ...,$

$$Z(\beta\mu) = \prod_i (1 - e^{\beta(\mu-\epsilon_i)}). \tag{3.4}$$

Using (3.4) we obtain the Bose-Einstein distribution function $f_{BE}(\epsilon_i)$, the total particle number N, and the total internal energy of the gas $E(T,\mu)$:

$$f_{BE}(\epsilon_i) = \bar{N}_i = -\frac{\partial}{\partial\beta\epsilon_i}\ln Z = \frac{1}{e^{\beta(\epsilon_i-\mu)}-1} \tag{3.5}$$

$$N = -\frac{\partial}{\partial\mu}(k_BT\ln Z) = \sum_i \frac{1}{e^{\beta(\epsilon_i-\mu)}-1} \tag{3.6}$$

$$= \sum_i f_{BE}(\epsilon_i), \tag{3.7}$$

$$E(T,\mu) = \sum_i \epsilon_i f_{BE}(\epsilon_i) = \frac{\epsilon_i}{e^{\beta(\epsilon_i-\mu)}-1} \tag{3.8}$$

The requirement of $N_i \geq 0$ induces a unique constraint for a Bose gas: $\mu \leq \epsilon_0$ (ϵ_0 is the energy of the single particle ground state). Hence, at given T, $f_{BE}(\epsilon_i > \epsilon_0)$ reaches a finite maxima, while $f_{BE}(\epsilon_0)$ diverges. So (3.7) can be rewritten in terms of the particle number in the non-degenerate ground state, N_0, and in all other states, N':

$$N = f_{BE}(\epsilon_0,T,\mu) + \sum_{i\neq 0} f_{BE}(\epsilon_i,T,\mu) = N_0(T,\mu) + N'(T,\mu), \tag{3.9}$$

For a given T, the total number of particles in all *excited* states can not exceed $N_c(T) = N'(T,0)$. It can be shown that for systems with more than two dimensions $N_c(T)$ is finite, yet for dimensions of 2 or less an infinite number of non-interacting bosons can always be accommodated in the system. In higher dimensions, if $N > N_c(T)$, the difference all goes to the ground state $N_0(T) = N - N_c(T)$.

In the thermodynamic limit, ϵ_i becomes continuous, the number density vanishes for any excited state:

$$n_i = \frac{N_i}{V} = f_{BE}(\epsilon)\frac{\rho(\epsilon)d\epsilon}{V} \to 0, V \to 0 \tag{3.10}$$

The ground state $n_0 = \frac{N-N_c(T)}{V}$ becomes finite once $N > N_c(T)$. This means that a macroscopic number of particles *condense* into the single microscopic ground state, this is Bose-Einstein condensation.

For a free Bose gas

$$n_c(T_c) = \frac{N'(T_c, 0)}{V} = \left(\frac{mk_BT_c}{2\pi\hbar^2}\right)^{3/2} \left(\frac{2}{\sqrt{\pi}} \int_0^\infty dx x^{1/2} \frac{1}{e^x - 1}\right) \tag{3.11}$$

where m is the mass, $\epsilon = p^2/2m$, and $x = \epsilon/K_BT_c$.

3.1.1 The Bogoliubov Model of BEC

To reveal the physical significance of a macroscopic n_0, we introduce the Bogoliubov theory which lays down the framework for the modern BEC [40; 41; 42; 43; 39]. The first step is to consider the Hamiltonian of an *interacting* Bose gas:

$$H = \sum_{\mathbf{b}} E(\mathbf{k}) a^\dagger_{\mathbf{k}} a_{\mathbf{k}} + \frac{1}{2} \sum_{\mathbf{b},\mathbf{k}',\mathbf{q}} V_{\mathbf{q}} a^\dagger_{\mathbf{k}+\mathbf{q}} a^\dagger_{\mathbf{k}'-\mathbf{q}} a_{\mathbf{k}} a_{\mathbf{k}'} \tag{3.12}$$

where $\hat{a}_{\mathbf{k}}$ and $\hat{a}^\dagger_{\mathbf{k}}$ are annihilation and creation operators and $V_{\mathbf{q}}$ the Fourier transform of the interacting potential for the boson-boson scattering.

The first approximation in the Bogoliubov model is to neglect the condensate fluctuations and replace the operators a_0, $a_0^\dagger$ by complex numbers A_0, A_0^*. As a result the condensate can be treated as a classical particle reservoir. The second approximation of the model is to keep only the largest terms of the interacting Hamiltonian, those that involve the condensate. Therefore equation (3.12) becomes:

$$H = N_0 V_0^2 + \sum_{\mathbf{k},k\neq 0} \left(E(\mathbf{k}) + N_0(v_{\mathbf{k}} + V_0)\right) a^\dagger_{\mathbf{k}} a_{\mathbf{k}} + N_0 \sum_{\mathbf{k}} V_{\mathbf{k}} \left(a^\dagger_{\mathbf{k}} a^\dagger_{-\mathbf{k}} a_{\mathbf{k}} a_{-\mathbf{k}}\right) \tag{3.13}$$

These approximations conserve off-diagonal coupling terms that induce the appearance of new eigenmodes. The so-called Bogoliubov transformation can then be used to diagonalise the Hamiltonian to give [44]:

$$H = N_0 V_0^2 + \sum_{\mathbf{k},k\neq 0} E_{Bog}(\mathbf{k}) \alpha^\dagger_{\mathbf{k}} \alpha_{\mathbf{k}}, \tag{3.14}$$

where $\alpha_{\mathbf{k}}$, $\alpha_{\mathbf{k}}^{\dagger}$ are the new bosonic operators.

As a result the *Bogoliubov dispersion*, E_{Bog} is defined as:

$$E_{Bog}(\mathbf{k}) = \sqrt{E(\mathbf{k})[E(\mathbf{k}) + 2N_0V_{\mathbf{k}}]} \tag{3.15}$$

where

$$E(\mathbf{k}) = \frac{\hbar^2k^2}{2m} \tag{3.16}$$

is the unperturbed quadratic dispersion, which is recovered if $N_0 = 0$.

Near $k = 0$ the dispersion becomes linear and can be approximated by

$$E_{Bog}(\mathbf{k}) \approx \hbar k\sqrt{\frac{N_0V_0}{m}} \tag{3.17}$$

this describes phonon-like quasi particles with sound velocity

$$v_s = \sqrt{\frac{N_0V_0}{m}}. \tag{3.18}$$

These phonon-like modes are called the Bogoliubov quasi-particles, or, the Goldstone modes.

3.2 Polaritons for BEC Study

As composite bosons, with fermionic as well as photonic constituents, polaritons are an ideal system for exploring both cavity QED and many particle physics. A variety of quantum phases are predicted for polaritons, including BEC and superfluidity [45; 46; 47; 48; 49]. Compared to other BEC systems, such as atomic gases and excitons, polaritons have vastly different length, energy and time scales [39] as detailed in table 3.1. As such polaritons possess many unique advantages for BEC research.

	polaritons	excitons	atomic gas
effective mass	10^{-5}	10^{-1}	10^{-1}
Bohr radius	10^{2}Å	10^{2}Å	10^{-1}Å
particle spacing	1 μm	10^{2}Å	10^{3}Å
critical temperature	>300 K	1-1x10^{-3} K	1x10^{-9}-1x10^{-6}
thermalisation time/lifetime	0.1 - 10	10^{-2}	10^{-3}

TABLE 3.1: Typical scales associated with the different BEC systems.

First of all, the critical temperature of polariton condensation ranges from a few kelvin to above room temperature, which is four orders of magnitude higher than that of excitons and eight orders of magnitude higher than that of atoms [50; 51]. It originates from the very light effective mass of polaritons due to the mixing with cavity photons (eqn 2.30).

Second, microcavity polaritons can be excited, resonantly or non-resonantly, by optical pumping. There exists a one-to-one correspondence between an internal polariton in mode $k_{\|}$ and an external photon with the same energy and in-plane wavenumber, propagating at an angle θ from the growth direction. The polariton is coupled to this external photon via its photonic component with a fixed coupling rate (eqn 2.35) due to imperfect mirrors. Hence information of the internal polaritons can be directly measured from the external photon field by standard optical techniques, including the polariton's energy-momentum dispersions and distribution functions. The downside to microcavity exciton-polaritons is their rapid decay time. This makes thermalisation an issue. However under suitable conditions the decay time can be an order of magnitude longer than the thermalisation time.

A critical density N_c must be reached for BEC to occur. This can be a problem in exciton-based systems, because as densities increase, excitons interact via their fermionic constituents, the electron and hole, leading to detrimental interactions, for example Coulomb screening and phase space filling. In a microcavity system, multiple QWs and even bulk active material can be used to distribute the exciton density for a given total polariton density: $n_{exc}^{QW} = \frac{n_{LP}}{N_{QW}}$, where N_{QW} is the number of QWs. In our experiments, we have GaAs based samples designed with QWs and room-temperature GaN samples utilising bulk active material.

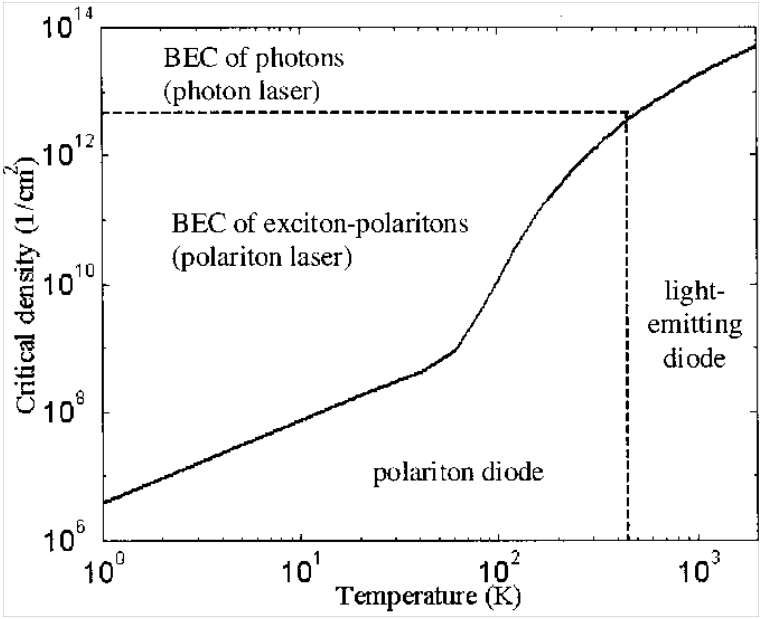

FIGURE 3.1: The phase diagram for polaritons in GaN, as calculated in [50]. The solid line shows the calculated KT phase transition. The dashed lines indicate the boundary between strong and weak coupling. Notice that BEC is possible at 300K

One of the main obstacles facing the BEC thermodynamic phase transition is the efficient cooling of hot particles. It is particularly so for relatively short-lived quasi-particles, excitons and polaritons, in solids which can decay before they thermalise. However polaritons can undergo bosonic final state stimulation and this greatly accelerates energy relaxation of polaritons.

In summary, BEC is the phenomenon where bosons accumulate in the same degenerate quantum state. BEC has been demonstrated in dilute atomic gases [34; 35; 36] and microcavity polaritons [2] at low temperatures. There are many challenges to overcome when designing a semiconductor microcavity which exhibits BEC, however it should be possible to achieve this at room temperature.

3.2.1 Polariton Phase Diagram

It is possible to use equations (3.25 -3.27) to obtain $T_{KT}(n)$ and thereby plot the polariton phase diagram (figure 3.1). The solid line shows the calculated critical concentration for a KT phase transition in GaN [50]. The broken lines show the approximate limit of the strong-coupling regime in a microcavity that come from either exciton screening by

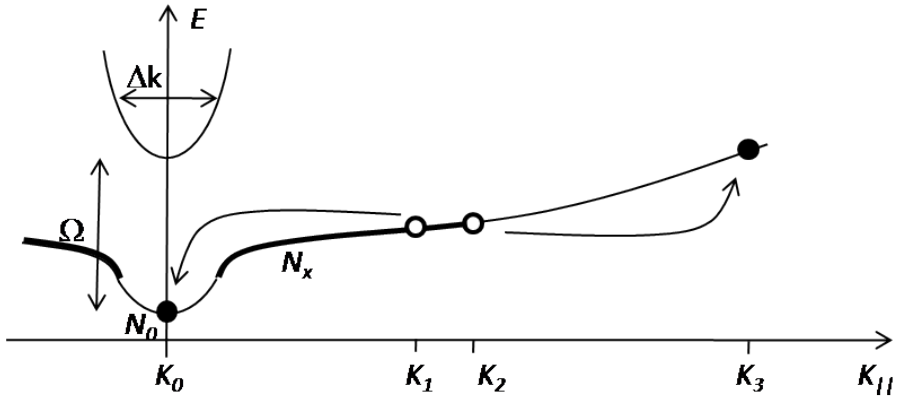

FIGURE 3.2: Dispersion relation for the pLaser. The polariton trap in $k_{||}$ is fed by pair scattering of excitons at $k_{1,2}$. Adapted from [11]

a photoinduced electron-hole plasma (horizontal) or from temperature-induced broadening of the exciton resonance (vertical). Below the critical density, if still in the strong coupling regime, a microcavity operates as a polariton diode emitting incoherent light, while in the weak coupling regime the device behaves like a conventional light-emitting diode. Above the critical density, in the weak coupling regime, the microcavity acts as a conventional laser.

3.3 The Polariton Laser

A polariton laser (pLaser) is an optoelectronic device based on the spontaneous emission of coherent light by a polariton Bose condensate in a microcavity. Kavokin et al [39] discuss a simple model for the polariton laser, and the core concepts are described in this section. This simple model makes a number of assumptions for the sake of simplicity, which can only be checked in the full quantum approach that is detailed in the following reference [39]. However they provide a first intuition as to how the pLaser compares to conventional VCSELs, and highlight the nature of the inversionless operation.

The model couples N_0 polaritons with an exciton reservoir of density N_x, assumed uniform over the polariton active mode volume, V. A polariton trap is created in momentum space by the strong coupling between photon and exciton. At $k = 0$ the states are split by the Rabi frequency Ω, producing a classical trap for polaritons in momentum space of depth $\Omega/2$ and FWHM $\hbar c\Delta k < \sqrt{6\epsilon\Omega E_{ex}}$. The $k = 0$ state is populated by excitons

in high-k states (k_1, k_2) scattering from each other (see figure 3.2). The quadratic shape of the exciton dispersion means that for energy and momentum to be conserved during these pair-scattering events, the excitons must be of sufficiently high k.

The total scattering rate depends on the occupation of the states involved. The pair scattering rate

$$\Gamma_{PS} = V\left[(1+N_0)f_1 f_2(1-f_3) - N_0 f_3(1-f_1)(1-f_2)\right] \tag{3.19}$$

where the first term is the final-state enhanced scattering into the N_0 polariton condensate and the second term is the re-ionization out of this trap. The Coulomb coupling constant $V \propto e^2/(4\pi\epsilon_0\epsilon_B a_B)$, where a_B is the exciton Bohr radius. The Fermi functions $f_i = 1/(1+e^{(E_i-E_f)/k_BT})$ provide an approximate distribution for the reservoir of excitons at temperature k_BT, and Fermi level E_f. Extracting the N_0 dependent and N_0-independent parts, this can be written in the form

$$N_0 R(N_x) + S(N_x) = \int d\mathbf{k}_1 \int d\mathbf{k}_2 \Gamma_{PS}(k_1, k_2) \tag{3.20}$$

where R is the stimulated scattering rate and S is the spontaneous scattering rate. For low temperatures compared to the trap potential depth ($k_BT < \Omega/2$), pair scattering only occurs if $E_f > \Omega/2$, implying that a sufficient number of excitons are needed to populate states at high enough k for which energy-momentum conservation becomes possible. For small exciton densities, no pair scattering is possible until the temperature is raised enough to populate these higher-k states. In the low-temperature regime, $f_3 = 0$ and so $R = S$ implying that only pair scattering *into* the polariton trap can occur, this being stimulated by occupation of the $k = 0$ state. As the temperature increases, the greater range of populated k_1 and k_2 increases the pair scattering, although ionization of polaritons out of the trap is also now possible from very high-k excitons, thus reducing R compared to S.

At low densities the pair scattering behaves quadratically as expected from a two-body incoherent process, so that

$$S = cN_x^2, \tag{3.21}$$

$$R = c\left(N_x^2 - d\frac{\Gamma_0}{\Gamma_{nr}}N_x\right), \tag{3.22}$$

where d allows for polariton ionization, Γ_{nr} and Γ_0 are the non-radiative and radiative emission rates respectively. Below threshold,

$$P_{th} = \hbar\omega V\Gamma_{nr}\sqrt{\frac{\Gamma_0}{c}} \tag{3.23}$$

the output power $P_{out} = \hbar\omega V\Gamma_{nr}\sqrt{\Gamma_0/c}$ corresponds to spontaneous pair scattering while above threshold, $P_{out} = P - P_{th}$. The associated $L - I$ curve differs from that of a conventional laser, allowing the possibility of new types of practical applications.

3.3.1 Comparision between Conventional and Polariton Lasing

In a pLaser, absorption at the emission wavelength is extremely weak, even at low exciton densities. Ionization of polaritons from their trap is prevented by the fast relaxation of high-energy excitons forming a "'thermal lock" (Fig. 3.2). Pair scattering separates the processes of absorption and emission through control of the exciton k-distribution, in contrast to conventional lasers for which absorption and emission are intimately linked. Unlike a conventional laser, the pLaser does not require population inversion, and hence does not require large carrier densities (threshold is several times less than the transparency density). Laser action can occur as soon as more than one polariton builds up in the trap, and the pair-scattering rate becomes stimulated by this final state occupation.

The pLaser works well until the build-up of carriers produces excessive broadening of the exciton transition resulting in absorption at the polariton energy and collapse of strong coupling regime.

3.4 Superfluidity

A further phenomenon often associated with BEC is superfluidity. A superfluid is a frictionless state that exhibits no spontaneous energy dissipation. Although BEC often implies superfluidity and vice versa, these are two distinct phenomena. For example, the Kosterlitz-Thouless phase in 2D is an example of a superfluid without BEC and BEC in disordered materials exhibits no superfluidity. Unfortunately, microcavity systems exhibit some photonic and excitonic disorder, reducing the likelihood of obtaining a superfluid phase of exciton polaritons. The Landau criterion for superfluidity is [52]:

$$v_s < v_c = \min_{\mathbf{p}} \frac{\omega(\mathbf{p})}{p} \tag{3.24}$$

Therefore a BEC with the dispersion given in 3.15 satisfies the above criterion when $v < v_c$.

3.4.1 Kosterlitz-Thouless Transition

In dimension $d \leq 2$, in the thermodynamic limit, the critical density defined in equation (3.9) diverges when $\mu \to 0$. It can be shown that in $d = 2$ with constant energy density of state, long wavelength thermal fluctuation of the phase destroys a long range order [53; 54], and BEC is absent at any temperature $T > 0$. BEC does exist at $T = 0$ where there are only quantum phase fluctuations.

However, phase fluctuations do not necessarily destroy superfluidity. In 2D, it is the thermal excitation of vortices which destroys superfluidity. This leads to a new type of phase transition in 2D, the Kousterlitz-Thouless (K-T) transition [52], with a critical temperature:

$$k_B T_{KT} = n_s \frac{\pi \hbar^2}{2m^2} \tag{3.25}$$

where n_s is the superfluid density. Above T_{KT}, vortices are thermally excited and produce friction, hence as a result, n_s and the number of vortices are exponentially

small. Below T_{KT}, single vortices are energetically costly, hence they bind to form pairs and cluster, with a total binding number equal to zero, allowing percolation of condensate droplets in which a phase coherent path exists between two distant points. Hence n_s jumps to a non-zero value. The superfluid is described by the same Bogoliubov theory for weakly interacting bosons, and follow the Bogoliubov quasi-particle dispersion $E_{Bog}(\mathbf{k})$ in (3.17). The superfluid density n_s is related to the normal fluid density n_n and total density n by the Landau formula derived in the framework of the *two-fluid model* (see for example [55]):

$$n = n_n + n_s, \tag{3.26}$$

$$n_n = \frac{1}{(2\pi)^2} \int E(\mathbf{k}, T, \mu) \left(-\frac{\partial f_{BE}(E_{Bog}(\mathbf{k}, T, \mu = 0))}{\partial E_{Bog}(\mathbf{k})} \right) d\mathbf{k}. \tag{3.27}$$

A BEC transition at finite temperature is recovered in 2D if the Bose gas is confined by a spatially varying potential $U \sim r^\eta$. In this case, the density of states becomes $\rho(E) \sim \epsilon^{2\eta}$, and the integral in (3.9) converges for $\eta > 0$, leading to a finite critical temperature for BEC transition:

$$k_B T_c^{2D} \sim (n/m)^{\eta/(2+\eta)} \tag{3.28}$$

In practice, any experimental system is of finite size and has finite numbers of particles. With discrete energy levels $\epsilon_i (i = 1, 2, ...)$, finite total particle number N, and finite size $S = L^2$, the critical condition defined in (3.10) can be modified as:

$$\mu = \epsilon_1; \tag{3.29}$$

$$n_c = \frac{1}{S} \sum\nolimits_{i \geq 2} \frac{1}{e^{\epsilon_i / k_B T} - 1}. \tag{3.30}$$

This allows the critical condition to be fulfilled at $T_c > 0$ even in a 2D box system of size L. The critical density is:

$$n_c = \frac{2}{\lambda_t^2} \ln\left(\frac{L}{\lambda_t}\right) \tag{3.31}$$

where λ_t is the thermal de Broglie wavelength. If the particle number N is sufficiently large, the transition shows similar features as a BEC transition defined at the thermodynamic limit [56].

3.5 Summary

In summary, this chapter has reviewed the basic concepts of BEC and superfluidity and the uniqueness of microcavity polaritons in BEC research has been highlighted. It was shown that interactions are necessary to form a genuine BEC, characterised by a sharply peaked distribution in the momentum-space, and phonon-like low-energy excitations. In 2D, BEC is absent in the thermodynamic limit but survives in a finite system. The basic concept of the pLaser was then described and comparisons with a conventional laser discussed. In the next chapter the actual samples studied in this thesis are described.

Chapter 4

Samples

A microcavity only exhibits strong coupling if it has been designed appropriately and the manufacturing technique provides excellent quality crystal growth. The coupling between exciton and photon depends on the square root of the photon field amplitude and its overlap with the exciton. To achieve maximum photon field the reflectivity of the DBRs should be as high as possible and the cavity length fixed at $\lambda/2$. The cavity reflectivity is determined by the number of layers and the refractive index contrast in the DBR. The surface of the layers must be as smooth as possible to prevent scattering, and the alloy composition as stable a possible to avoid fluctuations in refractive index and hence reflectivity. The exciton linewidth is determined by alloy fluctuations, QW width and material choice. If QWs are to be used within the cavity the photon-exciton overlap can be enhanced by using multiple quantum wells, however as the number of QWs increases, it becomes impossible to have them all situated at the anti node of the photon field in a $\lambda/2$ cavity. One solution to this problem is to increase the cavity length from the fundamental $\lambda/2$ to a higher order length, for example $3\lambda/2$. This provides multiple anti nodes within the cavity, allowing QWs to be spread between them. It is also desirable to have narrow quantum wells as this leads to an increase in oscillator strength and decrease in Bohr radius.

The highest quality samples are based on GaAs, where growth technology is well advanced and lattice mismatch is low. However, they require operation at liquid helium temperatures because the small exciton binding energy means that they are not stable

at higher temperatures. In order to study strong coupling at room temperature we have switched to GaN, a material system that exhibits excitons with binding energies > 20 meV.

4.1 GaAs Microcavity with InGaAs Quantum Wells

For low temperature studies on high quality GaAs based microcavities there are two options for the choice of the QW material, GaAs and InGaAs. GaAs has a smaller Bohr radius and higher oscillator strength and produces the narrower linewidth, however the heavy hole and light hole are close in energy, leading to more complicated dispersions. InGaAs has slightly broader linewidths and a reduced oscillator strength, however strain inherent within the QWs shifts the light hole to higher energies, simplifying the dispersion by only allowing strong coupling between the cavity and heavy hole without significant interaction with the light hole. In this thesis a GaAs microcavity containing InGaAs QWs was studied, as the dynamics are greatly simplified by the absence of the light hole resonance.

The sample is grown by metalorganic vapor-phase epitaxy (MOVPE) and consists of two pairs of three 100Å $In_{0.06}Ga_{0.94}As$ quantum wells in 100Å GaAs barriers embedded at each of the two anti nodes of the optical field, sandwiched between 17 (20) pairs of distributed Bragg reflectors $Al_{0.18}Ga_{0.82}As$/AlAs on top (bottom). The optical cavity length is $\sim 3\lambda/2$ and varies across the sample allowing access to both positive and negative detunings, $\Delta = \omega_{ex} - \omega_{cav}(\theta = 0)$, of the cavity resonance ω_{cav} from the exciton energy ω_{ex}. This structure exhibits a normal mode splitting at zero detuning of 7meV, with off resonance cavity and exciton linewidths of 0.5 and 1 meV, respectively.

4.2 Bulk GaN Microcavity

This microcavity sample is based on GaN and designed to work at room temperature. Unlike GaAs based microcavities, where the introduction of QWs generally optimizes light-matter coupling (due to the greater exciton-binding energy and better QW overlap

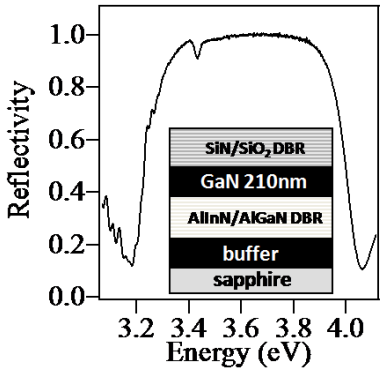

FIGURE 4.1: Schematic representation of the hybrid GaN microcavity structure with its measured reflectivity spectrum.

with the cavity standing wave), the nitride-based QWs currently exhibit broad linewidths and are plagued by the quantum-confined Stark effect [57]. Hence we use bulk GaN microcavities of a hybrid design (fig 4.1). The bulk $3\lambda/2$ GaN central spacer is sandwiched between a bottom 35 period $Al_{0.85}In_{0.15}N/Al_{0.2}Ga_{0.8}N$ DBR and a top 10 period dielectric SiO_2/Si_3N_4 DBR, as discussed in [58]. This choice of lower DBR is lattice matched, reducing the built-in tensile strain occurring during growth, preventing the formation of cracks and/or dislocations, and leading to a quality factor in excess of ~ 2800 in similar MC structures [59]. These large-area samples look transparent to the eye and are of high quality with few scattering defects.

4.3 GaN VCSEL

A GaN based VCSEL is used to compare the output polarisation of a pLaser with that of a standard laser. A crack-free planar hybrid $5\lambda/2$ GaN MC containing three InGaN QWs with a bottom lattice-matched (LM) AlInN/GaN DBR and a top dielectric ($SiO2/Si_3N_4$) DBR was grown by Ecole Polytechnique Federale de Lausanne. Figure 4.2 shows a schematic cross-section of the structure fabricated for this work.

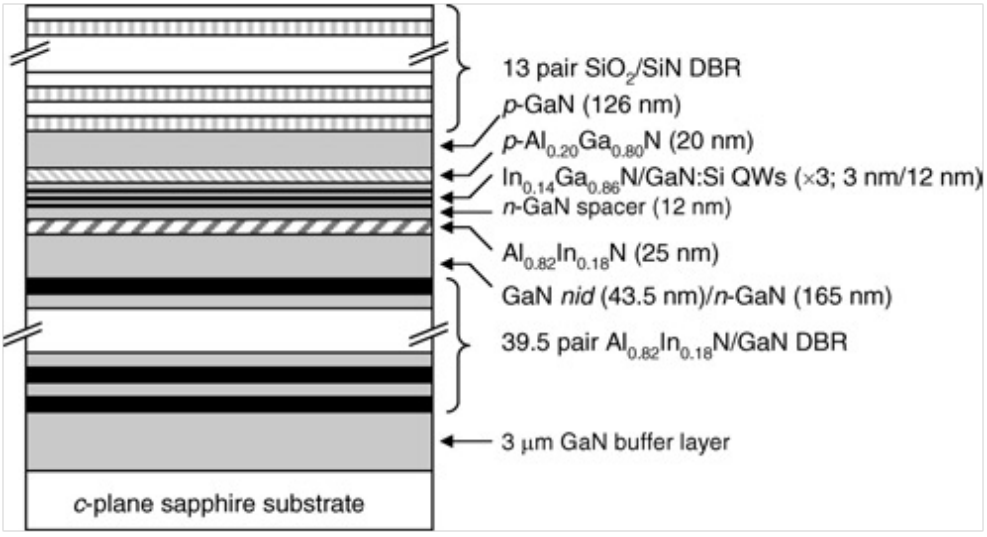

FIGURE 4.2: Schematic cross-section of GaN VCSEL structure.

Chapter 5

Experimental Techniques

The complexity of the physics governing semiconductor microcavities requires the measurement of many parameters to provide a comprehensive picture of the state of the system and the processes governing it. This chapter describes a variety of experimental techniques all based on optical spectroscopy. Such techniques allow investigation of scattering and relaxation processes, vital to the understanding of semiconductor microcavities. For example, chapter 6 investigates the dynamics of the microcavity OPO. To do this, the sample must first be characterised, this is done using the photoluminescence techniques described in section 5.3. Continuous wave and pulsed lasers are used to excite the system using the experimental configuration described in section 5.5. Then to gain further insight into the processes responsible for the dynamics, the spectral-temporal detection system, described in section 5.5, is employed.

5.1 Continuous Wave and Pulsed Lasers

One component common to all techniques is the use of laser light as an excitation tool. However the two material systems studied in this thesis require very different photon energies, with GaN requiring near ultra violet and GaAs near infra red wavelengths.

The primary pump laser source used for all of the laser systems is the Coherent Verdi solid state laser, which operates at 532nm and can give up to 18W of continuous wave

power. For experiments requiring continuous wave excitation in the near infrared red the Verdi pumps a Spectra Physics 3900s Titanium-doped sapphire (Ti:Al_2O_3, Ti:Sapphire) laser. A birefringent filter within the cavity is used to tune the output laser light in the region 700 - 1000 nm and can produce up to 500mW of output power. The same gain medium is to produce pulsed laser light required for time-resolved measurements. In this case a Coherent Mira 900-F, which produces near transform limited 150fs laser pulses with a 10nm bandwidth, is used. This system uses Kerr Lens Mode locking to produce 150fs pulses at a repetition rate of 76MHz. This system can also be tuned over the same wavelength range and gives a time-averaged power of 500mW, with a pulse energy of $\sim$7nJ.

Experiments on GaN require excitation in the UV. This is achieved by passing the output pulses of the Mira first through a Coherent RegA regenerative amplifier, which reduces the repetition rate to 250kHz and increases the pulse energy to 4μJ. However the pulses are still at 800nm. With the high pulse energies it is possible to use nonlinear mixing techniques to produce pulses of lower wavelength. This is done using a Coherent OPO 9400, which can be tuned to give pulses anywhere in the range 450 - 700nm. These pulses are then focussed down through a further mixing crystal (BBO) where a final frequency-doubling nonlinear interaction produces pulses in the range 270 - 400nm, limited by the allowed phase matching conditions determined by the cut of crystal. The resulting pulses are a few hundreds of femtoseconds in duration and have a time-averaged power of 10mW.

5.2 Reflection and Transmission Measurements

The previous chapter described how a wedge shaped cavity allowed for a variation in detuning between the exciton resonance and the cavity mode. Reflection and transmission measurements allow the mapping of such detuning variations without introducing a large population of carriers into the system.

The sample is either mounted on a sample holder (GaN) or on the cold finger of a large aperture continuous flow cryostat (GaAs). A heavily attenuated broadband light

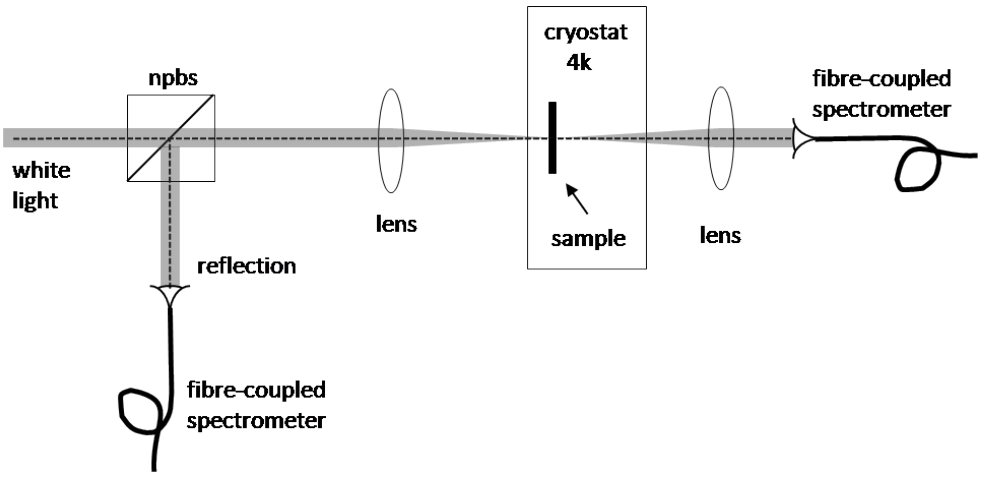

FIGURE 5.1: A schematic showing the setup used for reflection and transmission measurements when studying the detuning as a function of sample position. This particular example shows the extra beam splitter required for normal incidence reflection measurements.

source is directed onto the sample at a known angle and focussed down to a spot size of less than 100μm. The reflected/transmitted light is then collected and focussed into an optical fiber which is connected to a spectrometer. When studying the dependence of detuning on sample position the setup is constructed as in figure 5.1. The excitation and collection arms are fixed at normal incidence and the sample position scanned. However a full angle dispersion can be measured by removing the beam splitter and attaching separate excitation and collection optics to metal arms rotating around a pivot point directly below the sample.

5.3 Photoluminescence Measurements

Photoluminescence measurements allow study of the non-equilibrium emission of radiation from the sample. This occurs when an excited electron relaxes radiatively. In this thesis PL measurements have been used to map the dispersion of the polariton branches. A laser beam, tuned to a wavelength lower than that of the DBR stop band, injects carriers with energies greater than the polariton branches, this is typically referred to as 'hot injection'. The carriers then relax in energy, populating the polariton branches, before decaying radiatively. Collection optics similar to those used in transmission measurements are used to collect this photoluminescence. The angle of the collection arm

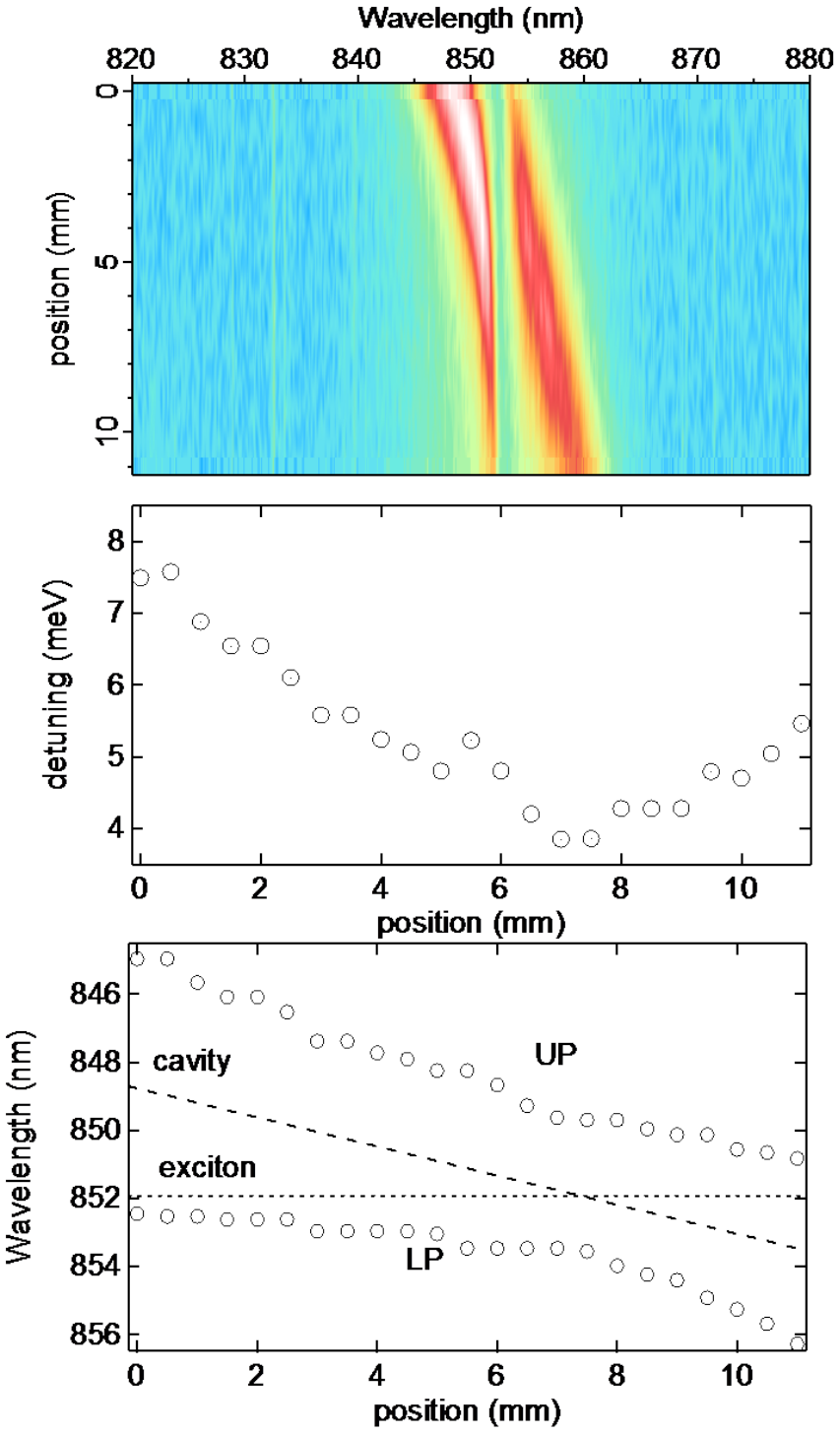

FIGURE 5.2: This is a typical detuning dependence seen on a GaAs sample. The sample is moved in 100μm steps over a range of more than 10mm. At each point a spectrum is measured and these are compiled to make the image shown in the top panel. In this image blue represents low counts, increasing through to red and then white. A clear anti crossing between the low wavelength upper polariton (UP) and the high wavelength lower polariton (LP) can be observed. The wavelengths of the UP and LP are extracted and plotted in the bottom panel, dotted lines indicating the position of the bare exciton and cavity modes are shown, the position at which they cross is zero detuning, which in this example is at 7.5mm. When zero detuning has been found it is then possible to plot detuning vs sample position as in the middle plot.

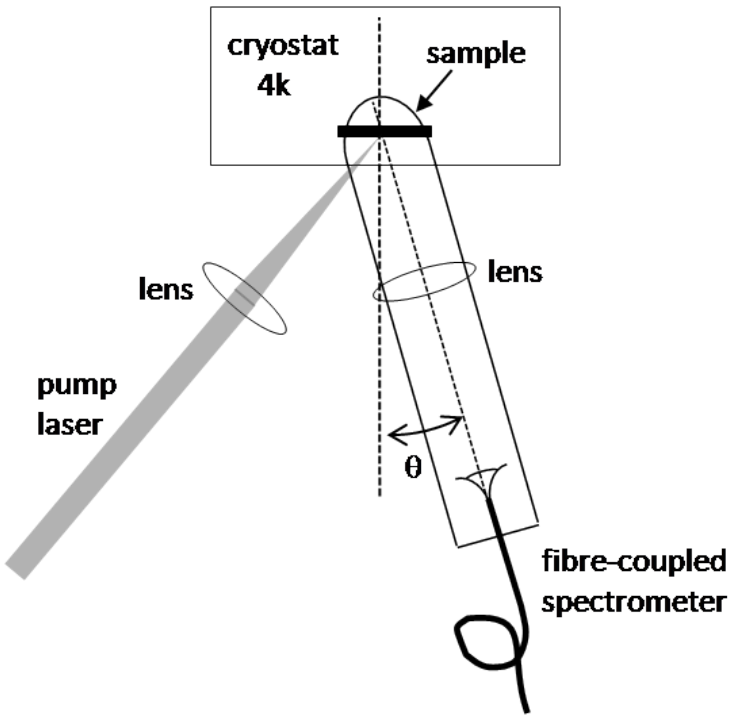

FIGURE 5.3: Schematic of a typical photoluminescence experimental setup. A high energy pump laser is focussed onto the sample to create carriers in the system. A lens collects the photoluminescence and focuses it down into a fibre coupled to a spectrometer. The collection system is mounted on an arm pivoted directly below the sample, allowing angle dependent measurements to be taken. In this example the sample is contained within a cryostat for studies at low temperatures.

allows emission angle and therefore in-plane momentum of the polaritons to be studied and a spectrometer gives information on their energy. Therefore it is possible to build a picture of exactly where the polaritons relax to within the dispersion before undergoing radiative relaxation. The ability to change the number of carriers in the system by controlling the power of the pump laser enables studies on population migration as a function of power. This is used when studying the bottleneck effect and can be used to show k-space collapses as in Chapter 8.

5.3.1 Imaging

Imaging techniques have been used in chapter 8 to show how polaritons collapse in real and momentum-space upon threshold in a room temperature polariton laser. This data also helps to support the the case of polariton BEC at room temperature. It is possible to image the photoluminescence using a combination of correctly arranged lenses (Figure 5.5). The simplest arrangement uses an achromatic lens to collect and collimate the

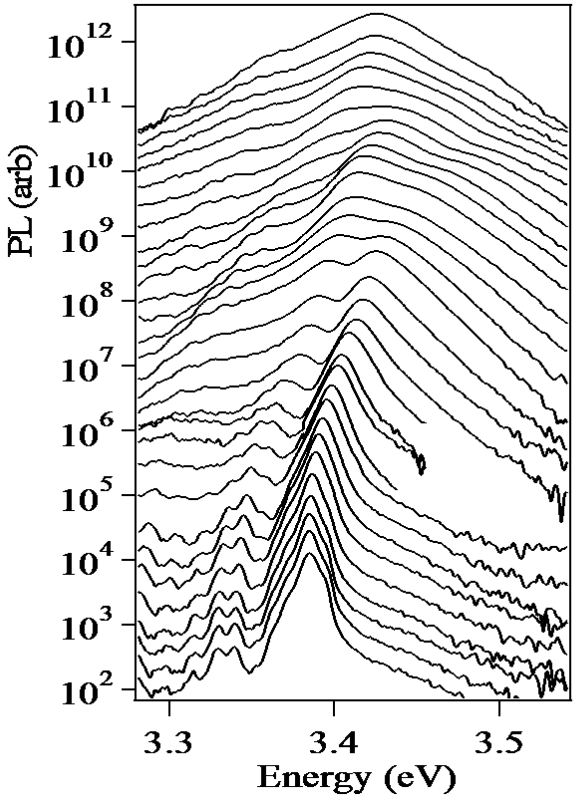

FIGURE 5.4: Typical PL data taken using the experimental setup of figure 5.3. Each trace is a spectrum taken at a different angle (angle increasing from 0^o (bottom) to 60^o(*top*). This particular data was taken from the GaN microcavity operating at room temperature.

photoluminescence (the sample placed at the focus of this lens) and then a second lens is used to focus the collimated light down to form an image. A CCD is used to record the image. The magnification of the imaging system is given by the ratio of the focal lengths of the two lenses. Figure 5.6 (a) shows the real space emission of a GaN microcavity pumped above threshold.

Momentum space can be imaged by removing the second lens in the imaging system, allowing collimated light to strike the CCD. Figure 5.6 (b) shows the k-space emission of a GaN microcavity pumped above threshold.

5.3.1.1 Momentum Space Imaging Post-Viva Amendment

The setup described for far-field (momentum space) imaging assumes that the photoluminescnence was emitted from an infinitely small spot in real space, in reality this is

not the case. Therefore Fourier optics should be considered in the design of the far-field imaging setup. In particular, a Fourier plane must be established, where a single emission angle from the entire real-space extent of the photoluminescence is mapped to a single position on the plane [60].

In the setup described above and shown schematically in Figure 5.5, a Fourier plane exists at one focal length behind the collection lens. In our experiment the CCD used to record the far-field images was situated at approximately thrice the focal length behind the collection lens, meaning that the was some mixing between the emission angles of photoluminescence from different positions on the sample. However, as described at the beginning of this chapter, another technique not relying on imaging was used to measure the angle dependence of the photoluminescence (Figure 5.3) and this showed very similar results to those gained using the imaging setup. Therefore, although the data collected using the imaging system is not as accurate as it could have been, it does still give a good representation of the angular emission profile of the photoluminescence.

5.3.2 First Order Coherence Measurements

Coherence measurements are used in chapter 8 to show that the emission from our room temperature polariton laser is first order coherent. The light emerging at $\pm 15^o$ to the sample is collected using a UV achromatic lens to collimate it. This beam is thus a far-field section of the angular emission. The beam is passed through a Michelson interferometer, figure 5.7, where the time delay between the arms can be varied.

The phase stability of the arrangement is such that observed fringes exhibit only slow drift (>1s). The far-field light from the two arms is overlapped on either a UV-sensitive CCD camera, or through an iris and onto a UV-sensitive PMT. By adjusting the angle between the two overlapped far field images which interfere, the fringe spacing can be adjusted. Images are recorded on the CCD over many thousands of emission pulses, for different time delays between the arms. By adjusting the iris diameter to be 10% of the fringe spacing, separate measurements of the visibility can be taken as the PZT is scanned. Because this measurement is over a small region in the far-field k-plane, it corresponds to integrating the first order coherence over the real space spot.

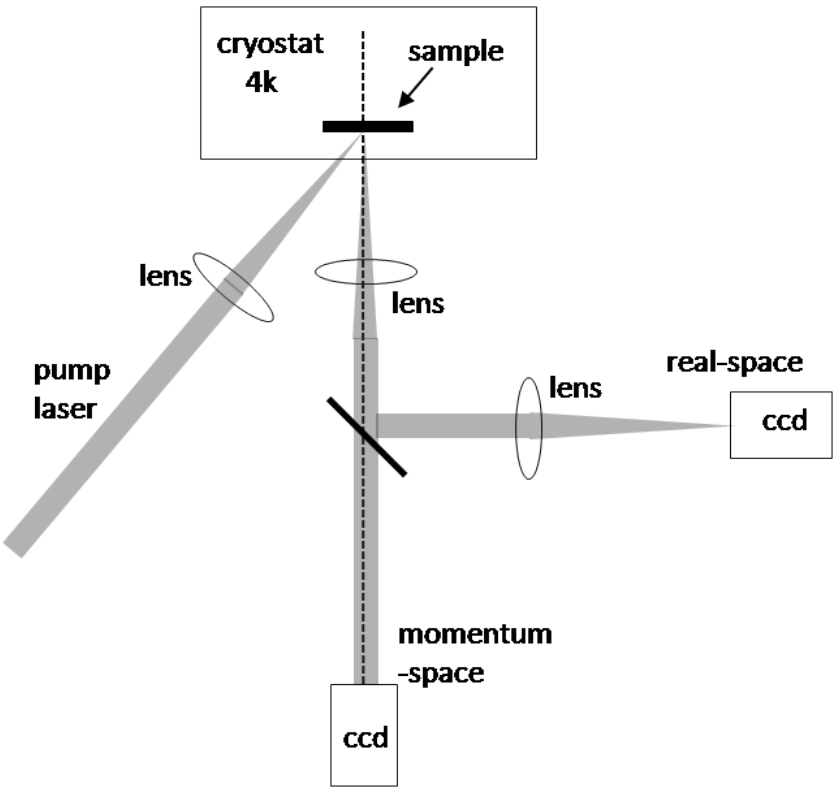

FIGURE 5.5: The normal incidence photoluminescence is collected using an achromatic lens. The resulting collimated light can be directed straight onto a CCD for momentum space imaging, or be focused down using a second achromatic lens for real-space imaging. The ratio of the focal lengths of the two lenses involved in the real space imaging setup determines the magnification of the image. Please see section 5.3.1.1 for a discussion on the shortcomings of this design.

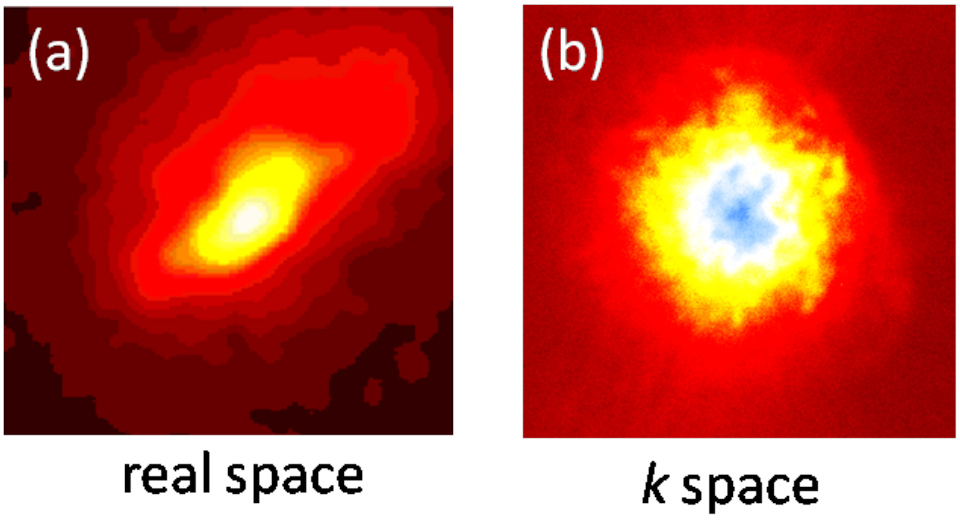

FIGURE 5.6: Figure (a) shows the real space image of photoluminescence from a GaN microcavity pumped above threshold, the real space dimensions of the image are 100 x 100 μm. Figure (b) shows the k-space image from the same situation, the image shows $\pm 15^{o}$ of emission.

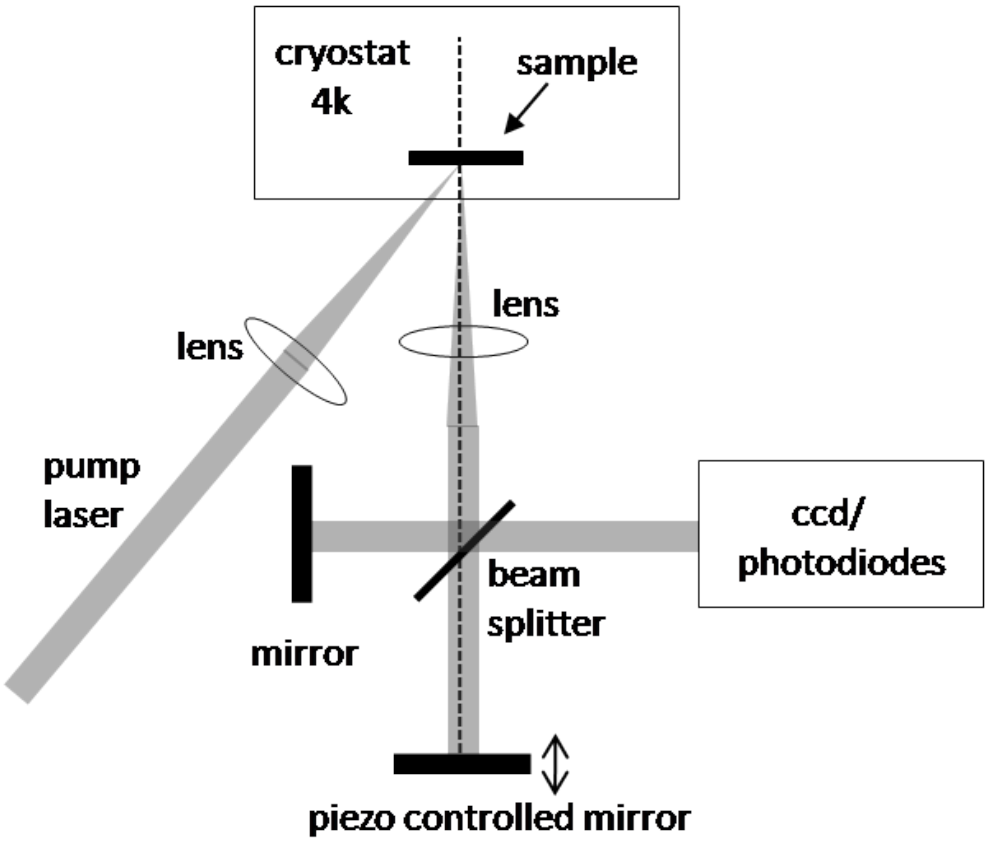

FIGURE 5.7: The first order coherence is studied by passing collimated normal incidence photoluminescence through a Michelson interferometer. One arm has a fixed length and the second, while the second is controlled by a micrometer stage and piezo electric transducer. The resulting interference pattern is recorded on a CCD. Increased dynamic range is achieved by passing a small section of the interference pattern to a photomultiplier tube and slowly oscillating the length of one arm of the interferometer with the PZT.

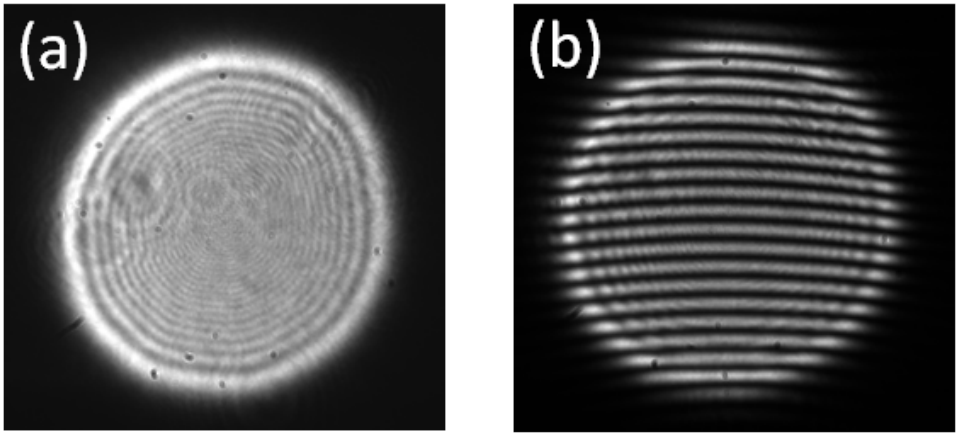

FIGURE 5.8: Figure (a) shows the image that results when one arm of the first order coherence setup is blocked. There is no interference and therefore the k-space emission is imaged. Figure (b) shows the clear interference pattern resulting from interference of the beams when the arms of the interferometer are set to have similar lengths.

5.4 Polarisation Measurements (single shot and time integrated)

In chapter 8, it is shown that a room temperature Bose-Einstein condensate can be produced in our GaN microcavity. The critical piece of data supporting this is the shot-to-shot polarisation statistics. Polarisation is an order parameter of the system and the statistics show spontaneous symmetry-breaking, required to prove BEC.

Light emerging at $\pm 15^o$ to the sample is collected using a UV achromatic lens and collimated. The light passes through broadband UV wave plates (half-wave and quarter-wave) before being split by polarisation beam splitters (care has to be taken over the angular acceptance and alignment of these optics). In the experiments which use repeated measurement of one polarisation basis, a single polarisation beam splitter is used, and the two emerging beams are individually focussed on to detectors. For Streak camera measurements, they are focussed onto different positions of the input slit of the Streak camera, and their optical paths made equal so that the two polarisation components of each pulse appear at the same time position on the streak image, figure 5.10. The streak camera is manually triggered, with a gain sufficient to record the relatively weak emission, and many iterations of this procedure produce images from which the intensity of each polarisation component, averaged over each laser shot, can be extracted. UV-sensitive photo multipliers (PMTs) can be used instead of the streak camera, with a temporal response of <100ns, and after pre-amplification and pulse clean up electronics, these are recorded using a PC-based ADC card with sample-and-hold facility which records simultaneous measurements on all channels. The overall time resolution of the system is $< 1\mu$s, and allows extraction of the intensity of each polarisation component for each pulse, over thousands of successive shots (fig 5.10 (a)). To allow calibration of the system a half wave plate is used to swap the polarisation basis between PMTs. By splitting the emission into two extra beams using two additional polarisation-independent beam splitters at near normal incidence, 4 PMTs can simultaneously record pulses (for instance along Horizontal, Vertical, Diagonal, Right-circular bases) allowing complete reconstruction of the full Stokes parameters. Linearly polarised laser light is used to calibrate the system and confirm that no artifacts are present from the polarisation

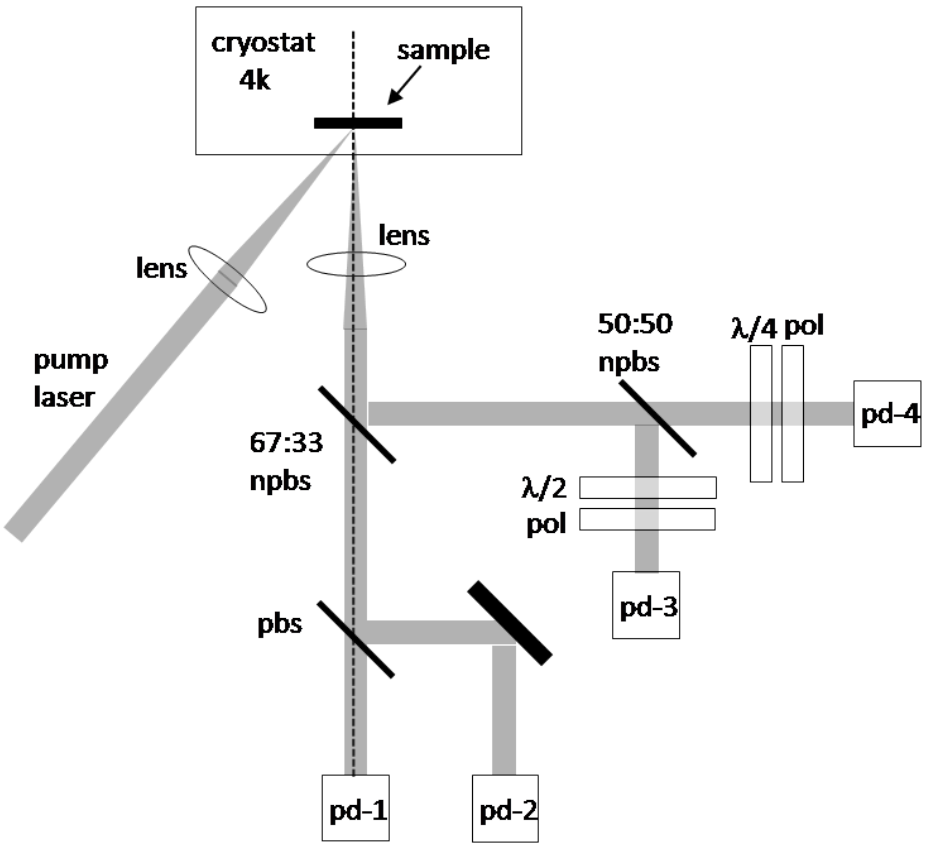

FIGURE 5.9: Schematic showing the experimental setup for measuring the single shot polarisation of the photoluminescence from a GaN microcavity. An achromatic UV lens collimates the normal incidence PL, this is then sent through a combination of beam splitters and wave plates and polarisers, such that all four of the Stokes parameters can be measured. The repetition rate of the laser is reduced to 100kHz, giving enough time between pulses for the PMTs to recover.

splitting optics. Electronic noise in the detection produces a background polarisation degree in addition to that contained within the optical signal. Hence even perfectly polarised input produces a polarisation histogram with some deviation about the average polarisation. For signal to noise in our measurements this is approximately 8%.

5.5 Pump-Kick

The pump-kick technique is used to study the temporal dynamics of the microcavity system, figure 5.11. A continuous wave laser is incident on the sample at 16 degrees and tuned to an energy suitable for the operation of the micro-OPO described in section 6. A pulsed laser beam (named the kick) is also incident on the sample and arranged to overlap spatially with the continuous wave beam. The kick excites from the back side

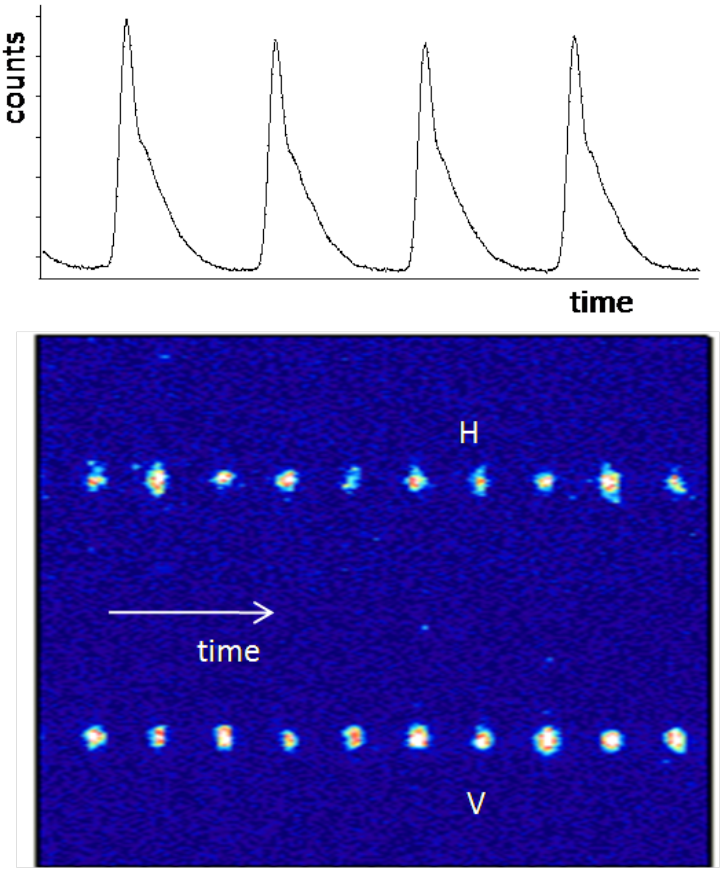

FIGURE 5.10: Figure (a) shows the pulses recorded by one of the PMTs. Figure (b) shows how a streak camera can be used to replace two of the PMTs to simultaneously measure one of the Stokes parameters.

of the sample, so as to not interfere with the pump optics, and can be set to any angle. An achromatic lens is used to collect and collimate the emission at normal incidence to the sample. This is then focussed onto a streak camera, which enables the intensity of the emitted light to be measured with a time resolution of a few ps.

5.5.1 Spectral-temporal measurements

The self interaction of polaritons leads to a blue shift of the polariton modes. Therefore population can be ascertained by measuring the energy of the photoluminescence. Spectral-temporal information can be gained by coupling an imaging spectrometer to the streak camera. The light passes through the spectrometer, which images in the vertical plane and spreads the wavelengths in the horizontal plane. An image is produced on its output slit and a pair of lenses image this onto the entrance slit of the streak

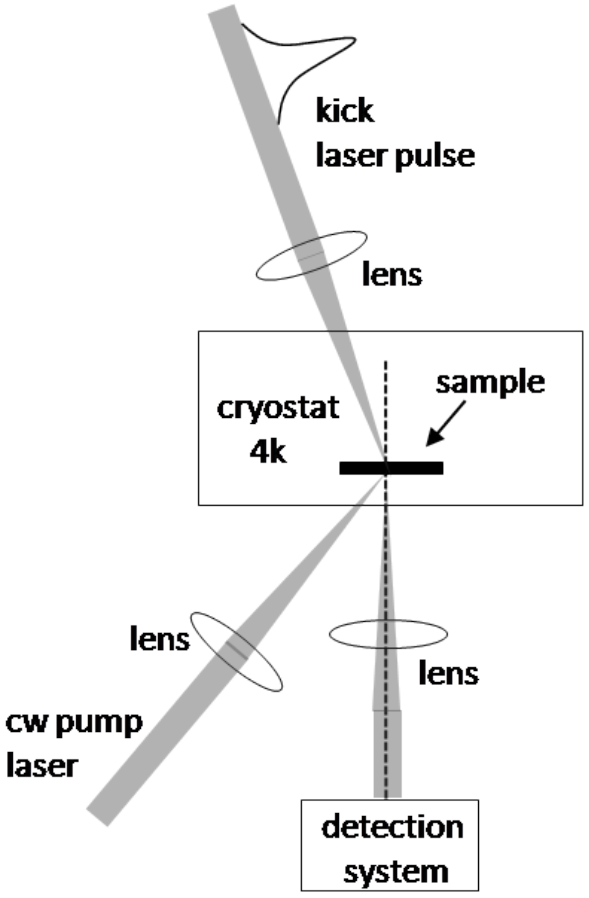

FIGURE 5.11: A cw pump laser is incident on the sample and tuned so that the microcavity operates as an OPO. A pulsed laser is directed onto the sample from the opposite side and overlapped with the pump spot. The pulsed laser is designed to perturb the operation of the OPO. A lens is used to collect and collimate the normal incidence emission. A streak camera is used to record the temporal dynamics of the emission intensity.

camera, Figure 5.11. The result is a streak image that has wavelength on its horizontal axis, time on the vertical, and colour scaling representing intensity. An example of such data is shown in figure 5.12

5.5.2 Time-resolved Imaging

Spatio-temporal information is gained by imaging the photoluminescence from the sample onto the entrance slit of the streak camera. However, the input slit required to achieve high time resolution means that the streak camera can only image in one dimension (a slice of the 2 dimensional image). In order to recreate the full two dimensional image a piezo electric transducer is attached to a mirror mount, which directs the image

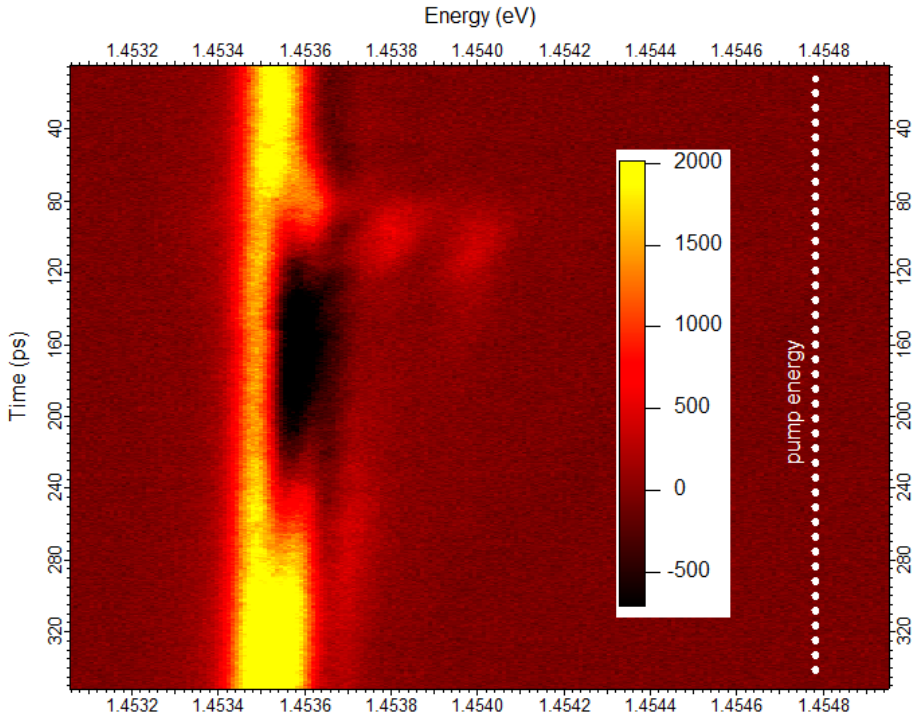

FIGURE 5.12: Temporally and spectrally resolved data. The perturbation kick pulse arrives at $t = 80$ ps.

onto the streak slit. The PZT moves in small steps, translating the two-dimensional image across the input slit of the streak camera, at each step a streak image is taken (Fig 5.13). When the entire image has been translated across the slit, the data from the streak camera can be complied. This essentially allows two-dimensional movies, in real or momentum space, to be recorded with a time resolution of a few ps. Frames from such movies are presented in chapter 7.

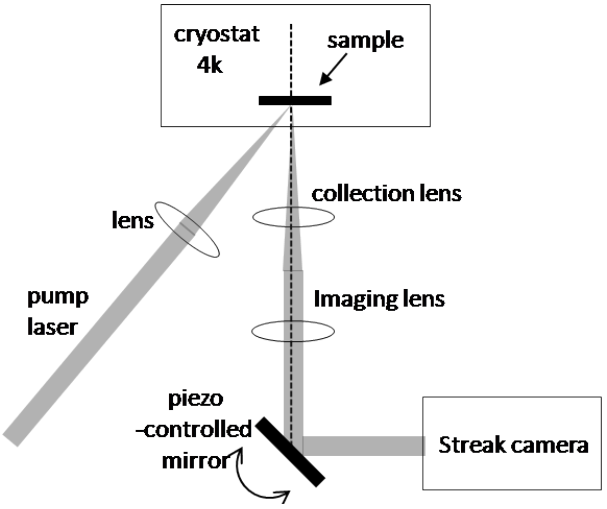

FIGURE 5.13: A piezo electric transducer replaces the actuator of a mirror mount. This allows the controlled scanning of an image across the streak input slit. At each position a streak image is recorded. This data can be compiled to produce a movie of the real space emission of the microcavity with a temporal resolution of a few picoseconds.

Chapter 6

Temporal Dynamics of the Polariton Optical Parametric Oscillator

In 2000, Baumberg *et al* demonstrated the operation of an optical parametric oscillator (OPO) in a semiconductor microcavity. The substantially reduced threshold and smaller size of the microcavity compared to conventional crystal based OPOs has ignited interest in the development of such systems. The drawback of the initial experiments was their need to be performed at liquid helium temperatures. However, while material growth technology is being driven forward to enable operation of microcavity OPOs at room temperature, as will be discussed in chapter 8, in this chapter we study the properties of the OPO operating at liquid helium temperatures.

There has been little experimental research into the temporal dynamics of the microcavity OPO system and particularly how it reacts to perturbations in pumping power. In this chapter we report on experimental studies of the perturbation dynamics in the GaAs based sample detailed in Section 4.1. An optical pulse is injected into a working CW OPO to perturb it from an equilibrium state. The dynamics are studied by observing the temporal dynamics of the OPO signal emission intensity. A model is constructed to

explain the experimental results before conclusions are drawn on the physical processes that govern the dynamics.

6.1 Optical Parametric Oscillators

OPOs are nonlinear resonators oscillating at optical frequencies in which a coherent pump wave is converted into coherent 'signal' and 'idler' waves of different frequencies. Conventionally OPOs are based on nonlinear $\chi^{(2)}$ crystals and have been successfully commercialised, but they also provide an almost unique environment for research into non-classical phenomenon such as quantum entanglement [61]. In 2000 Baumberg *et al* [11] reported the use of a semiconductor microcavity as an OPO, shrinking the size of the device by a factor of 10,000. This was made possible because the polariton trap present in the lower polariton branch of the microcavity dispersion efficiently channels energy from the pump via a $\chi^{(3)}$ parametric scattering process. Figure 6.1 shows a cartoon representation of the dispersion, indicating the position of the OPO states and the scattering process. The pump, signal and idler states are all resonant within the system and these interact via the Coulomb interaction of the excitons. The quantum properties of the microcavity inhibit spontaneous emission into non oscillating modes and enhance the stimulated scattering. These combine to reduce the threshold compared to nonlinear crystal systems by more than 100 [11].

6.2 Modelling the OPO

The microcavity OPO reported in 2000 [11] was operated in the steady state regime, under continuous wave excitation. In this section we will build a simple model to describe the system and use it to fit some experimental data. The model will then be extended in later sections to help describe the dynamics of the OPO.

As is indicated in figure 6.1, the microcavity OPO operates on the LPB of the dispersion of the semiconductor microcavity. The LPB contains many states at differing k values. However modelling the interactions of such a large number of states is a complicated

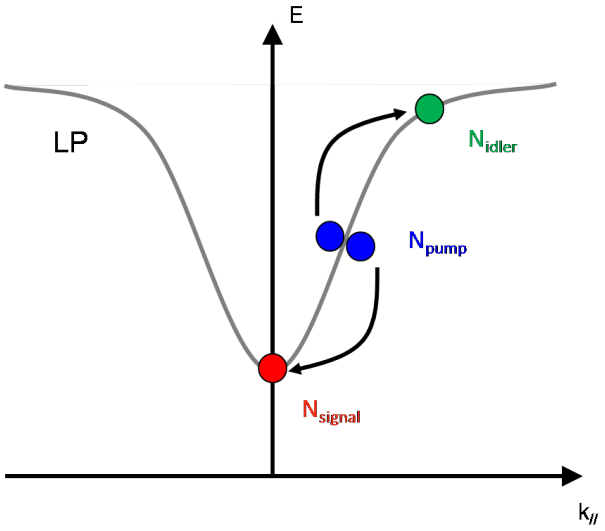

FIGURE 6.1: A cartoon showing the polariton dispersion with the positions of the pump, signal and idler states. The arrows represent the parametric scattering process, where two polaritons in the pump state scatter to the signal and idler state. The scattering process is efficient as energy and momentum are conserved.

procedure requiring a large amount of computer processing power. Therefore to simplify the theoretical approach we reduce the number of states described by the model to just three. The first state is defined by the angle of incidence and energy of the excitation laser, which injects polaritons into the system. This state is named the 'pump' state and resides at the point of inflection on the LPB. In our system this corresponds to an excitation angle of 16 degrees and an excitation energy, $\omega_{cw} = 1.452$ eV. The other two states are defined by the energy and momentum conservation laws:

$$2\epsilon_p = \epsilon_s + \epsilon_i \tag{6.1}$$

$$2k_p = k_s + k_i \tag{6.2}$$

where ϵ is the energy and k the in-plane momentum of pump (p), signal (s) and idler (i) states respectively.

The unique shape of the LPB, coupled with the assumption that only a single pump state is populated by the excitation laser, means that there is only one combination of signal and idler states that satisfy these conservation laws. The signal state is at the

bottom of the polariton trap, with zero in-plane momentum, and therefore the idler has twice the in-plane momentum of the pump state, at an angle of 32 degrees to normal incidence.

The Hamiltonian in Appendix A has been used to create a set of rate equations, describing the evolution of the population of each state in time:

$$\frac{dN_s}{dt} = -\frac{N_s}{\tau_s} + \frac{2}{\hbar} IM\{VC\} \tag{6.3}$$

$$\frac{dN_i}{dt} = -\frac{N_i}{\tau_i} + \frac{2}{\hbar} IM\{VC\} \tag{6.4}$$

$$\frac{dN_p}{dt} = -\frac{N_p}{\tau_i} - \frac{4}{\hbar} IM\{VC\} + F \tag{6.5}$$

$$\begin{aligned}\frac{dC}{dt} = &-\left(\frac{1}{2\tau_s} + \frac{1}{2\tau_i} + \frac{1}{\tau_p}\right) C \\ &+ \frac{i}{\hbar}\left[(\epsilon_s + \epsilon_i - 2\epsilon_p) + \frac{i}{\hbar} U(X_i + X_s - 2X_p)(X_i N_i + X_s N_s + X_p N_p)\right] C \\ &+ \frac{iV}{\hbar}\left[N_p^2(N_s + N_i + 1) - 4N_s N_i (N_p + 1)\right]\end{aligned} \tag{6.6}$$

where N is the population, τ the lifetime, and ϵ the energy of the signal (s), pump (p) and idler (i) states, V is the interaction constant, F describes injection of polaritons via an external pump, and X is the excitonic fraction given by equation 2.24. The fourth equation describes the dynamics of a complex correlation term, controlling the interaction between the states. It is constructed of three terms: the first describes a reduction in correlation due to decay of the polaritons, the second describes a change in correlation due to self interaction of the polaritons resulting in a renormalisation of the lower polariton branch [62], and the third term describes both spontaneous and stimulated scattering of polaritons between the states.

This is of course a simplified model. The dispersion contains many states at different k, and in reality scattering could take place between any two states. An example would be two polaritons in the signal state scattering from each other, one to the pump state and one to another state with energy $\epsilon = \epsilon_s - (\epsilon_p - \epsilon_s)$ and wave vector $k = k_s - (k_p - k_s)$; such off-branch processes have been studied by Savvidis *et al* [63]. Importantly, these

off-branch scattering events have a low probability of occurring, justifying their exclusion from the model. A further simplification is the assumption that the pump is a plane wave, and therefore there is no variation in real space, of course in an experiment the pump state is excited optically by a laser beam with a Gaussian profile, therefore the effective size of the pump term F and hence the population of polaritons is not a constant in space. Such effects will be investigated further in Chapter 7.

6.2.1 Steady-State

Experimental results show that for all pump powers the system settles down into steady state operation [11]. As the system reaches a steady state, we can assume that the blueshift terms do not affect the resonance condition of the OPO. Therefore the theoretical model shall be simplified by removing the blueshift term in equation 6.6. In doing this the complex correlation function c remains purely imaginary, and we explicitly use $C = Im(c)$. We also make the assumption that the decay rate τ is the same for all three states and define $\kappa = 1/\tau$. In reality the 3 states have slightly different decay rates, however this assumption should make no significant difference to the dynamics of the system but will allow steady state solutions to be solved easily. The rate equations describing the system now become:

$$\dot{N}_p = -\kappa N_p - 4Dc + F \tag{6.7}$$

$$\dot{N}_i = -\kappa N_i + 2DC \tag{6.8}$$

$$\dot{N}_s = -\kappa N_s + 2DC \tag{6.9}$$

$$\dot{c} = -2\kappa c + D\left[N_p^2(1 + N_s + N_i) - 4N_s N_i(N_p + 1)\right] \tag{6.10}$$

where $D = V/\hbar$ is the redefined coupling constant.

If the pump term, F is fixed and has no time dependence then a steady-state equilibrium condition can be reached. The system of equations can then be solved to give:

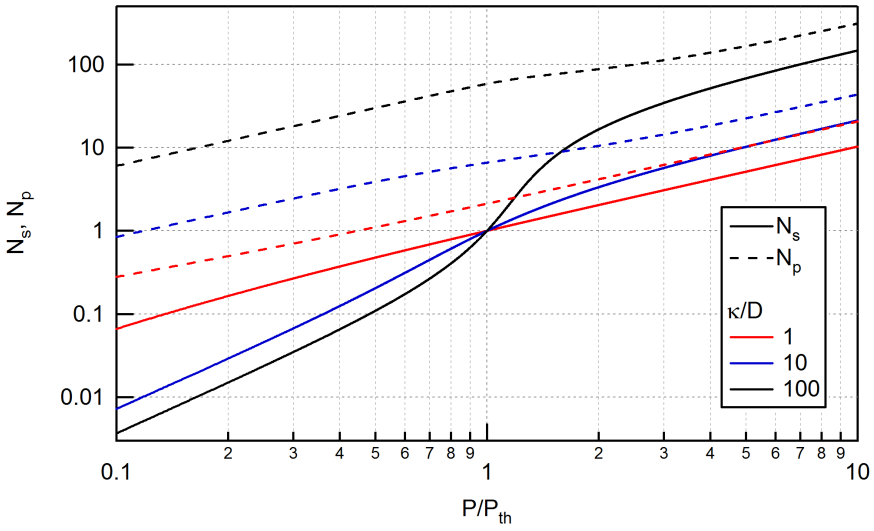

FIGURE 6.2: A comparison between the steady state power dependence of the OPO system for different ratios of κ/D, the decay rate and interaction constant respectively. Population of the signal state, N_s and pump state N_p are plotted against input power. The input power is normalised to a threshold value calculated using equation 6.16. A clear threshold is not achieved unless $\kappa \gg D$.

$$N_s = \frac{2D}{\kappa}C = N_i \equiv N \tag{6.11}$$

$$N_p = \frac{F}{\kappa} - 2N_s \equiv f - 2N \tag{6.12}$$

$$2\kappa C = \frac{\kappa^2}{D}N = D\left[(f-2N)^2(1+2N) - 4N^2(f-2N+1)\right] \tag{6.13}$$

where $f = F/\kappa$.

This leads to a cubic equation in the equilibrium signal population,

$$16N^3 - 12fN^2 + \left(2f^2 - 4f - \frac{\kappa^2}{D^2}\right)N + f^2 = 0 \tag{6.14}$$

The solution of this equation depends only on the pump rate f and the ratio $\frac{\kappa}{D}$ as expected. κ is given by the linewidth of the polariton mode. This is measured experimentally to be ∼0.5 meV. D is the interaction constant and can be estimated from the blueshift [1] of the LPB at threshold to be ≤0.25 meV. Therefore $\kappa/D \geq 2$ in our

[1] from [64] the blueshift $\tilde{\epsilon_s} = 2DN_s$, the blueshift just above threshold is measured to be ∼0.5meV. At threshold N_s= 1 by definition, therefore D≤0.25meV

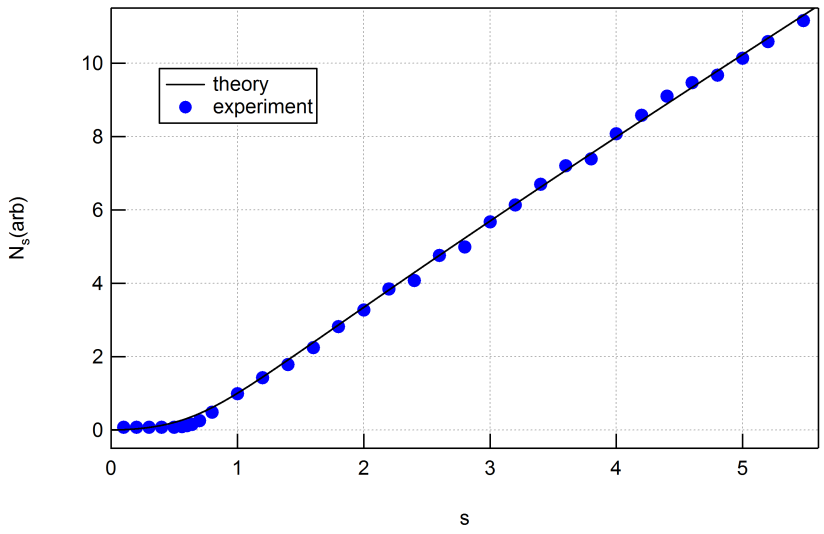

FIGURE 6.3: Experimental data for the power dependence of the steady-state OPO (blue dots) is overlaid with that of the theoretical model detailed in equation 6.14. A κ/D ratio of 10 was found to fit best.

system. The theoretical solutions for the dependence of N_s and N_p on F are shown for values of $\frac{\kappa}{D} = 1, 10, 100$ in figure 6.2. Several features are evident. Only if $\kappa \gg D$ does a pronounced threshold appear with a quadratic region at low pump powers and a linear-like region above threshold. As $\kappa \sim D$, the threshold is washed out and a truly thresholdless OPO results. Figure 6.3 shows a fit to experimental data, from this we can conclude that in our system $\frac{\kappa}{D} \sim 10$, which is in good agreement with the estimate of $D \geq 2$ made using the linewidth and blueshift measurements.

The threshold pump rate can be found by solving (6.14) for the condition in which the signal state population reaches unity, $N_s = 1$. This leads to a quadratic in the pump rate, f_{th}

$$\frac{3}{16} f_{th}^2 - f_{th} + 1 - \left(\frac{\kappa}{4D}\right)^2 = 0 \tag{6.15}$$

which leads to

$$f_{th} = \frac{8}{3}\left[1 + \frac{1}{2}\sqrt{1 + 3\left(\frac{\kappa}{4D}\right)^2}\right] \tag{6.16}$$

Henceforth we use the scaled pump power $s = f/f_{th}$ to describe the operating condition of the OPO.

6.2.2 Steady State Band Renormalisation

Earlier in this section we made a simplification to our model by removing the polariton self interaction terms from the complex correlation function. This simplification contradicts a theoretical stability analysis of the microcavity OPO by Whittaker [65]. He found that for a particular pump excitation energy, ϵ_p, there exists an upper threshold pump power, above which the OPO is no longer stable. This is due to the renormalisation of the lower polariton branch, in response to polariton self interaction. Thus his model predicts that the OPO should turn off above a certain pump power. We have investigated this experimentally by performing two power dependences, as shown in figure 6.4. The black diamonds show the power dependence when the pump energy is tuned to give optimum signal power for each pump power, and the red circles in the figure show the dependence when the energy of the CW pump is fixed at that energy giving the optimum signal just above threshold. In both cases at low powers there is very little emission from the signal state, and what is measured is due to spontaneous emission. However beyond a threshold pump power, the OPO switches on. This occurs when the population of the signal state reaches unity and stimulated scattering is turned on. The horizontal axis of the graph has been rescaled to show pump power normalised to this threshold power. For powers at and slightly above threshold the two curves follow a similar trend, however when the normalised pump power, $s \sim 1.5$ the two curves begin to deviate from one another. In the case of fixed pump energy the rate of increase of the OPO signal power begins to drop. On the same graph the energy of the OPO emission is plotted for the case when ϵ_p is fixed. Just above threshold ϵ_s begins to increase, i.e. the lower polariton branch is renormalised and blueshifts, however as the pump power is increased further the emission energy clamps. This is because the conservation conditions stated in equations 6.1 and 6.2 determine the emission energy, and the states cannot move more than their linewidth (0.5 meV) away from these resonance energies.

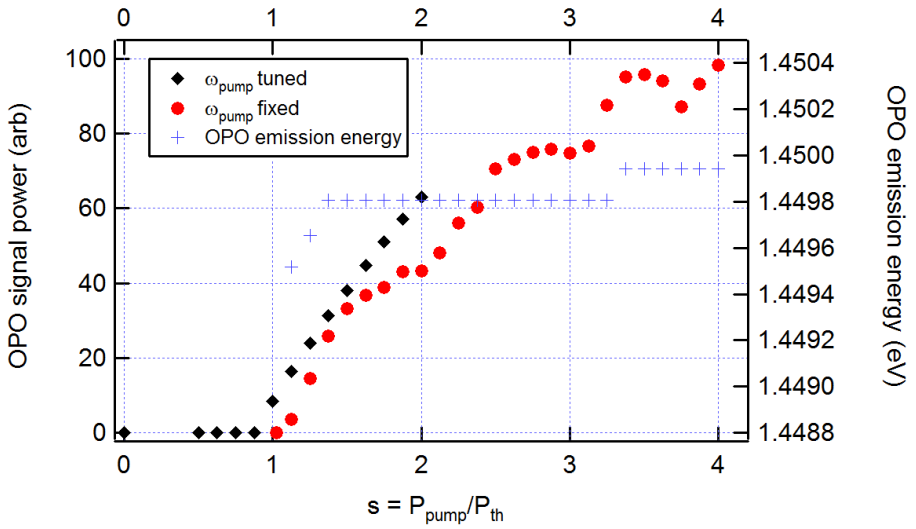

FIGURE 6.4: Data showing the power dependence of the OPO emission for two pumping conditions. In one case the pump energy is fixed (red circles) and in the other it is tuned with power to give optimum signal (black diamonds). The blue crosses show the energy of the OPO emission in the case of fixed pump energy.

Whittaker [65] explains this result as a consequence of the plane wave approximation used in the OPO model. In reality the Gaussian profile of the pump spot means that for high pump powers, the regions in the centre of the spot cross the upper threshold and the OPO switches off, yet for the same power regions in the tail of the Gaussian become sufficiently populated that the OPO turns on. The effect is that for spatially integrated experiments, as described in this chapter, the signal emission does not turn off for pump powers above the threshold when the pump energy is fixed. Inclusion of the energy shifts in our steady state model would mean that an equilibrium condition would not be reached for range of pump powers. We have shown that this is not the case experimentally and therefore justify its exclusion from the steady state model. However, energy shifts are clearly present in the system and will be reintroduced to the model once a steady state solution has been reached.

6.3 Dynamics Under Perturbation

In the previous section the concept of the microcavity OPO was introduced and a simple model was created to describe the population of the OPO states under continuous wave

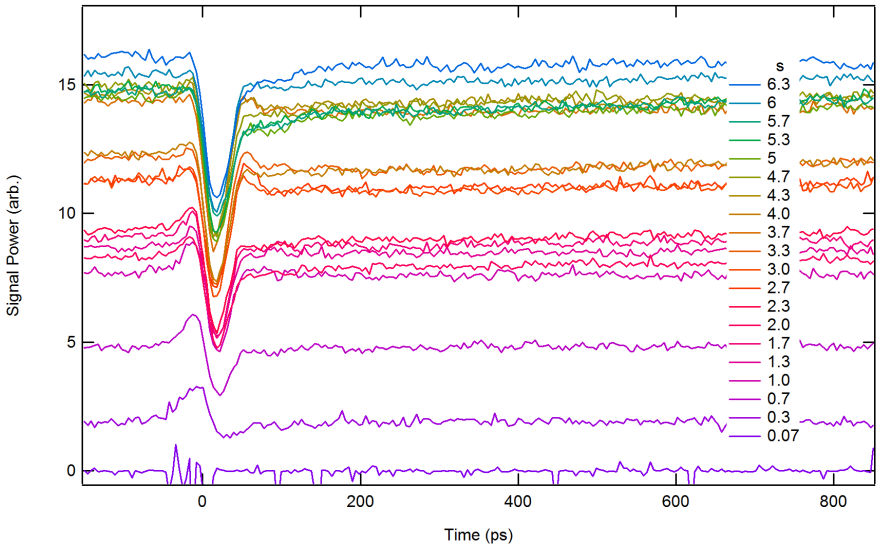

FIGURE 6.5: Experimental results showing the dependence of the perturbation dynamics of the OPO as a function of cw pump power, F. Below threshold (25mW) the perturbation acts to increase the signal emission. Above threshold however the perturbation causes a dip in the signal emission intensity. The time of the dip is below that of the resolution of the detector (10ps). Notice that the depth of the dip is dependent on s.

pumping. In order to understand more about the interactions and processes governing the OPO, we now introduce an experiment to perturb it from its equilibrium state, allowing its recovery dynamics to be observed. This is achieved experimentally using the pump-kick technique described in section 5.5. It uses a continuous wave excitation laser, as in the previous section, to create a steady state OPO at equilibrium. A $\sim$1 ps laser pulse, with a bandwidth of 1 nm is then incident on the pump state, rapidly injecting polaritons, transiently increasing the population of the state N_p. This 'perturbs' the system by taking it out of equilibrium. It will stay out of equilibrium until the surplus polaritons decay from the system. Scattering between polaritons allows their redistribution between the three OPO states during this period of perturbation. This redistribution will be tracked experimentally by temporally resolving the output intensity of the signal state using a streak camera; the number of photons emitted is proportional to the number of polaritons in the state.

The power of the perturbing pulse, referred to as the 'kick', is chosen such that it injects approximately 10 times the number of polaritons into the system as the cw pump at

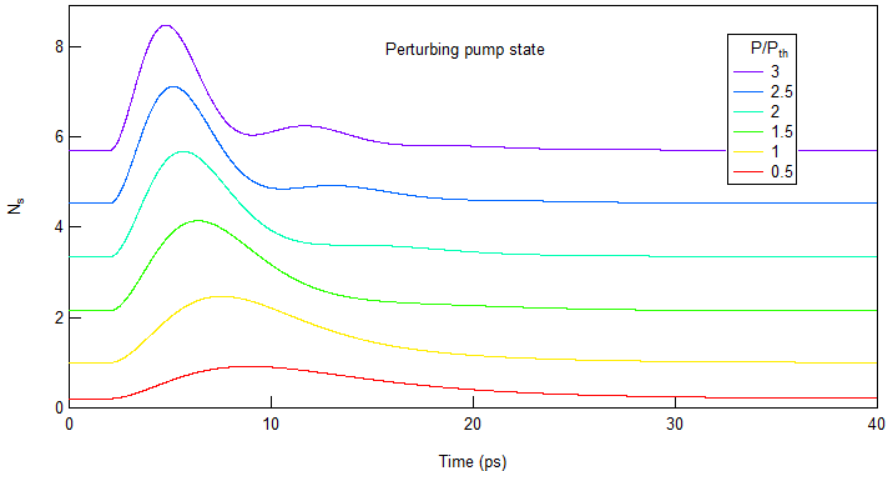

FIGURE 6.6: Plots showing how the theoretical model reacts to a perturbation of the pump state. In this case the perturbation is defined as a transient increase in the pump population. Although the timescale of the dynamics is correct, it unfortunately predicts an increase in N_s and does not fit the experimental data.

threshold[2]. Figure 6.5 shows the temporal response of the signal state as a function of the normalised cw pump power, s. It can be seen that when the OPO is pumped below threshold ($s < 1$), the effect of the perturbation is to increase the signal population. This can be explained as either an increase in the spontaneous scattering from the pump state to the signal state, or momentary 'turn-on' of the OPO. As $s > 1$ the nature of the dynamics changes completely. In these circumstances the perturbation causes a *decrease* in N_s. This transient 'dip' in N_s, recovers on a timescale within the resolution limit of the detection system (10ps). It is also apparent that the depth of the dip depends on s, this trend is discussed later.

In order to model this experiment, the pump term in equation 6.7 is redefined to have both time-dependent and time-independent components:

$$F = F_{cw} + F_{kick}(t). \tag{6.17}$$

The system is simulated for a range of values of s and the resulting traces are shown in figure 6.6. Initially running in its steady state, at some time, t_k, the kick pulse injects

[2]The kick pulse has a time-averaged power of $\sim$ 0.1 mW and repetition rate of 80 MHz resulting in $\sim$1 pJ per nanosecond pulse, the overlap of pulse spectrum with the LPB mean that $\sim$ 10% of this is absorbed by the system, so approximately 0.1 pJ is injected per pulse. The cw laser has a time averaged power of $\sim$10mW, therefore in 1 ps 0.01 pJ are transferred.

polaritons into the pump state. The model shows an increase in the signal population for all values of s. In its current form the model is just a system of coupled non-linear oscillators. It therefore exhibits the usual dynamics of relaxation oscillations, whose frequency depends on population and the damping coefficients (in our case κ). In the polariton system, these are a result of final state stimulated scattering, a feature of Boson statistics. As s is increased, N_s and N_i increase accordingly, therefore stimulated scattering is enhanced and the rate at which polaritons are 'sucked' into the signal state from the pump state increases. For very high values of s the population of the states become sufficiently large that stimulated backscattering becomes important and the system goes into oscillation.

Although the model shows many interesting features, it does not recreate the transient dip in N_s seen experimentally. Polariton self interaction must be added to account for the reduction in signal emission upon perturbation.

6.3.1 Blueshift Effects

As discussed earlier in the chapter, the self interaction of polaritons leads to a blueshift of the polariton branches. Theoretically this leads to an upper threshold [65], above which the OPO is no longer resonant and switches off. However, complete switching off the OPO is not seen experimentally and the discrepancy is thought to be due to the plane wave approximation in the theory. In order to model the steady state OPO, the blueshift term was removed from the correlation function and this model gave a good match to the steady state power dependence measured when tuning the pump energy with power. However, this simplified model is not able to reproduce the temporal dynamics shown in figure 6.6.

We define the blueshift of the LPB at the pump state, $\tilde{\epsilon_p}$ as the difference in energy between the LPB under perturbation, ω_p and in steady state operation, ω_p^0.

$$\tilde{\epsilon_p} = \omega_p - \omega_p^0 \tag{6.18}$$

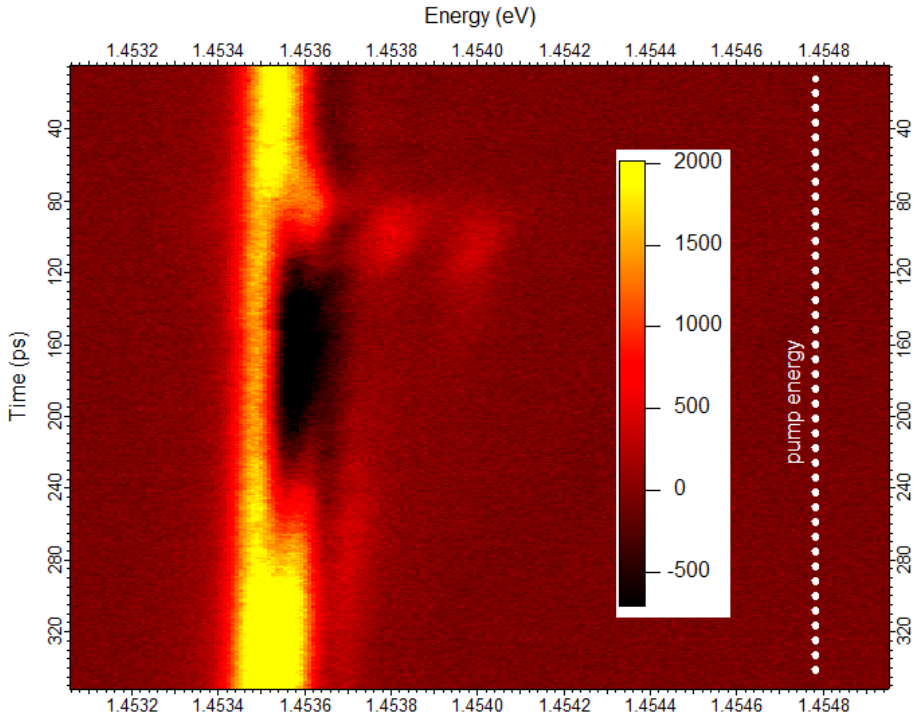

FIGURE 6.7: Temporally and spectrally resolved data taken using the setup described in section 5.5.1. The perturbation pulse arrives at $t = 80$ ps. Upon arrival the kick acts to blue shift the emission by 0.5 meV and significantly reduce its intensity. Some steady state emission remains, particularly at the low energy side. The long timescales are due to the use of non resonant perturbation, as described later in the chapter.

The blueshift of a state is dependent on the total number of particles in the entire system [64][62]:

$$\tilde{\epsilon_p} = X_n \left[X_i(N_i - N_{i0}) + X_s(N_s - N_{s0}) + X_p(N_p - N_{p0}) \right] \tag{6.19}$$

where X_n is the exciton fraction of the state in question.

Therefore, one effect of the transient introduction of extra polaritons into the pump state is to blueshift all of the states from their equilibrium steady state energy. We show this experimentally by spectrally and temporally resolving the signal emission during perturbation [3] (fig 6.7). When the kick arrives there is an instantaneous blue shift of >0.5 meV and the signal emission intensity drops significantly. Interestingly the low energy side of the signal emission is relatively unaffected. This can again be explained by spatial effects due to the Gaussian profile of the pump and kick.

[3]The increased timescale of this data compared to those seen previously in this chapter is due to a non-resonant perturbation scheme which is the subject of the latter part of this chapter.

A blueshift of the system has two effects, the first is a change in the resonance conditions between the three OPO states, and the second is a detuning introduced between the energy of the pump laser and the lower polariton branch.

6.3.1.1 Blueshift of OPO Resonance

The blueshift of a state is proportional to its excitonic fraction (eqn 6.19) and this is wave-vector dependent (eqn 2.10). Therefore the three OPO states blue shift by different amounts.

$$(X_s + X_i - 2X_p)\left[X_i(N_i - N_{i0}) + X_s(N_s - N_{s0}) + X_p(N_p - N_{p0})\right] \tag{6.20}$$

The term in the round brackets describes this blueshift-dependent detuning between the OPO states and is responsible for the switching off of the OPO at high powers, for our sample at zero detuning the value of this term is ~ 0.03.

The blueshift-induced detuning of the OPO states can be introduced into the model as a phase shift in the complex correlation term. Hence we relax our condition that c is purely imaginary and the full complex dynamics of the equations are tracked. The introduction of a phase shift means the system deviates from the phase-locked OPO condition (i.e. C real) upon blueshift from the equilibrium condition.

6.3.1.2 Blueshift of OPO Pump Coupling

The energy of the laser (ω_{cw}) is fixed during an experiment and its linewidth (κ) is narrow, as is that of the LPB ($\sim 0.5meV$). The coupling efficiency of the pump laser is dependent on the energy overlap of the pump with the LPB. The detuning between the laser and the LPB is defined as:

$$\Delta = \frac{\epsilon_p - \omega_{cw}}{\kappa/2} \tag{6.21}$$

Assuming that $\Delta = 0$ at equilibrium, any blueshift-induced detuning of the lower branch will reduce the pump coupling efficiency. This can be described by an overlap factor, o which acts on F_{cw}:

$$o = \frac{1}{1 + \Delta^2}. \tag{6.22}$$

As the pump coupling efficiency is dependent on the blueshift of a single state and not the difference in blueshift between three states as in the blueshift of the OPO resonance, it becomes a significant effect at much lower powers.

6.3.2 Comparison between Theory and Experiment

Figures 6.8 and 6.9 show how the model reacts when blueshift effects are introduced. In the first case the population of polaritons introduced into the model creates a small blueshift that changes the coupling of the pump laser, but is not great enough to shut off the OPO resonance. The timescale of the dynamics matches those seen experimentally. However, no reduction in the signal is seen. Hence we conclude that a blueshift of the pump coupling is not responsible for the dynamics.

In the second case a much larger blueshift occurs and both pump coupling and OPO resonance effects come into play. In this case a clear reduction in the signal state emission of the OPO can be achieved. The model also shows oscillations in the signal population during recovery with a period of a few picoseconds. This is below the resolution of our detector and so we would not be see them in our experimental data. The blueshift-induced detuning between the pump laser and LPB does not reduce the signal emission. This analysis shows that a blueshift-induced switching off of the OPO causes the transient reduction in signal intensity seen experimentally.

The dependence of the ratio of the dip depth to the steady state emission intensity on CW pump power is presented in figure 6.10 for both theory and experiment. In both cases the ratio is ~ 0.6 and is independent of pump power. This ratio depends on the size

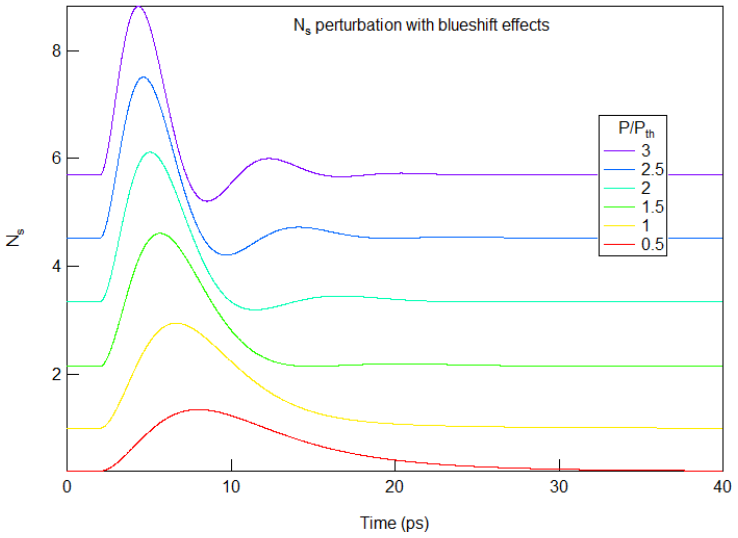

FIGURE 6.8: Theoretical model of the dependence of the temporal dynamics on CW pump intensity. Upon perturbation the blueshift acts to detune the LPB from the energy of the laser, effectively reducing the pump rate.

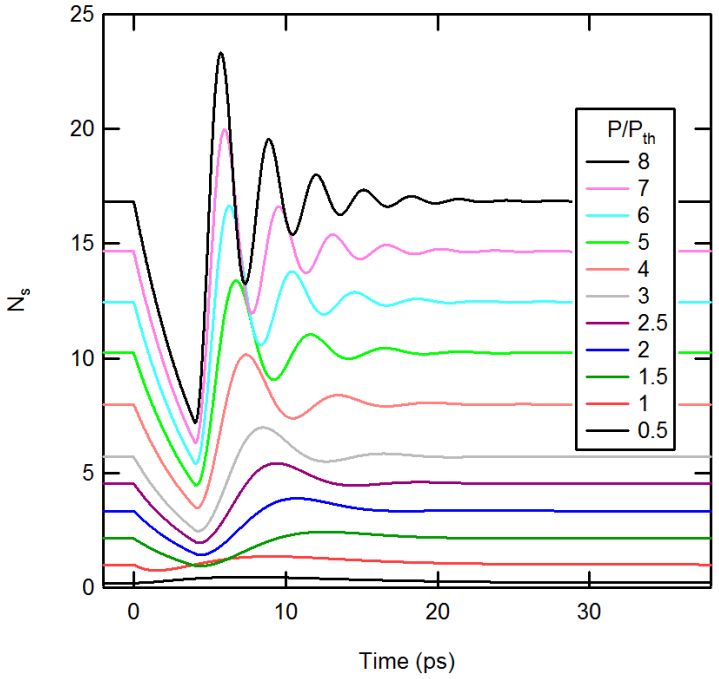

FIGURE 6.9: Theoretical model of the dependence of the temporal dynamics on CW pump intensity. Upon perturbation the blueshift acts to take the OPO out of resonance, effectively turning it off for a period of time.

of the kick induced blueshift. The agreement between experiment and theory confirms that sensible parameters are used in the model.

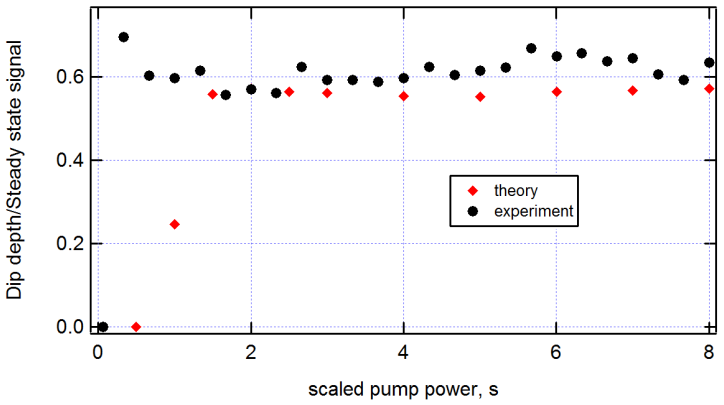

FIGURE 6.10: Theoretical (red) and experimental (black) ratio of the dip depth to the steady state emission intensity for different CW pump powers.

6.3.3 Weak Coupling

One possible argument to explain the dip is a transition from strong to weak coupling induced by the perturbing pulse. However, it is not thought that this is the case for the following reasons. First, the perturbing pulse is designed to introduce approximately as many polaritons into the pump state as are ordinarily there during steady state operation at twice threshold. This would not provide enough carriers to drive the system into weak coupling. Second, the OPO does not turn off completely during perturbation. Finally, the blueshift data of figure (6.7) clearly shows emission from the pump state during and immediately after perturbation. No emission was seen at the exciton or cavity mode, as would be expected if the system were driven into weak coupling.

6.3.4 Summary

In summary, a simple rate equation model, neglecting polariton self interaction, has been constructed to simulate the steady state operation of the OPO. Experiments have been performed that investigate the temporal dynamics of the signal state upon injection of surplus polaritons in the pump state. It was found that when the OPO is operating above threshold in the steady state regime, the effect of the perturbation was a transient reduction in the signal state population. The time scale of this dip is resolution limited ($< 10ps$) Blueshift effects had to be reintroduced to the theoretical model to fit the experimental data. It was found that the blueshift of the OPO resonance condition,

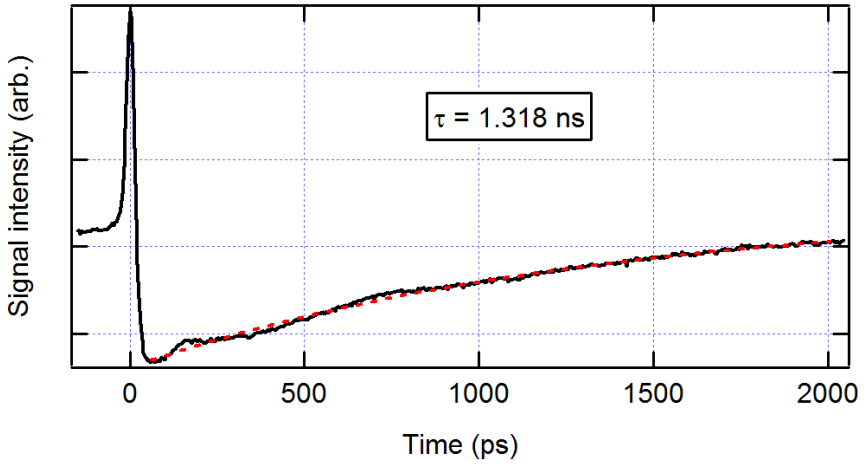

FIGURE 6.11: Experimental data showing the temporal dynamics of the OPO emission when the kick excites the exciton reservoir. A recovery time of 1.3 ns is measured, two orders of magnitude larger than that found under resonant excitation.

switching it off upon perturbation, was the important effect and replicated the data to a reasonable degree. Hence we have shown that the OPO signal emission can be transiently reduced by introducing surplus polaritons to the pump state. The time scale of the reduction is a few picoseconds, set by the polariton decay rate, κ.

6.4 Tuning OPO Dynamics Using Long-Lived States

In the previous section it was shown that emission from the OPO signal state could be reduced by an injection of polaritons into the pump state. This reduction was due to a blueshift of the lower polariton branch caused by the extra polaritons. Therefore the effect lasted only as long as the carriers in the system - a few ps. The blueshift acts through the exciton component of the polaritons. Stevenson [66] showed that it is possible to excite a reservoir of uncoupled excitons in the system. The excitons in this reservoir sit outside the light cone and are therefore dark. They have a lifetime of $\sim$1 ns and therefore we can to use them to extend the timescale of the dynamics seen in the previous section. In order to achieve this we tune the kick to be resonant with the exciton energy. A scattering process, either involving two virtual polaritons or a phonon populates the exciton reservoir.

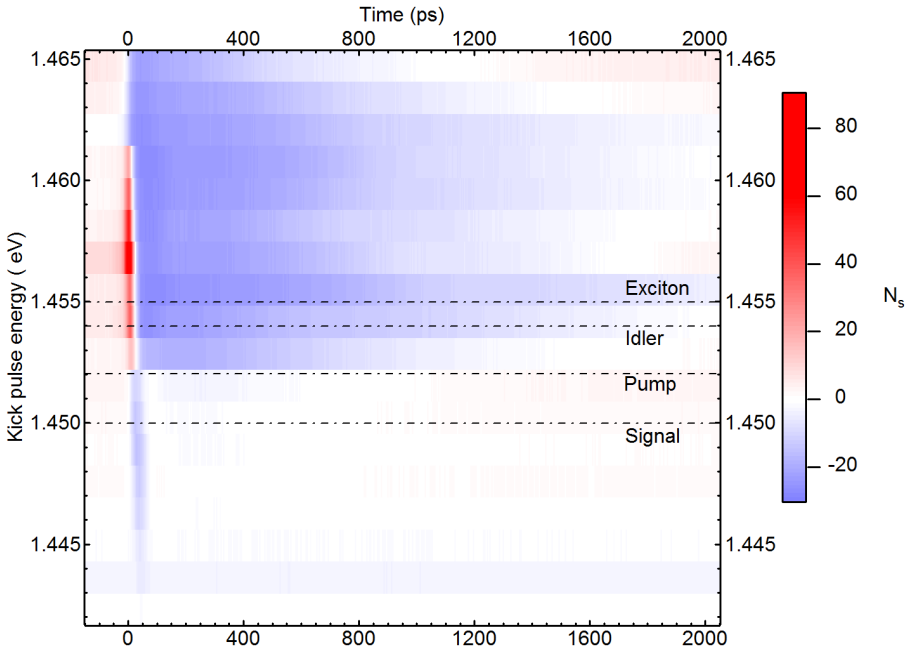

FIGURE 6.12: The energy of the kick pulse is tuned in 0.5meV increments from below the pump state, up to the UPB. When tuned to be at or below the LPB the dynamics have a timescale below the resolution limit of the detection system (10ps). However for higher kick energies the recovery dynamics have a timescale of up to 1ns. It is interesting to notice that at some energies there is a short peak in N_s as the pulse arrives.

Experimental data has been collated into an image (fig 6.12), to show how the dynamics of the system depends on perturbation energy, ω_k. For $\omega_k \leq \omega_p^0$ (again ω_p^0 is the energy of the LPB pump state in the steady state), the short-lived dip, investigated in the previous section, is evident. However, for $\omega_k \geq \omega_p^0$, the recovery timescales increase to as much as 500 ps 6.11. Again there is a reduction in N_s, but under non resonant excitation the recovery time grows to many hundreds of ps, rather than 5 ps as before. It was the excitation pulse length and polariton lifetime that determined the timescales in the resonant experiments, therefore the long timescales seen in these non-resonant experiments are a result of populating the much longer lived exciton states. Another interesting feature is the time-resolution-limited peak in emission that occurs before the dip at some energies. As is shown in the figure, this occurs for energies that are not resonant with any mode of the system, therefore it could be that this peak is just scatter of the perturbing pulse. In order to determine the nature of the interaction between these newly perturbed states and the OPO system the theoretical model will be adapted, as discussed in the next section

6.5 Modelling the interaction between the OPO and long-lived states

The kick pulse excites a reservoir of states, but in order to incorporate it into the model, it will be assumed that it actually only populates a single reservoir state. By giving this state its own lifetime and the ability to interact with the other states, it should provide a reasonable model of the reservoir of coupled excitons. This state, henceforth called the kick state, shall have the characteristics of an exciton, with a lifetime of ~ 1 ns. It shall contribute to the blueshift of the LPB. Scattering from the kick state to the other three states will be allowed, but a new coupling constant, D_k, will be used. D_k will be less than D as no parametric processes are available and therefore scattering will be via phonon interactions. The equations become:

$$\dot{N_s} = -\kappa N_s + 2DC + D_k N_s N_k \tag{6.23}$$

$$\dot{N_i} = -\kappa N_i + 2DC + D_k N_i N_k \tag{6.24}$$

$$\dot{N_p} = -\kappa N_p - 4DC + D_k N_p N_k + F_{cw} o \tag{6.25}$$

$$\dot{N_k} = -\kappa_k N_k - D_k N_k \left(N_s + N_i + N_p\right) + F_k(t) \tag{6.26}$$

where C is the correlation term defined in equation 6.13, N_k is the population of the kick state, κ_k is the kick state decay rate, and $F_k(t)$ the perturbing pulse.

Figure 6.13 shows the result of this model. At time $t = 200ps$ a kick pulse arrives and populates the kick state. The cw pump power, F_{cw} is set at $1.5P_{th}$ and the lifetime $1/\kappa_k$ to be 1ns. Calculations have been performed for different values of D_k. Without introducing any phase shift, the model shows a dip in N_s for all values of D_k. There is an inverse relationship between D_k and the recovery time and it can used to tune it

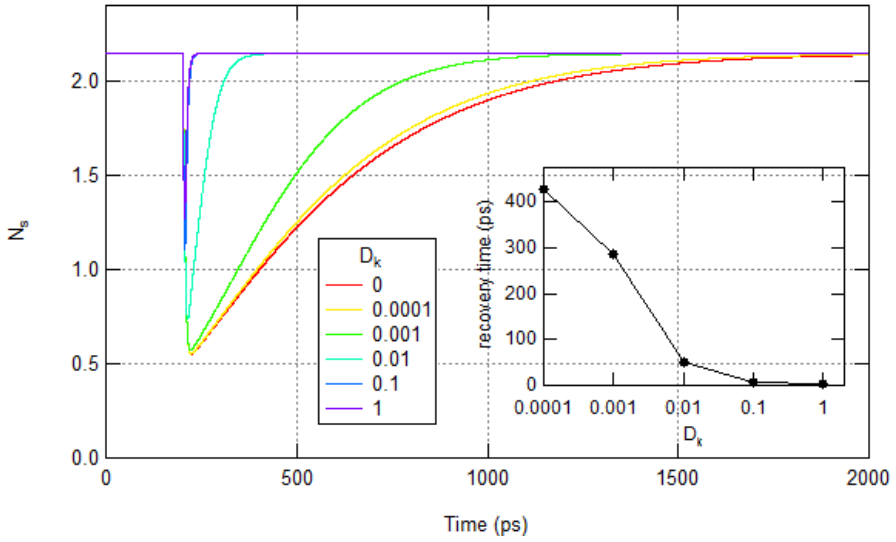

FIGURE 6.13: The recovery time of N_s is shown as a function of the coupling constant D_k. The decay time for the kick state is set to be 1ns. The inset shows how tuning D_k allows the recovery time of N_s to be tuned from 100s ps to 5 ps. Comparison to experimental data suggests that in this system $D_k < 0.001$.

from 5ps up towards 450ps. It was expected that D_k would be lower than $D = 0.02$, and the inset of figure 6.13 confirms that for the recovery time of the dip to be several hundreds of ps it should have a value of more than an order of magnitude below this. When the model is set to include a blueshift related phase shift of the OPO resonance the entire system shuts off and the signal state population drops to zero. Hence the long-lived dip appears to be primarily due to the overlap function controlling the pump coupling. Figure 6.14 shows the overlap function during resonant and non-resonant excitation. Under resonant excitation, the decay times of the polariton states mean that the overlap is only present for a few ps, after which the blueshift and therefore overlap recover to steady-state values and have limited effect. In the non-resonant case however, the blueshift is determined largely by the population of the kick state, which has a long lifetime in comparison to the OPO states. Therefore the overlap function significantly reduces the effective pump rate, which causes the dip in N_k.

The coupling efficiency of the kick into the system and therefore the absorbed kick power for the non-resonant experiment is much lower than in the resonant experiment. Hence fewer excitons are excited in comparison and the blueshift is smaller. In the previous section we showed that the pump coupling becomes important for much lower blueshifts than the OPO resonance effect. The coupling efficiency of the kick is dependent on

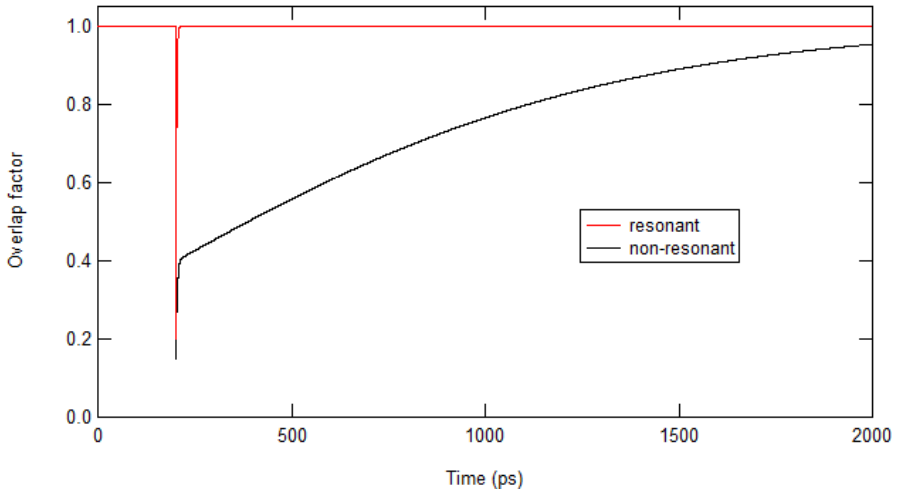

FIGURE 6.14: The overlap factor is compared between resonant (red) and non-resonant (black) excitation. The pulse and cw powers are the same in both situations. In the non-resonant case the recovery of the overlap factor is determined by the polariton lifetime. In the non-resonant case, the recovery is initially determined by the polariton lifetime, but then as the population of the three OPO states drops, the dominance switches to the kick state lifetime, set to be ~ 1 ns.

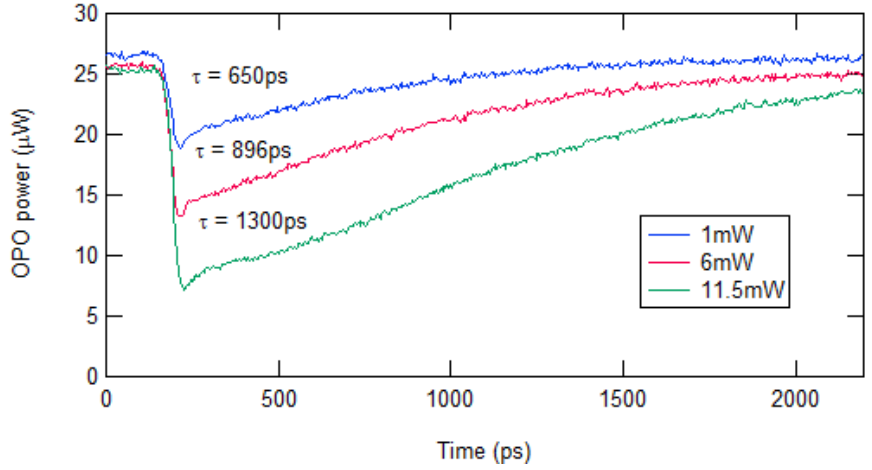

FIGURE 6.15: An experiment where the kick is set to be non-resonant and all parameters are kept constant except the kick power, F_{kick}. This shows that the dip depth and the recovery time depend on F_{kick}.

energy. Therefore the energy dependence of the recovery rate (fig 6.12) can be explained as a change in the kick injected polariton population. We performed a kick power dependence (Fig 6.15) and it shows that the recovery time is dependent on kick power, with increasing recovery times at higher powers. This would therefore suggest that we achieve optimum coupling to the exciton reservoir when we kick with an energy of 1.455 eV (from fig 6.12), which is the expected exciton energy in this system.

The data is modelled by changing F_k in equation 6.26 and the results are shown in figure

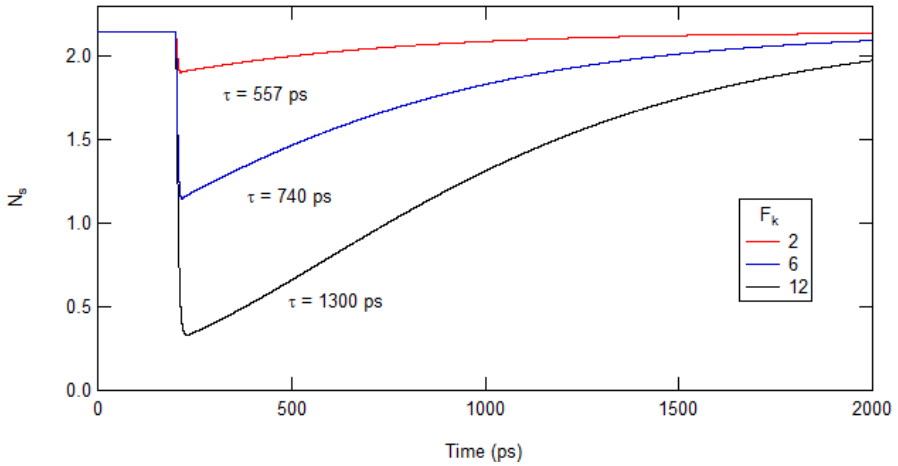

FIGURE 6.16: Traces demonstrating how the theoretical model can replicate the experimental data shown in the previous figure. Here everything is kept constant, except the power F_{kick} of the non-resonant perturbation. Although some of the recovery times vary slightly from the experimental data, the dip depth and recovery time are proportional to F_{kick}, as in the experiment. The shape of the recovery is also a good match.

6.16. The model matches the data to a good extent, with dip depth and recovery time dependent on kick power. This suggests that the variation in kick dynamics with kick energy can be explained in terms of a change in kicking efficiency with energy.

In summary, we can use the exciton reservoir to control the OPO dynamics on timescales of 100s ps via a blueshift changing the pump coupling efficiency.

6.6 Detuning Studies

Three further experiments were performed to support the hypothesis that the blueshift induced detuning between the pump laser energy and the LPB is responsible for the dynamics. First we control the detuning manually by fixing the pump and kick powers and performing a CW laser energy dependence. The experimental data (fig 6.17) shows that at low pump energies where the OPO is already detuned from its optimum position, the effect of the kick is to further increase the detuning, resulting in a decrease in overlap and hence efficiency of the pump laser, resulting in a decrease in signal intensity. However, for cw energies detuned above the LPB (energies above 1.454 eV as can be seen by the equilibrium signal level at times before the kick is incident) the extra blueshift

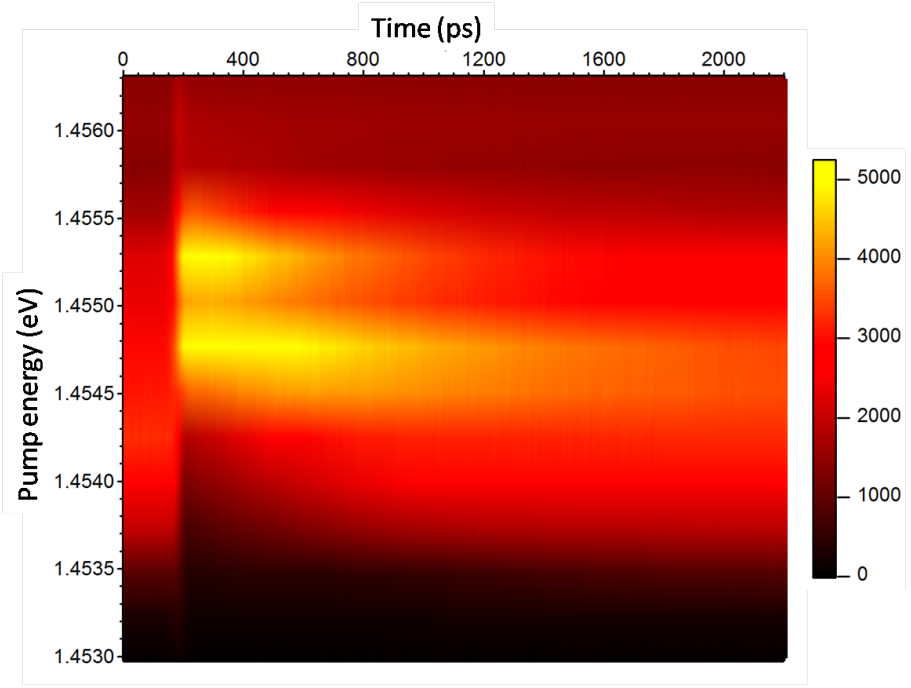

FIGURE 6.17: Experimental data showing the dependence of the OPO signal intensity non-resonant dynamics on CW pump energy. The kick arrives at t=150ps.

reduces the detuning the overlap is increased, resulting in an increase in signal emission. This proves that detuning and hence overlap determine the dynamics.

In the final two experiments we use the power of the CW pump to again control the detuning between the laser and the LPB. Firstly in fig 6.18 the CW laser energy is set to be resonant with the LPB at threshold. Therefore any kick-induced blueshift decreases the overlap and hence reduces the pump coupling efficiency, resulting in a decrease in the signal emission. This effect becomes more pronounced at high CW powers, where the steady state blueshift already creates a slight detuning. Figure 6.19 shows that the theoretical model does produce dynamics similar to those seen experimentally. The timescales are correct and the dip depth increases with CW power. However it is not clear why the experimental data shows a non exponential recovery. The shape of the recovery is more complex and can not be understood using our model. It is possible that the spatial effects described by Whittaker [67] are responsible.

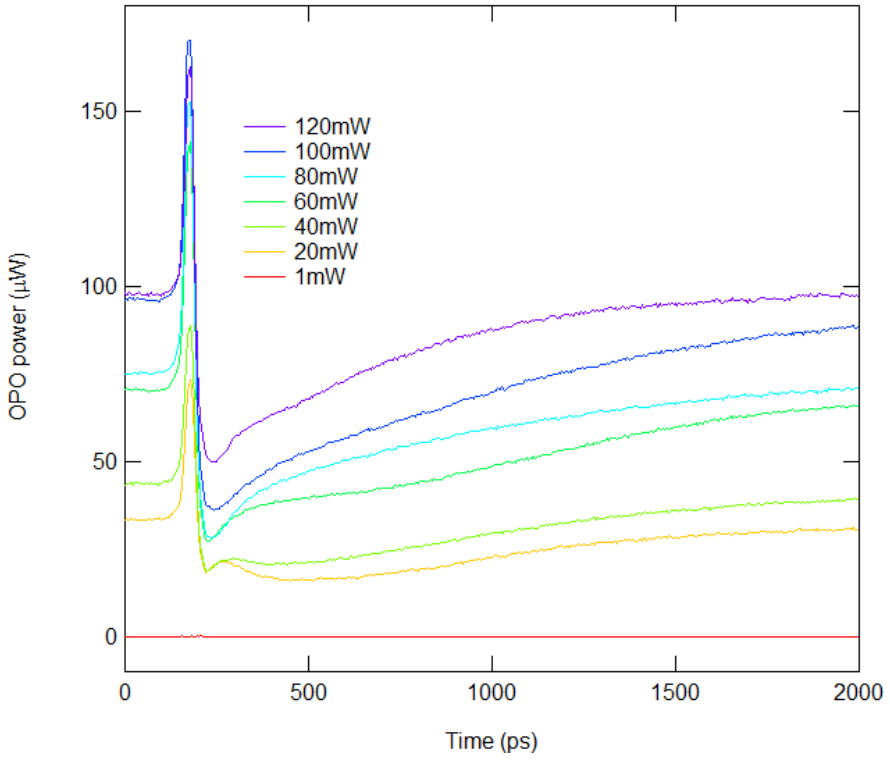

FIGURE 6.18: A non-resonant kick experiment, showing the dependence on cw power, F_{cw}. A temporary increase in N_s occurs before a long-lived dip becomes evident. The height of the peak and depth of the dip are proportional, whereas the recovery time is inversely proportional to F_{cw}. Notice the complicated recovery dynamics evident in some of the traces.

6.7 Summary

In this chapter we have measured the dynamics of an OPO that is perturbed from a steady state using a pulsed laser. It was found that for resonant perturbation of the pump state, the dynamics showed a reduction in signal intensity that recovered within a few picoseconds. Non-resonant perturbation resulted in dynamics with timescales of $\sim 1ns$, more than two orders of magnitude longer than the resonant case. This timescale was attributed to a kick-injected population of excitons.

A rate equation model was introduced which showed that the dynamics are caused by a perturbation-induced blueshift of the LPB. In the case of resonant excitation, the size of the blueshift was enough to bring the OPO out of resonance, shutting it off until the surplus polaritons had decayed from the system. However, in the case of non-resonant excitation the kick was able to excite far fewer carriers and, this resulted in a blueshift that was insufficient to take the OPO out of resonance, but did change the coupling of

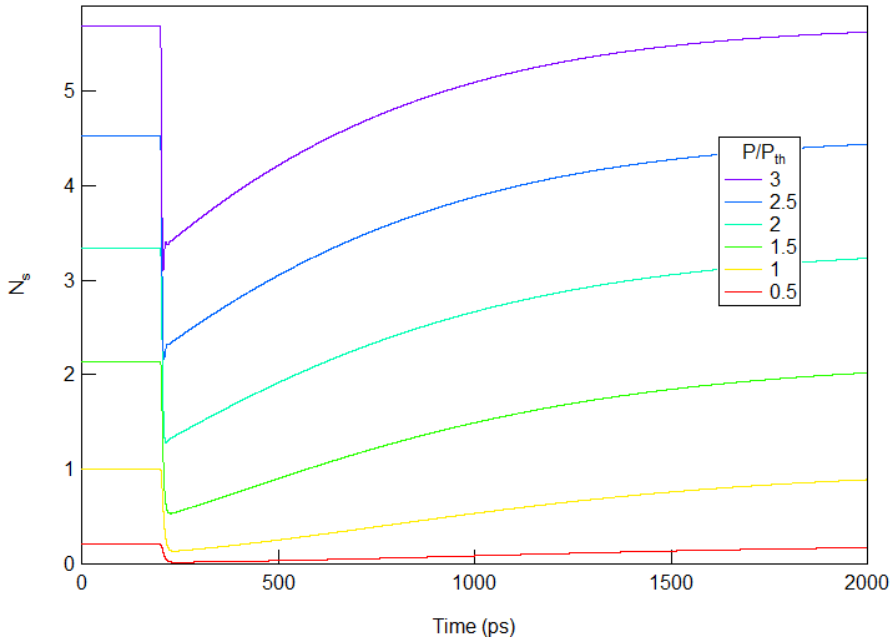

FIGURE 6.19: The theoretical model successfully replicates some of the important features of the experiment. In particular the dependence of dip depth and recovery time on cw power, F_{cw}. It does not however replicate the short peak, or complicate recovery dynamics seen in some of the experimental data.

the cw pump laser with the LPB. It was shown that by varying the detuning between the pump laser and the LPB the perturbation could be used to increase or decrease the OPO signal for hundreds of picoseconds.

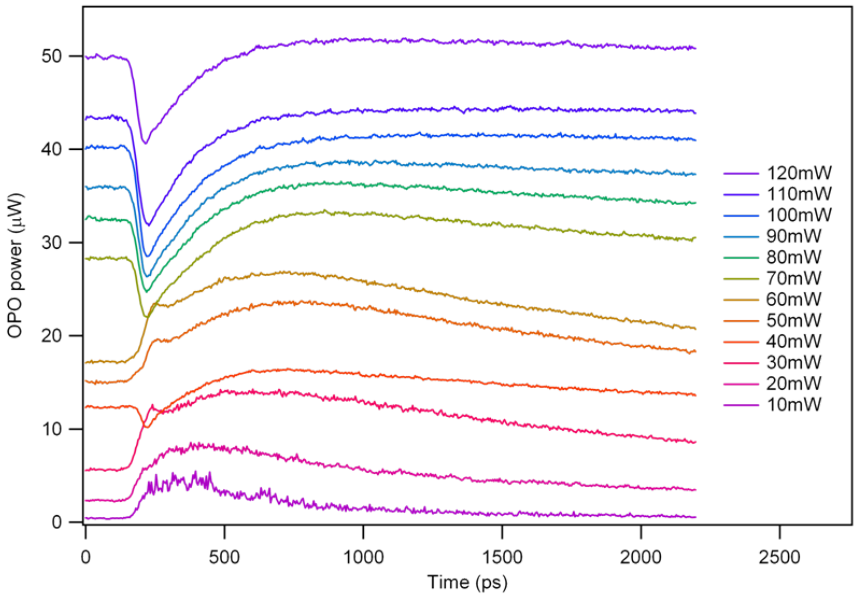

FIGURE 6.20: The overlap function responsible for the dip in non-resonant experiments can be used to produce a *peak* in N_s. The cw laser was tuned to be resonant when pumping at $s = 1.5$, rather than $s = 1$, the kick-induced blueshift tunes the pump state into resonance with the pump laser for $s < 1.5$. When $s > 1.5$, the blueshift once again shifts the pump out of resonance and a dip is created.

Chapter 7

Spatio-Temporal Dynamics of a Polariton Fluid

Exciton polaritons in microcavities are composite 2D weakly interacting bosons. The previous chapter showed that stimulated scattering allows a macroscopic population of the ground state, sometimes referred to as a polariton fluid [48]. If the polaritons reach some kind of thermal equilibrium then a Kosterlitz-Thouless transition is expected to occur (see chapter 3.4). Spatial disorder in real samples means that a phase transition to a Bose glass must occur before the superfluid transition is reached [68]. It is predicted theoretically that in this glass phase the polaritons accumulate spatially in areas where the potential landscape is at a minimum, and as the population builds the polariton states blueshift to level out the disorder[68]. At some polariton density all of the disorder is leveled out by blueshifts and the system enters its superfluid phase. This is characterised by a single emission energy across the entire emitting region, which is predicted to cover 50% of the excited sample area [68]. Recently, many research groups have started to investigate the spatial properties of microcavity poalritons. Exciting experimental reports have been announced claiming superfluidity of microcavity polaritons, proved via observation of the interaction of the polariton fluid with defects [69], and the observation of vortices [70]. However a detailed study of a sample similar to the one under investigation in this thesis by Sanvitto *et al* [71] showed that disorder prevents superfluidity even at very high pump powers. Although we can not observe

superfluidity in our sample, it has been shown both experimentally and theoretically that the microcavity OPO signal state exhibits some interesting spatial features [71].

One of the main simplifications of the theoretical model used to explain the results in the previous chapter was the plane wave approximation, ignoring the Gaussian profile of the pump beam. In this chapter the spatio properties of the dynamics of the perturbed OPO are investigated experimentally. Theoretical work by Whittaker [65] [67] has shown that stability of the OPO manifests itself in the spatial properties of the polariton fluid of the signal state. He shows that just above threshold the polaritons collapse to a small region in real space centered at the maximum of the Gaussian pump profile. This occurs because a threshold pump intensity must be reached before stimulated scattering becomes prevalent, hence this occurs at the center of the pump spot. However, as the pump power is increased, the central region of the Gaussian pump increases to such an extent that the OPO is taken out of resonance and switches off. However, for the same pump power a region in the wings of the Gaussian pump is brought into resonance, and OPO operation begins in this new spatial region (fig 7.1). This manifests itself as a ring structure of emission in real space. A detailed study by Sanvitto *et al* [71; 72] showed that in a sample similar to ours, this turning off of the OPO in its center does occur, however disorder in the system precludes formation of the ring structure.

The interesting dynamics shown in the previous chapter were explained in terms of the blueshift of the lower polariton branch. There were two effects: the first was a reduction in pump coupling efficiency and the second was a loss in the OPO resonance that turned off the OPO. However the model could not explain some of the more complex recovery dynamics and it was proposed that these could be due to spatial effects not described by the plane wave approximation. A theoretical model describing the OPO in real space is beyond the scope of this thesis, therefore the observations in this chapter are mainly qualitative and draw on the features explored in the previous chapter and in the theoretical work of Whittaker [65][67][62].

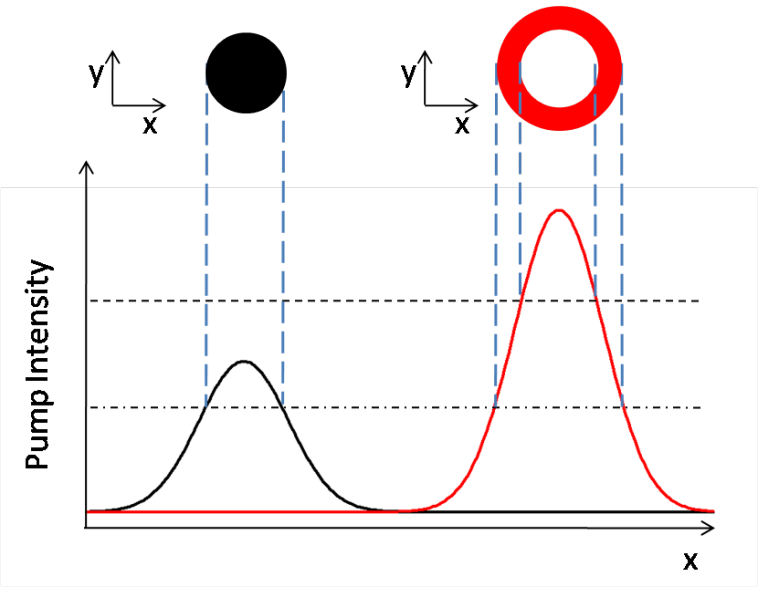

FIGURE 7.1: A schematic representation of the power dependence of the spatial features of the OPO signal state according to the theoretical model of Whittaker [67]. Two thresholds exist in the OPO (horizontal dashed lines). The pump intensity must be above the lower threshold and below the upper threshold for an OPO to operate. This, coupled with the Gaussian profile of the pump beam means that at high intensities the signal has a ring structure.

7.1 Spatial Overlap

The first investigation into the spatial properties of the polariton fluid will concentrate on the spatial overlap of the pump and kick beams. This experiment uses an imaging system to check the spatial overlap of the pump and kick pulse, but spatially integrates the normal incidence emission intensity.

We have found that the dynamics have some dependence on sample position. This is attributed to disorder. Therefore, in the following experiments every effort was made to repeat experiments on the same position of the sample. We choose 5 different overlap configurations. The spot size of the pump and kick beams are made to be the same. In one case the two spots are completely overlapped, in the other 4 cases the kick spot is shifted relative to the pump spot by one spot diameter in a given direction. The schematic on figure 7.6, shows a graphic representation of the overlaps and indicates the direction of travel of pump polaritons, determined by the angle of incidence of the pulsed laser. In the 'above', 'below' and 'right' overlap conditions the kick and pump spots do not overlap and the polaritons of the kick travel away from the pump. In these

conditions (green, red and blue traces in fig 7.6) the dynamics show a long lived increase in the OPO signal. This is because in the steady state regime the population density created in these regions means that the steady state blueshift is insufficient to bring the LPB into resonance with the pump laser. However, the pulse injects polaritons, which increases the blueshift LPB and decreases the detuning between it and the CW laser. The pump rate then becomes large enough to allow bring the system above the OPO threshold , this is referred to as a triggered OPO. The OPO now covers a greater area of real space and hence the signal emission increases. It is interesting to note that the triggered OPO lasts for much longer than the polariton lifetime.

In the cases where the beams are overlapped we see more complicated dynamics. First a decrease, followed later by an increase in the spatially integrated signal emission above the steady state level. The dip is more pronounced in the fully overlapped case (black). In the situation where the polaritons are injected spatially away from the pump spot and then move towards and collide with it (pink) clear oscillations are present in the intensity of the signal as it recovers. It was initially thought that these oscillations were an important part of the recovery dynamics, however they were later found to be an artifact [1]. All of these dynamics can be explained using the blueshift-dependent overlap function described in section 6.6

In summary, we have shown that the spatial overlap of the pump and kick beams play an important role in the spatially integrated OPO dynamics. The dynamics can be explained qualitatively using the blueshift-dependent overlap function described in the previous chapter.

7.2 Spatio-Temporal Measurements

To explore the dynamics occurring within the polariton fluid an experiment was performed with spatial as well as temporal resolution. The experimental setup is detailed in section 5.5.2. An image of the real space emission of the microcavity is projected onto

[1] It was found that when exciting with a pulsed laser with an energy 43 meV below the LPB, temporal oscillations were present in transmission/reflection with the same period as the data in fig 7.6. These are attributed to reflections from the back and front surface of the sample (including the substrate). With refractive index taken into account these oscillations suggest a feasible sample thickness of $\sim$500 μm.

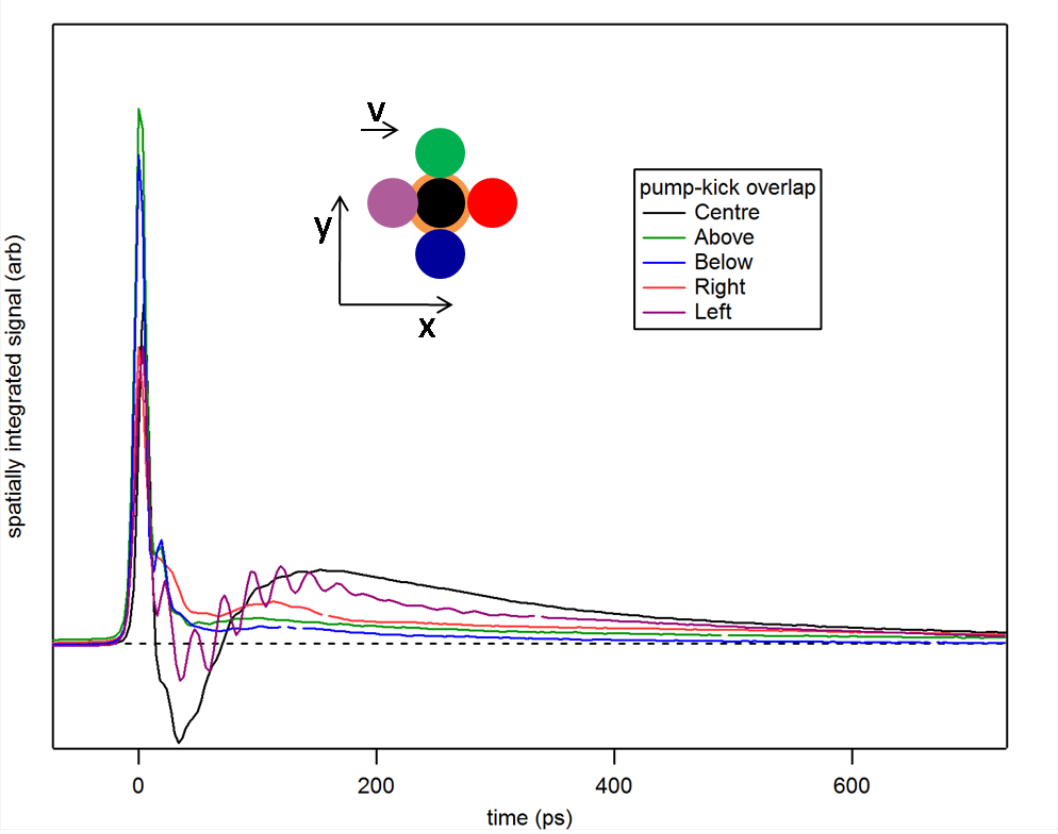

FIGURE 7.2: Spatially integrated data showing the effect of pump-kick overlap on the dynamics of the signal state. The schematic shows the overlap of the kick (coloured) with the pump (orange) in each of the five experiments. The direction of travel of polaritons is towards the right, indicated by the arrow.

the input slit of a streak camera using a combination of lenses. A slit at the entrance to the streak camera allows a thin slice of the image to enter. It can then provide temporal information on that slice, with one dimension of the resulting image being time and the other real space. In order to build up a complete two dimensional image, a piezo controlled mirror moves the image across the streak input slit in small steps, recording a spatio-temporal image at each position. This images are then collated in a 3D matrix, effectively storing a movie of the polariton dynamics. The magnification of the system allowed a 100 μm area of the sample to be studied. The streak camera has a temporal resolution of up to 5ps. We first present results on a simple single-beam experiment, used to test the imaging system by measuring the velocity of injected polaritons. Then we look at the full spatio-temporal dynamics of the pump-kick experiment.

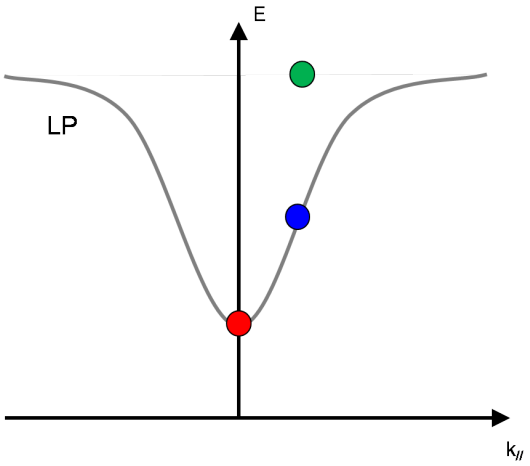

FIGURE 7.3: A schematic of the lower polariton branch showing the states excited in the single beam experiment of section 7.3.

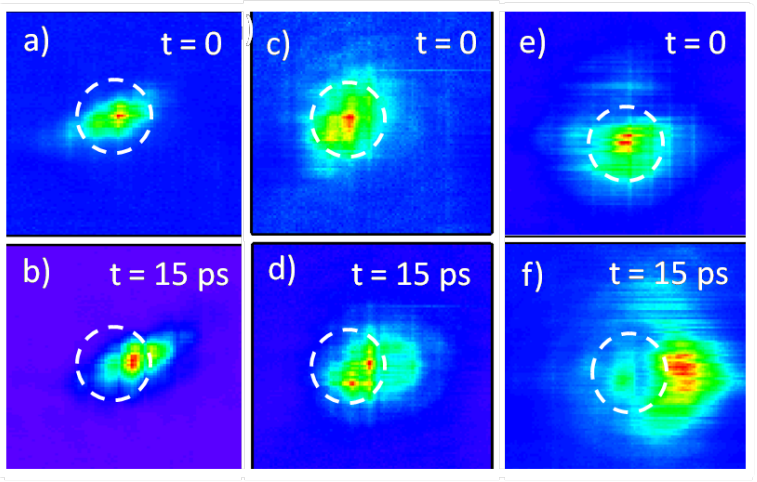

FIGURE 7.4: Real space images of the signal state emission, with sides 100 micron. The top images are upon excitation with a pulse, the bottom after 15ps. Panels a) and b) are under normal incidence excitation resonant with the LPB, panels c) and d) are under resonant excitation at 16 degrees and panels e) and f) are at 16 degrees but slightly non-resonant (close to the bare exciton energy).

7.3 Measuring Polariton Velocity

In order to test the spatio-temporal detection system a single beam experiment was devised where a pulsed laser beam is used to inject polaritons into the system in three different scenarios (fig. 7.3). No energy filtering of the emission is performed, therefore a significant amount of scatter is detected when the pulse arrives at time t=0, allowing determination of the position of the excitation in real space. Polariton emission from the k=0 state is temporally and spatially resolved, tracking the 2D real space emission in time.

Figure 7.4 shows two slices from the 3D data set, for each of the three excitation scenarios, showing the real space emission pattern at times t=0 and t=15 ps. When exciting at normal incidence, where the polariton has zero in-plane momentum, the polaritons move a very small amount in real space (fig 7.4(a,b)). However, in both of the experiments with 16 degrees excitation (equivalent to $\sim 0.5\mu m^{-1}$ (fig 7.4(c-f)), where the polariton states have some in-plane momentum, the emission center moves significantly. This movement of the emission center has been extracted from the data and is presented in figure 7.5. Careful calibration of the image magnification allows a velocity to be calculated; in the case of resonant excitation the polaritons move with a speed of $\sim 0.5\text{x}10^6$ ms^{-1}, and for non-resonant excitation it is approximately twice this value. Hence, the polaritons travel at $\sim$ 1% of the speed of light, similar velocities have recently been reported elsewhere [69]. In the case of nonresonant excitation the pulse will excite a variety states on the lower polariton branch, these states will have different effective masses and in-plane momentum and hence different speeds. This explains the difference in the velocity between the resonant and nonresonant experiments. The spreading of the pulse spot under non-resonant excitation also suggest that a number of states with varying velocities are excited. In the case of resonant excitation the spot size remains almost fixed in time, suggesting that all polaritons have the same velocity and therefore come from the same state.

7.3.1 Summary

In summary, the spatio-temporal detection system was used to measure the movement of polaritons with in-plane momentum $\sim$0.5 μm^{-1}, injected by a short pulse. Their velocity was calculated to be $\sim$ 0.5% the speed of light, comparable with measurements reported elsewhere [69]. We suggest that in that under non-resonant excitation a range of polariton states are excited.

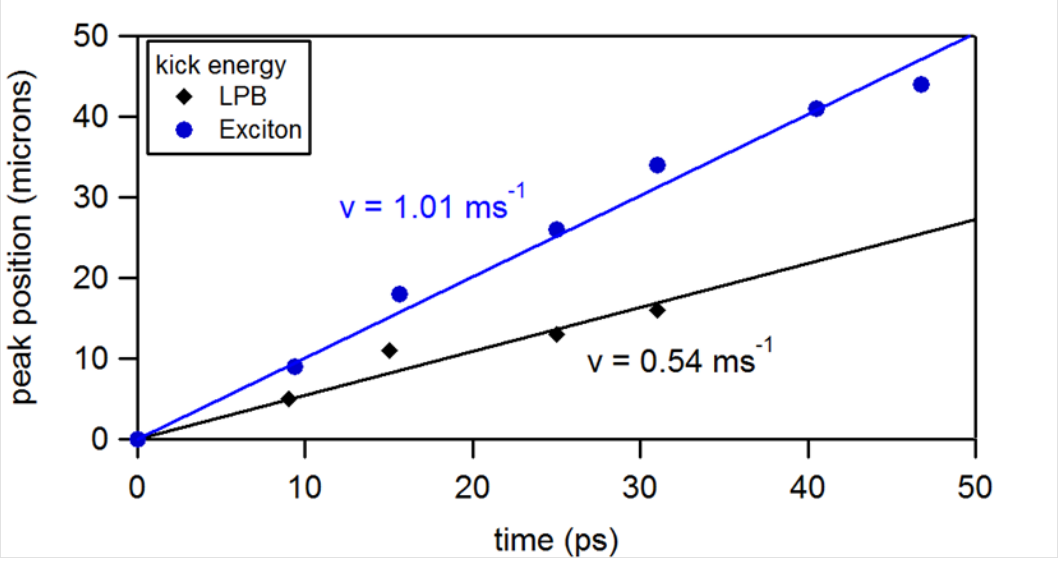

FIGURE 7.5: Temporally resolved real space images have been used to track the motion of polaritons. A pulse is used to excite create the polaritons at 16 degrees, both resonantly (black) and non-resonantly (blue) with the LPB. Speeds close to 1% speed of light are realise in the nonresonant case.

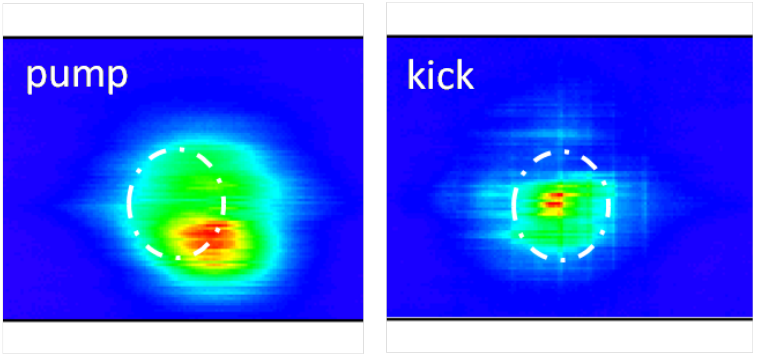

FIGURE 7.6: Real space images of signal state emission under cw pump (left) and pulsed kick (right). A white circle is used to give a reference between the images.

7.4 Two Beam Spatio-Temporal Dynamics

An experiment is now reported where the spatio-temporal dynamics of the pump-kick experiment is studied. In order to do this we choose an overlap between the pump and kick beams that is slightly off center, such that we get the most interesting spatially integrated dynamics 7.1. The power and energy of the CW pump are also fixed such that there is minimal detuning between the pump laser and the LPB. This pump-kick experiment was performed as described in section 5.5.2.

Figure 7.7 is split into two sections, the bottom panel shows the spatially integrated dynamics for comparison with the overlap data discussed in the previous section. The top

9 panels show real space images of the signal emission at different times after perturbation. To make the effects clearer to see, the steady state OPO emission profile has been subtracted from the images. Regions of space which experience an increase (decrease) in OPO emission are coloured red (blue). Areas unaffected by the pulse appear white. At time t=0 almost the entire real space image shows an increase in signal. This is thought to be due to scatter of the kick pulse as well as rapid relaxation of kick-injected polaritons to the ground state 7.3. At later times, in some areas of the image there is a reduction in OPO emission (blue areas), but at no time does this happen in every region of the polariton fluid. This shows that the temporal dynamics vary within the polariton fluid.

This is highlighted again in figure 7.8 which shows a slice through space, where the horizontal axis is real space in the x direction and the vertical axis is time (increasing downwards). This slice is taken at the y position where the kick pulse is maximum at time t=0. It is clear that the depth of the dip and its lifetime depend on the pump-kick overlap. In general, areas with lower concentrations recover from the dip more quickly. Towards the wings of the Gaussian profile of the kick an increase in signal emission is seen after recovery from the dip. Such features can again be explained using the theory developed in the previous chapter, where the OPO signal dynamics are determined by the blueshift-dependent coupling between the pump laser and the LPB.

7.5 Summary

Several common features can be extracted from these spatial studies. Qualitatively, the theory developed in Chapter 6 describes the dynamics. However, a full two-dimensional model would have to be constructed to prove this. Firstly, it is clear that the OPO dynamics depend on spatial distribution of polariton population. Second, because the spatial distribution of polaritons depends on the intensity profile of the pump and kick states, by changing their spatial overlap all sorts of dynamics can be achieved in the spatially integrated data - from an increase, to a decrease, to something that switches between the two. Third, by spatially resolving the intensity we have shown that the

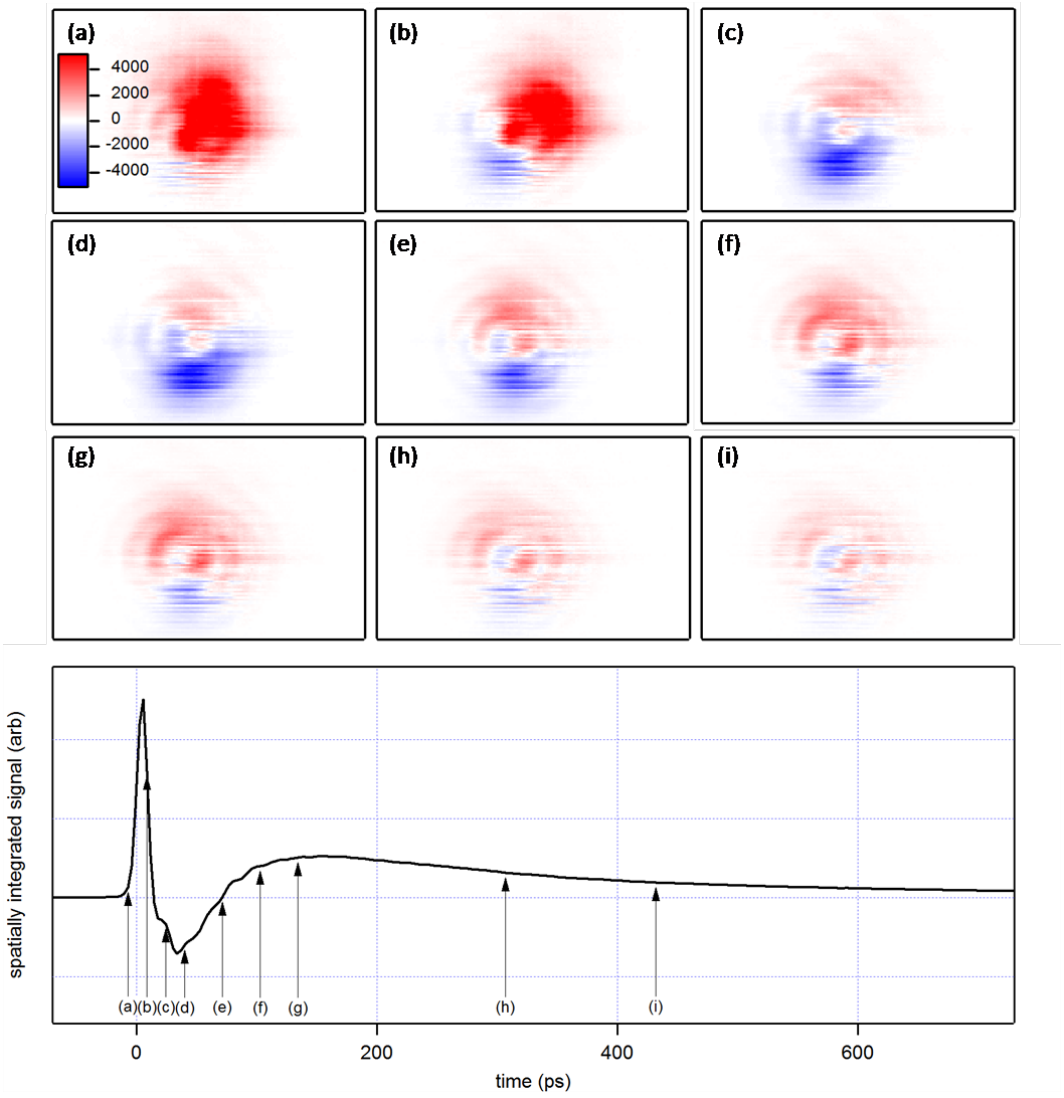

FIGURE 7.7: Spatio-temporal dynamics of a pump kick experiment. The lower panel indicates the time-resolved spatially-integrated emission. Arrows mark the times at which images are displayed (labelled a-i). Red (blue) indicates an increase (decrease) compared to the steady state emission.

polariton fluid does not act as a single entity upon perturbation, many different dynamics occur within the polariton fluid.

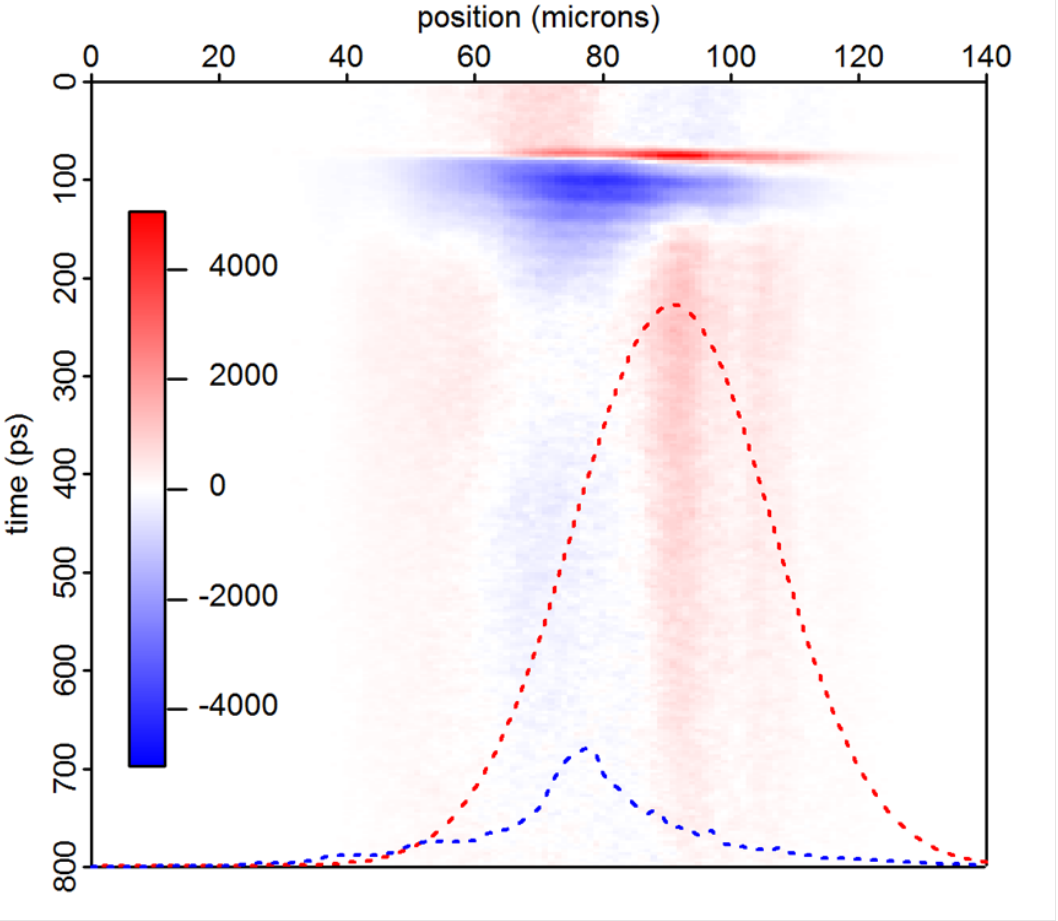

FIGURE 7.8: A time-resolved slice through the real space image during a pump-kick experiment. Red (blue) indicates an increase (decrease) compared to the steady state emission. The time dynamics are different at every point in real space, indicating that overlap and sample disorder are important factors in dynamics. The profile of the steady state(pulsed) emission has been overlayed in red (blue) dashed lines for comparison.

Chapter 8

Room Temperature Polariton Lasing and BEC

In this chapter experimental data is presented that demonstrates the operation of the first room temperature polariton laser. Polariton lasing is the result of bosonic stimulated *scattering* to a macroscopically occupied state which results in inversionless coherent emission, or polariton lasing. This is in stark contrast to the stimulated *emission* of a conventional laser requiring population inversion. Further to this, the emitted polariton laser light exhibits spontaneous symmetry breaking of the polarisation, suggesting the presence of the first room temperature Bose-Einstein condensate (BEC). This work was carried out on the GaN-based sample detailed in section 4.2, whose large oscillator strength and exciton binding energy allows strong coupling at room temperature with a Rabi splittings of 36 meV [50]. The results presented in this chapter were collected in collaboration with Stavros Christopoulos and Giorgio Baldassarri.

8.1 Large Area Reflectivity

A Jasco UV-Vis spectrometer is used in reflection mode to measure the near normal incidence reflectivity of the top dielectric mirror, figure 8.1. It clearly shows the high

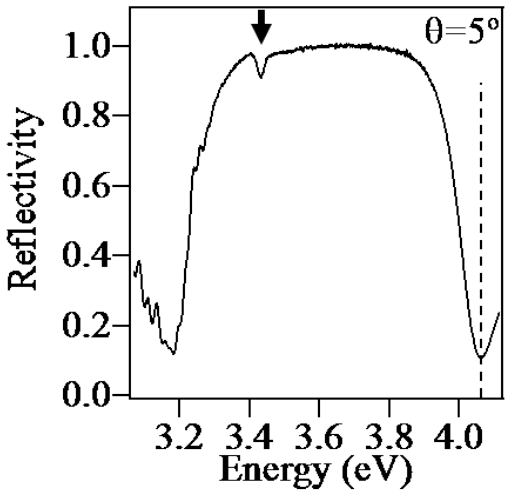

FIGURE 8.1: Microcavity reflectivity at room temperature at near normal incidence. The arrow indicates the polariton mode and the dashed line shows the position of the nonresonant pump laser energy. This data was taken with a Jasco UV-vis spectrometer.

reflectivity stop band of the DBR along with the lower polariton mode at 3.4 eV, indicated by the black arrow. The full dielectric constants of GaN at 3.4 eV [73], both with and without the excitonic resonance, have been used in a transfer matrix calculation giving the dispersion and absorption of the microcavity, Figure 8.2. The effect of strong coupling manifests itself in the relatively flat lower polariton branch, however the upper polariton is broadened and almost completely attenuated by the exciton continuum. The hybrid nature of the microcavity mirrors means that top dielectric and bottom GaN DBRs have different average refractive indices. This leads to different in-plane dispersions and hence increased detuning with angle. Also, Bragg modes from the GaN-based DBR stop band cross the dispersion [74].

The photoluminescence setup described in section 5.3 is used to investigate the emission under non-resonant pumping. Pulses of **1**50 fs duration are focussed down to a 60 μm diameter spot on the top DBR and the resulting luminescence is collected in a particular emission direction over an angular range of $\pm 3^o$, and focused onto a UV multimode collection fibre coupled to a 0.5m monochromator and liquid N_2-cooled CCD.

Pumping efficiency is maximized by tuning the pump energy to be resonant with the first Bragg mode, indicated by a dashed line in figure 8.1. The sample is not wedged, and exhibits a detuning of -10 meV, however some tuning of the cavity mode around the

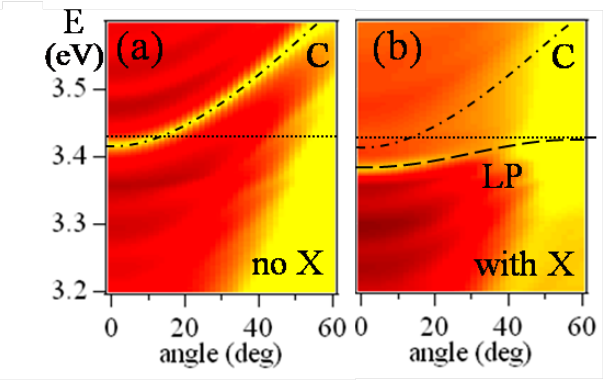

FIGURE 8.2: Theoretical angular dispersion both without (a) and with (b) the resonant exciton contribution to the GaN cavity(ω_{LP} dashed line, ω_{cav} dash-dotted line) for a slightly negatively detuned cavity (Δ = -10 meV). As published in [75]

exciton energy, $\Delta = \omega_c - \omega_x$, due to photonic disorder is achieved by scanning around the sample. PL spectra at low power (<10 W cm^{-2}) are recorded as a function of angle for a fixed spot on the sample, figure 8.3, and are characteristic of results seen over a large area of the sample. The lower polariton (black dashed line) is clearly visible increasing towards the exciton from below. As predicted by the theory the upper polariton PL is very weak and Bragg modes from the lower DBR also strongly couple to the GaN exciton, leading to additional anticrossings at high angles (red dashed line) [74]. This data shows that the microcavity exhibits strong coupling at room temperature. Similar strong-coupling bulk GaN microcavity dispersions have been previously reported [58][76].

8.2 Power Dependent Characteristics

Figure 8.4 shows the temporally integrated output intensity collected at normal incidence when the sample is again pumped nonresonantly at the first Bragg mode. A clear nonlinear behaviour is found for the emission at $\lambda \simeq 365$ nm, with an increase of over 10^3 at the critical threshold around $I_{th} = 1.0$ mW. The carrier density, N_{3D}, is given by:

$$N_{3D} = \frac{(1-R)AI_p}{(f_p \hbar \omega \pi r^2 L)} \tag{8.1}$$

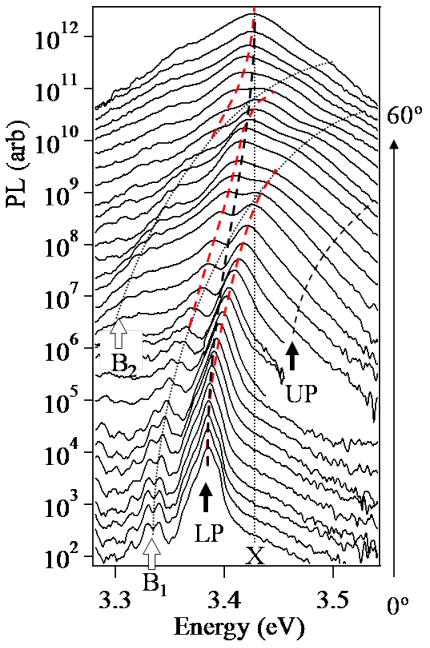

FIGURE 8.3: Angle-resolved PL at low powers up to 60^o, with Lower (LP) and upper (UP) polaritons, exciton (X), and Bragg modes (B) marked. This particular set of data was recorded by Stavros Christopoulos as published in [75].

where R is the reflectivity of the top mirror, A is the absorption of the bulk GaN, I_p is the time averaged pump intensity, f_p is the pump repetition rate, r the spot radius and L the cavity length. R was measured to be 30%. Therefore if it is assumed that A is also 30%[1] $N_{3D} \sim 2.2$ x $10^{18} cm^{-3}$. The Mott density in GaN at room temperature is given in the literature as $\simeq 1 - 2$ x $10^{19} cm^{-3}$ [77][78]. This is also the value of the transparency density, a lower limit for photon lasing. Therefore, as the threshold density of this system is an order of magnitude below the transparrency density, photon lasing cannot be occuring, which therefore implies the operation of a polariton laser. Figure 8.5 shows a photograph of the polariton laser operating above threshold.

These features are similar to the low temperature polariton lasing reported in II-VI and III-V microcavities at low temperature [1][2][74][60]. A simple model can been used to fit the integrated output intensity [79]:

$$I_{out} \propto r - 1 + \sqrt{(r-1)^2 + \frac{4r}{p}} \tag{8.2}$$

[1]the substrate used to grow the microcavity is absorbing a the pump wavelength and therefore a direct measurement could not be made.

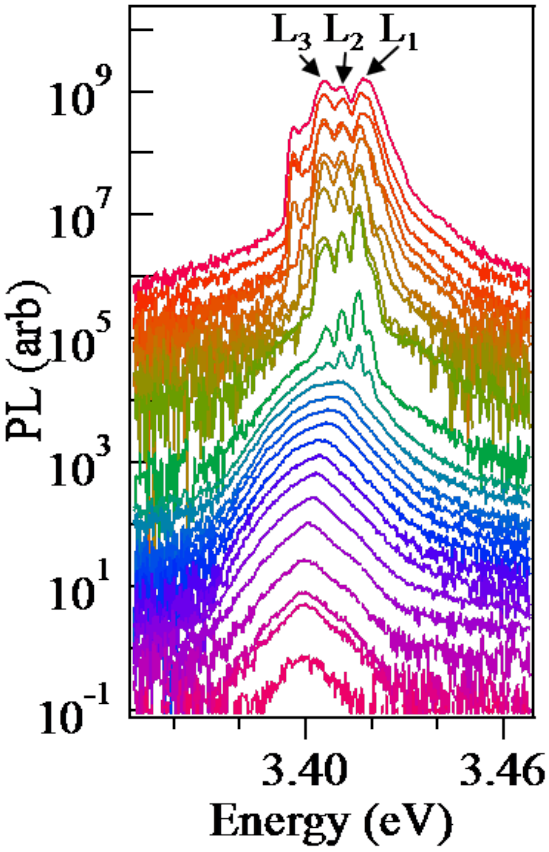

FIGURE 8.4: Emission spectra at pump powers from 20 μW to 2 mW at 0^o shifted for clarity.

where r is the pump rate normalized to threshold and p is the number of modes into which polaritons can spontaneously decay. A fit to the integrated intensity is shown in figure 8.6 (a), using $p = 7000$. $\beta = 1/p$ is the probability that the spontaneously emitted polaritons emerge in the mode which undergoes stimulated scattering [80][81][11].

The polariton laser threshold is defined as the point at which the occupation in any polariton mode reaches unity. This causes stimulated scattering of polaritons into that state, due to their bosonic nature, resulting in inversionless coherent emission, or polariton lasing. For a pump power of 4 mW, the emitted power is measured to be 80μW. The number of polaritons per state per pulse above threshold is given by the relationship:

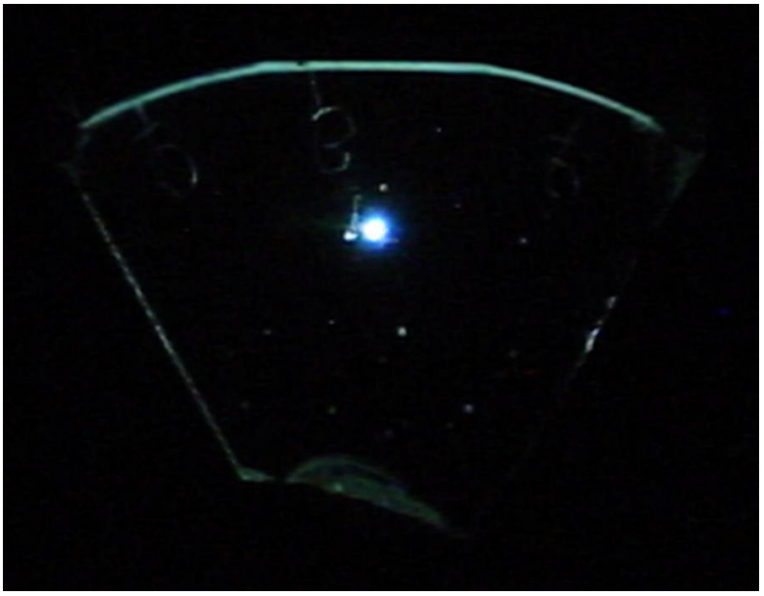

FIGURE 8.5: Photograph of the polariton laser operating above threshold.

$$N_{state} = \frac{I_{out}}{f_p \hbar \omega p} \tag{8.3}$$

where p is as defined in equation 8.2. In our system this is found to be $\sim 10^5$ polaritons/state/pulse above threshold Therefore at threshold occupations are estimated to be $\geq$10. In reality, the occupation must be 1 at threshold, the discrepency is likely to be due to uncertainty in the number of modes above threshold.

At the threshold of the exponential power increase, there is a simultaneous collapse in emission linewidth down to the resolution limit of the detector (1.7 meV) (fig. 8.6). Spectra integrated over 10ms often show multiple line emission, for example emission lines L_{1-3} in 8.6 (c). The energy spacing between the sharp emssion peaks is dependent on sample position and is often irregular. It is thought that the photonic disorder localizes the polariton condensate laterally (similar to CdTe microcavities [74][60]), with the different modes first attaining unity occupation on different laser shots statistically. This is discussed further in section 8.4.

As in the GaAs system discussed in chapter 6, as the pump power increases the peak emission energy *blueshifts* until it locks at threshold, figure 8.6 (c). This is due to

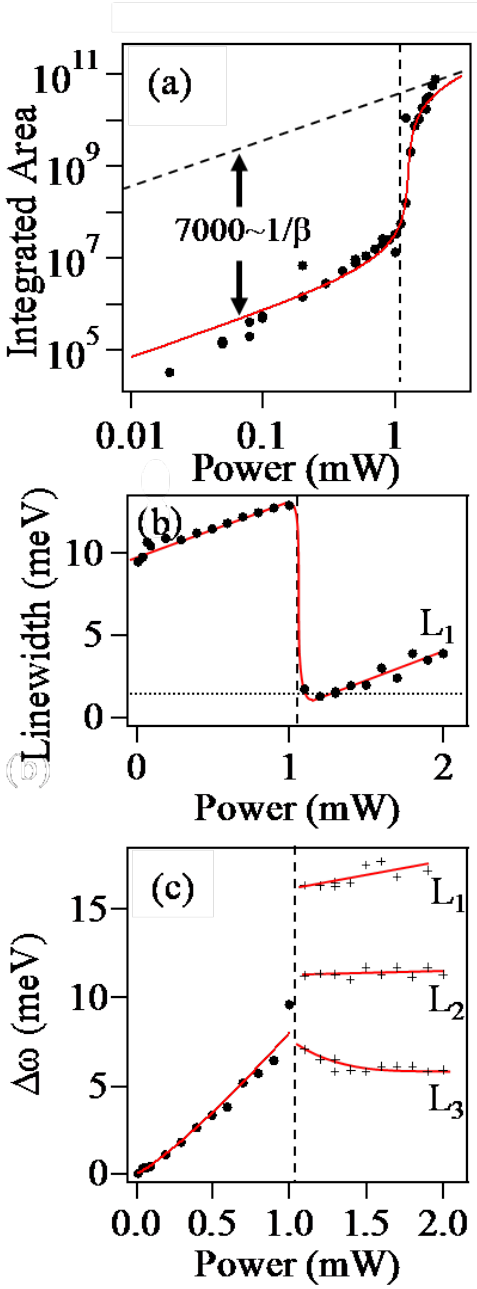

FIGURE 8.6: (a) Integrated intensity vs pump power (solid points), with fit. (b) spectral linewidth and (c) energy shift of peak emission with pump power (for different modes L_{1-3}).

polariton-polariton interactions [82]. The blueshift at threshold is related to the exciton density:

$$\hbar\Delta\omega_{LP} = \frac{1}{2}\hbar\Delta\omega_X \sim 3.3\pi E_b a_B^3 N_{3D} \tag{8.4}$$

where $E_b = 28$ meV is the exciton binding energy, $a_B = 3.5$ nm is the Bohr radius, and

N_{3D} is the exciton density. From this relation $N_{3D} \sim 8$ x $10^{17} cm^{-3}$ at threshold, which compares favourably to the estimate using equation 8.1, confirming sub-Mott density coherent emission. The blueshifted emission remains below the exciton energy, further supporting the existence of strong coupling at threshold. By contrast, incoherent GaN emission is known to *redshift* with increasing pump power [77][78], while thermal cavity expansion would have a similar effect.

8.3 Time-Resolved Photoluminescence

The rise and decay time of the normal incidence emission at and around threshold is recorded using a streak camera with 4ps time resolution (fig 8.7). In all cases there is a resolution limited rise time suggesting that even at low carrier densities, scattering and thermalization occur on sub picosecond timescales. At low powers there is an exponential decay of 30 ps, this can be attributed to trapping of excitons at non-radiative defects [83]. As the power is increased to threshold, an additional fast component rapidly rises (8.7, dashed fits show slow decay, inset shows relative amplitudes), with a decay time of 8 ps. Above threshold, the coherent emission turns on and off in <2 ps, implying that scattering from the exciton reservoir is extremely fast. The efficiency of emission increases as stimulated scattering into the lower polariton (which emits within a few ps) becomes fast in comparison to the nonradiative rates.

8.4 Real Space Disrbutions

The real space polariton distribution is measured as a function of power using the experimental setup described in section 5.3.1. Figure 8.8 (a) shows the below threshold emission with the pump illumination area indicated by a dashed line. At these low powers the spatial emission clearly follows the pump spot. Above threshold, figure 8.8 (b), the real space emission spot reduces in size to $\sim 5\mu$m. This size varies slightly with position. In some positions multiple emission centres are recorded, figure 8.8 (c). Again, it is assumed that only a single emission spot occurs for each excitation pulse,

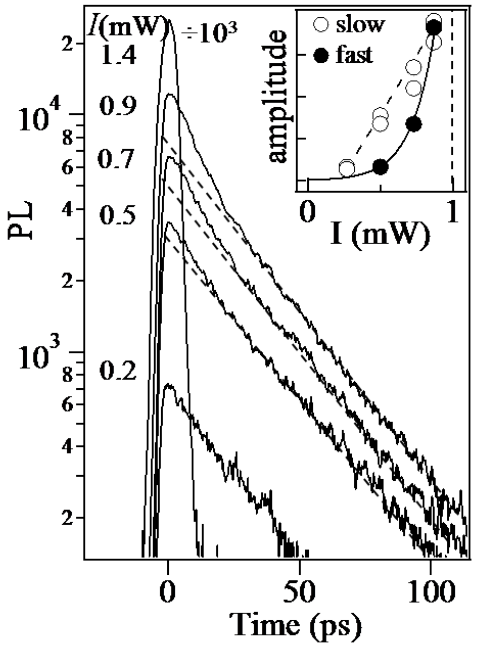

FIGURE 8.7: Time-resolved emission at normal incidence vs pump power from 0.2 mW to 1.4 mW, with amplitudes of fast and slow components extracted (inset).

however if multiple regions within the pump spot are capable of lasing then they will occur statistically in repeated measurements. A 5 μm spot size above threshold implies that only $\sim 1\%$ of the pumped spot is involved in the strong emission, thus suggesting efficiencies within this small area close to 100%.

A micro photoluminscence map, recorded by Gabriel Christman of EPFL, is shown in figure 8.8 (d). This maps the q-factor and therefore photonic disorder using a spot size of $\sim$8 μm.. Regions of high q-factor with a size of $\sim$5 μm are clearly present and therefore it is likely that it is this photonic disorder that determines the emission spot size and accounts for the multiple emmision centres.

Such a spatial localization will produce transverse modes with the following spacing:

$$\frac{\Delta\omega}{\omega} \simeq \frac{3(\lambda_0/n)^2)}{4\Delta x^2} \simeq 5\mu m \tag{8.5}$$

in good agreement with those observed in figure 8.6 (c).

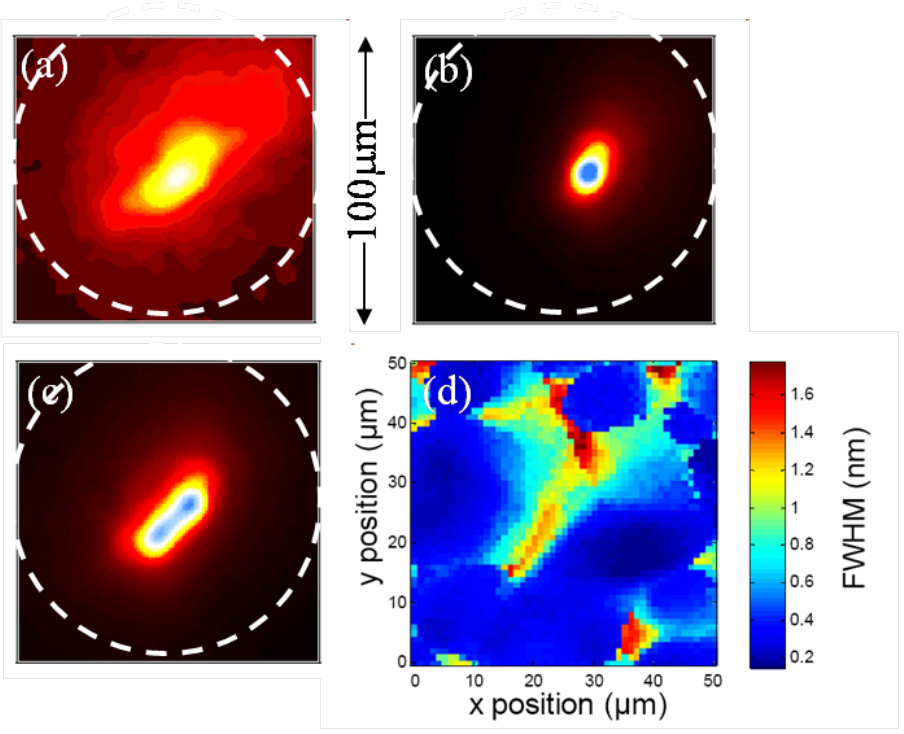

FIGURE 8.8: Time integrated images of the spatial distribution of the polariton emission, just below (a) and just above threshold (b,c). The dashed white line indicates the position of the excitation laser spot. Notice that in (c) multiple emission centres are present. Micro-transmission maps of the cavity mode linewidth of a GaN bulk microcavity (d) recorded by Gabriel Christmann at EPFL.

8.5 Momentum Distributions

In order to study the buildup of the emission and observe the collapse in k-space, we perform angularly resolved detection for different incident pump powers without moving either sample or pump laser focus. The integrated intensities on each branch are extracted when pumping below, at, and above the threshold (fig 8.9). Similar results are gained when imaging the momentum space emission (fig 8.10). There is a k-space emission reduction down to HWHM $\Delta\theta = 5^o$ on passing through the threshold, as expected for polariton lasing. Surprisingly, below threshold the total emission from all branches is independent of emission angle (dashed lines) and no obvious bottleneck in polariton relaxation at high k is observed in contrast to III-V and II-VI microcavities. This implies that at 300 K in GaN, phonon, exciton-exciton, and exciton-electron scattering can efficiently populate the branches giving rapid thermalization [84][13]. For near normal incidence polaritons the exponential increase can once again be seen. The expected

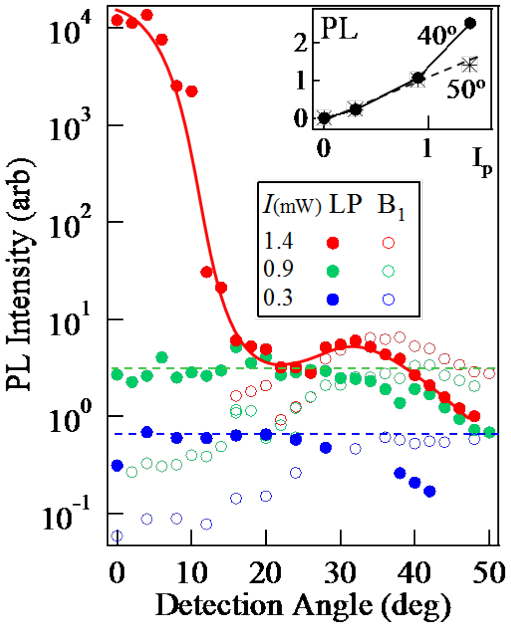

FIGURE 8.9: Extracted PL integrated intensities vs detection angle on the lower polariton branch (LP, solid points) and subsidary Bragg mode (B_1) at three inpu powers, 0.3, 0.9 and 1.4mW. Reproduced from [75].

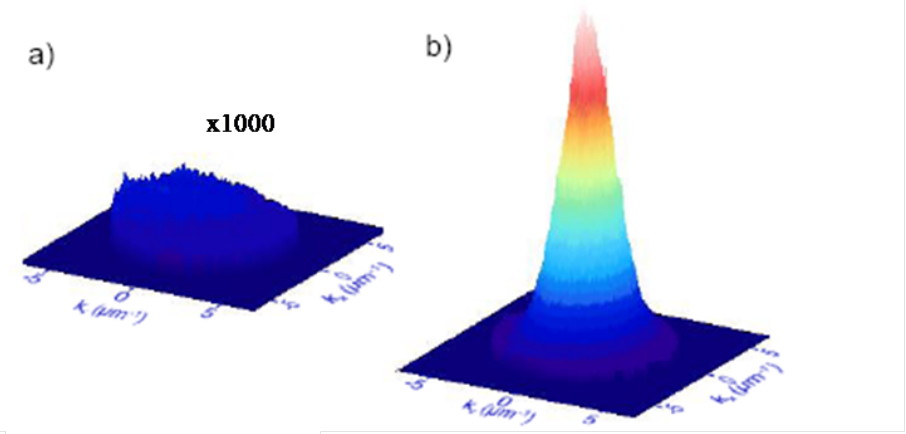

FIGURE 8.10: Formation of polariton lasing at in-plane wavevectors up to 7 μm^{-1} for (a) just below and (b) just above threshold.

bottleneck position of $\sim 40^o$ shows a quadratic increase in population (fig 8.9 inset), whereas the exciton popoulation, accessed at angles $\gg 50^o$ shows a linear relationship.

8.5.1 Conversion of Measured Intensity to Polariton Occupation

The issue of conversion from emission intensities measured at a specific angle of emission, and the polariton population at the equivalent in-plane momentum differs from that

now accepted for quantum well polaritons with CW excitation [85]. There are two reasons for this: the emission originates from bulk polaritons, and it occurs in a pulsed regime. In general, the exciton-polariton radiative life-time, τ, in a microcavity is given by $\tau^{-1} = |C|^2\tau_{ph}^{-1} + |X|^2\tau_{ex}^{-1}$, where C and X are the photon and exciton Hopfield coefficients respectively, and τ_{ph} and τ_{ex} are the lifetimes of a purely photon and exciton mode respectively.

In a CW measurement, polaritons leak out through the Bragg mirrors at a certain rate set by this polariton lifetime. Hence the intensity at each angle has to be normalised by the appropriate photon lifetime to get the average polariton occupation.

(a) For *pulsed* emission that is fast compared to the non-radiative lifetime in the sample, the use of the polariton photon fraction to convert intensities into populations is incorrect. Our time resolved measurements (Section 8.3) showed that the non-radiative lifetime of excitons in this sample is 35ps. On the other hand, the radiative lifetime of polaritons is much faster, on the order of <1ps for the states of interest here. Hence excitons at high k which are scattered into the polariton region of the dispersion near $k = 0$ are emitted before non-radiative decay occurs. Hence for each incident pump pulse, the *time-integrated emission* at a particular angle is proportional to the total polariton population at that angle. This is different to a CW experiment in which polaritons scatter into and out of particular states and the competitiion with non-radiative recombination gives rise to the need for a normalisation factor proportional to the photon lifetime.

(b) On the other hand the radiative exciton lifetime is different for bulk and QW excitons. In the bulk microcavity case τ_{ex} is comparable with τ_{ph} because both are dependent on the overlap of delocalised states inside the cavity with the continuum photon modes outside the cavity. The photon lifetime depends on the overlap of the cavity photon mode with the external photon continuum, while the exciton lifetime depends on the overlap of the exciton wavefunction which exists throughout the bulk semiconductor cavity with the same external photon continuum. Hence these lifetimes are similar in bulk microcavities, compared to QW microcavities in which the photon lifetime is considerably shorter

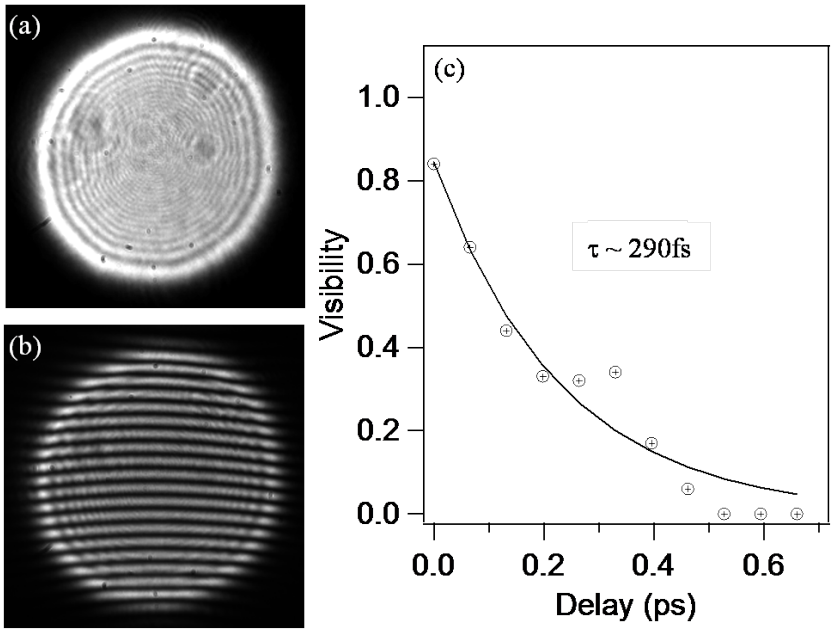

FIGURE 8.11: Interference of far-field emission cone through a slightly misaligned Michelson interferometer to show the high spatial coherence from the fringe visibility below (a) and above (b) threshold. Fringes can be seen for delays of up to 700fs, the coherence lifetime is measured to be 290fs (c)

The observed angular distribution of intensity thus directly reflects the polariton occupation along the dispersion. A further complication is the angular tuning of the stop band of the upper dielectric mirror, which means that by 50 degrees, DBR Bragg modes come into resonance with excitons 8.3. For this reason we restrict the analysis of the polariton occupation below 30 degrees when the polaritons are well formed.

8.6 Coherence Measurements

A Michelson inteferometer is used to show that the emission is first order coherent. Two copies of the collimated far-field light are interfered in the interferometer, as described in chapter 5.3.2. The resulting interference patterns are shown in figure 8.11 (a,b) for different time delays between the arms. Fringes are seen for time delays up to ∼700 fs between the paths, figure 8.11 (c), matching the ultra-short emission lifetime, indicating first order coherence.

The visibility of the measured first order coherence is found to be around 90% above threshold, where the coherence lifetime is found to be 290fs. Below threshold the visibility for $\Delta\tau = 200$fs decreases to zero, however the precise systematics of this are unreliable because around threshold fluctuations in the laser power and exact sample emission spot are exponentially enhanced. This coherent lifetime is of the same order as that expected from the emission linewidth above threshold.

The maximum fringe visibility of $\sim 90\%$ directly reflects the Onsager criterion [86] for polaritons:

$$\frac{\langle \psi^{+}(\overrightarrow{r})\psi(\overrightarrow{r}')\rangle}{\langle \psi(\overrightarrow{r})\rangle^{+} \cdot \langle \psi(\overrightarrow{r}')\rangle} \rightarrow 1 \tag{8.6}$$

By looking at the visibility from a small area of the far field emission it averages r and r' over the whole micron-sized emitting regions of the sample, demonstrating the presence of a macroscopic coherent phase. The temporal decay of this coherence is dominated by the sub-ps emission time of the condensate.

This confirms that each above-threshold spot emits fully first order coherent light. The direct imaging of the spatial coherence *within* the emiting spots has not been possible because over time, the far field pattern wobbles around slowly on a 100ms timescale. This is coincident with a degradation of the emission over time. This is thought to be to a combination of micron scale movements of the sample/pump focus as well as UV damage caused to the $Si-3N_4$ in the top DBR mirror.

8.7 Polarisation Studies and BEC

In 2006 BEC of exciton-polaritons in a microcavity was demonstrated at temperatures up to 40 K [2]. The existence of polariton BEC was proved through four experimental criteria:

1. angle-resolved photoluminescence (PL) demonstrated polariton relaxation to thermal equilibrium;

2. at the critical pumping density, a superlinear increase of population of the lowest energy polariton state was detected;

3. above threshold the cavity emission became first-order coherent;

4. above threshold the linear polarisation of the emission built up to 85%.

The data shown previously in this chapter to prove polariton lasing implies macroscopic population of the lowest energy polariton state emission of coherent light by this state, so that the BEC criteria (2, 3) are fulfilled. Also, the angle-dependent emission below and above threshold which was shown to have a warm thermalised distribution, fulfilling criterion (1). In this section the build-up of polarisation of the polariton condensate above the lasing threshold is demonstrated which fulfils criterion (4).

The anisotropy of the polariton-polariton interaction in the CdTe system means that the minimum energy for the condensate is reached when $|\psi_\uparrow| = |\psi_\downarrow|$, corresponding to a linearly polarised condensate [87]. The relative phase of the two condensate components is however not fixed, which means that the orientation of the linear polarisation should be randomly chosen by the system for each experiment. However, in the experiment of Kasprzak *et al* the linear polarisation orientation was found to be pinned to the crystallographic axes [88] and did not show that randomness expected of a BEC. In this respect, polariton condensates achieved in the CdTe system do not exhibit a departure from the polarisation orientation of the laser. A similar pinning of linear polarisation has been later observed by Balili *et al* who studied the exciton-polariton BEC in spatial traps [14]. The polarisation build-up observed in these experiments thus cannot be considered as a definite proof of spontaneous symmetry breaking.

To avoid polarisation pinning which is likely to occur in quantum wells due to their reduced symmetry, the cavity under investigation in this chapter is composed of *bulk* GaN, whose mixed excitons mean the exciton-exciton interaction is expected to be isotropic [89]. This means that polariton BEC in such cavities should be commensurate with the spontaneous appearance of completely arbitrary polarisation.

Initial experiments designed to measure the time integrated polarisation of the microcavity emission showed that it is exactly zero, independent of the orientation of the

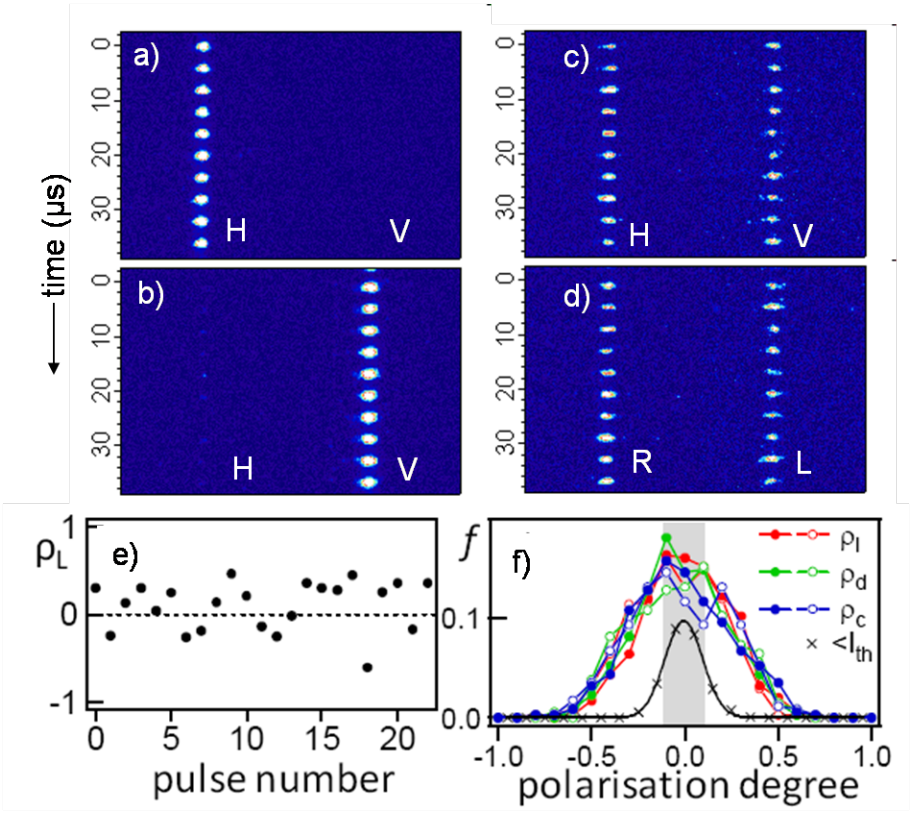

FIGURE 8.12: Characetisation of the pulse-by-pulse polarisation experiment using UV laser in horizontal and vertical polarisations. (a,b) Above-threshold polarisation-resolved emission of the condensate when analysing along (c) H/V and (d) R/L bases. (e) Extracted linear polarisation degree showing stochastic variation from pulse to pulse. (f) Histogram of the polarisation state along linear, diagonal and circular bases of nearly 2000 polariton condensates. Open and closed circles show repeated measurements with reversed polarisation split (e.g. H/V and V/H), while crosses show below-threshold unpolarised emission statistics (within detection sensitivity shaded grey). Reproduced from [90].

analyser axes. This is in contrast to polarisation measurements peformed on nitride vertical cavity surface emitting lasers (VCSELs) having similar mirrors to our structure but with InGaN/GaN quantum well active region, as described in section 4.3, which show the VCSEL emission is linearly polarised, along the crystallographic axes (fig 8.13).

In order to investigate the time averaged unpolarised emission further an experiment was designed to resolve the polarisation of the emission of the microcavity for every condensate formed by successive excitation pulses. The setup is detailed in section 5.4, the emission is split into two orthogonal polarisations and focussed into either

1. the input slit of a Streak Camera operated in single-shot mode.

2. the cathode of balanced PMTs.

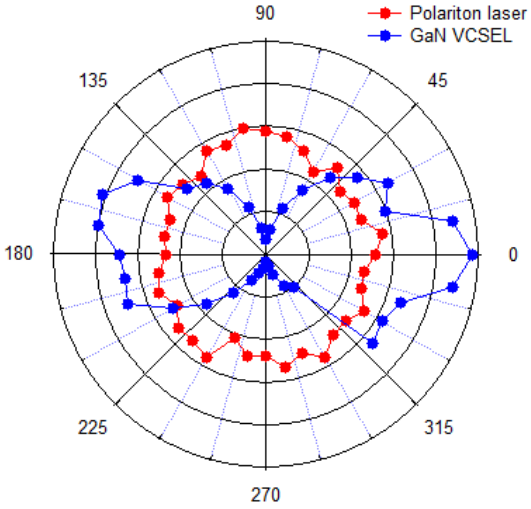

FIGURE 8.13: Emission vs. linear analyser angle for time integrated polarisation of the optically-pumped InGaN QW VCSEL (red) detailed in Section 4.3, and the bulk GaN microcavity laser (blue). This demonstrates the linearly polarised emission of the VCSEL compared to the unpolarised output of the polariton laser.

Using appropriate waveplates the polarisation of each pulse along linear (H,V), diagonal (D,$\overline{D}$) and circular (R, L) bases can be measured. These measurements are calibrated using a linearly polarised pump laser (fig 8.12), for different orientations of the input $\lambda/2$ plate, and is better than 95%. Comparable data taken over 35 μs from the microcavity above threshold is shown in figure 8.12 revealing that each BEC has a different polarisation. The intensity of each polarisation component is extracted and used to calculate the linear polarisation degree

$$\rho_l = \frac{I_H - I_V}{I_H + I_V}, \tag{8.7}$$

with the equivalent measures for diagonal ρ_d and circular ρ_c bases, figure 8.12. To ensure that no experimental artefacts are present in the data the polarisation axes are reversed on the detectors (for instance swapping H and V) and they do indeed produce exactly equivalent results. A histogram is formed by repreating the experiment many hundreds of times in each polarisation basis, figure 8.12. The BEC emission is found to be instantaneously elliptically polarised, with no preferential orientation. The magnitude of the mean polarisation is 25% for each basis, giving a total mean polarisation $\langle\rho\rangle \sim 43\%$ just above threshold. It might be thought that $\langle\rho\rangle$ measured for a single shot should be

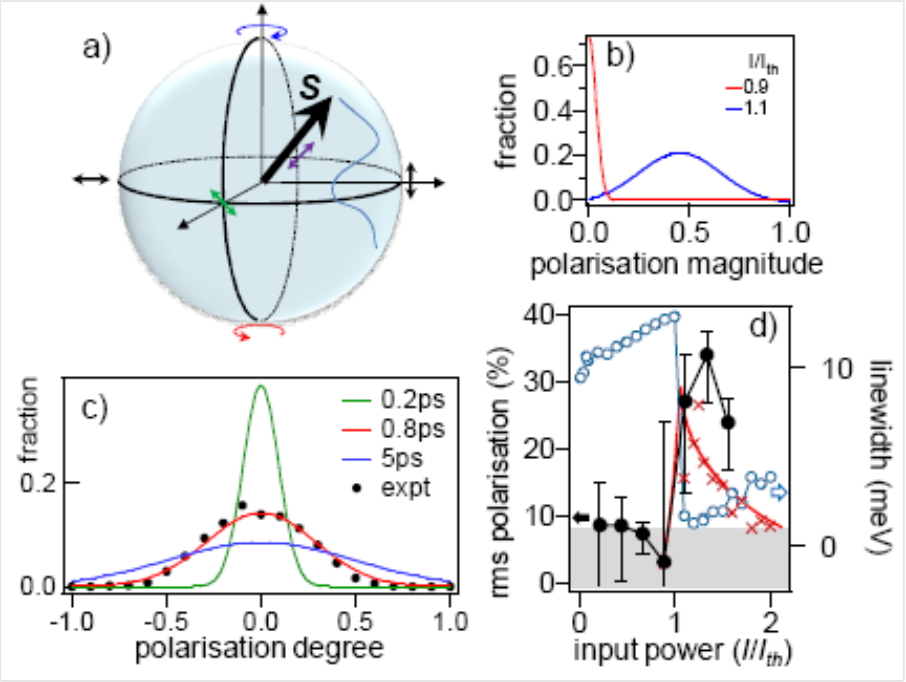

FIGURE 8.14: (a) Random evolution of the pseudospin, S (Stokes vector) of a polariton condensate inside the Poincare sphere is characteristic for the order parameter dynamics in a finite size bosonic system. (b) Above threshold, the magnitude of the pseudospin vector becomes finite. (c) Statistical distribution of the polarisation degree of the condensate showing experiment vs theory for different dephasing times. (d) Root mean square (rms) polarisation degree increases from zero (within detection error, shaded grey) to a maximum just above threshold before decreasing again. The crosses show the result of theory described in the text (red line is guide to eye), using linewidth (blue) as input parameter. Reproduced from [90].

100%, however the random walk of the polarisation vector on a time scale given by the coherence time of the condensate means that $\langle\rho\rangle < 100\%$.

In order to reproduce the experimental polarization histogram, Malpuech and Kavokin [90] performed a Monte Carlo simulation of the microcavity emission. Their model is analogous to the classical Heisenberg spin model [91] used to describe the magnetization in ferromagnets. At any moment of time the condenstae is assumed to be completely polarized but the direction of its pseudospin, **S**, on the poincare sphere, (fig 8.14) is random. The pseudospin has a probability to change its direction which is inversly proportional to the coherence time of the condensate t_c which when formed, is given by the inverse of the linewidth. If this coherence time is shorter or comparable with the emission time, it reduces the total measured polarisation degree well below 100%. The coherence time is given by [92]:

$$t_c = \left(\frac{W_{in}}{N_0 + 1} + \frac{1}{t_i} \right)^{-1}, \tag{8.8}$$

where W_{in} is the time-dependent spontaneous scattering rate towards the ground state. Both W_{in} and N_0 are calculated using the Boltzmann equations describing polariton relaxation [93] which produces the theoretical polariton distributions in figure 8.14, Appendix B gives more detail on this model. The dephasing time t_i is governed by the fluctuation of the number of polaritons in the system. In case of *cw* pumping $t_i \approx \frac{\hbar}{V\sqrt{N}}$ where V is the matrix element of interparticle interactions and N the average number of particles.

To reproduce the experiment with pulsed excitation the polarized emission of the ground state is averaged for 100 ps after after each pulse and the numerical experiment is repeated 10^5 times. The spontaneous build-up of polarisation is clearly observed above threshold (fig 8.14 (b,d)). The dephasing time used in the calculation is directly taken from the linewidth measurements (fig 8.14 (d)). Examining the polarisation histograms (fig 8.14 (c)) shows that the best fit is indeed obtained for $t_i = 0.8$ ps (corresponding to the resolution-limited 0.82meV linewidth). Below threshold, the residual polarisation is below the detection limit of our setup, while it increases to a maximum at threshold (fig 8.14 (d)), before decreasing again because of the shortening of the coherence time, probably due to stronger polariton-polariton interactions [94].

8.8 Second Lasing Threshold

Recent discussions in the literature [95] have stressed the desireability of demonstrating that the strong-weak coupling transition occurs at higher polariton density than the polariton lasing threshold, and also of showing a separate lasing transition at even higher powers. This has only recently been achieved for the same spot on the sample for microcavities which have been patterned into pillars [95].

For the GaN wafers here, the main problem is that of the dielectric mirror degradation noted above. For this reason it is not possible to directly show higher pump power emission, and track the appearance of a strong-weak coupling transition.

8.9 Chapter Summary

In summary, the emission of a hybrid bulk GaN microcavity has been investigated at $T = 300K$ under pulsed nonresonant excitation. The observation of a low-threshold coherent emission, and the emission line blueshift due to polariton-polariton interactions, demonstrates the first room-temperature polariton lasing. Further to this, polarisation studies showed that the phase coherent state of bosonic exciton-polaritons in GaN which form a above a charactersitic density, exhibit spontaneous symmetry breaking at room temperature. The coherent polariton state thus fulfils all the criteria to be classed as BEC.

Chapter 9

Conclusions

This thesis has investigated the temporal and spatial properties of microcavity-polaritons at liquid helium temperatures and polariton lasing and BEC at room temperature. Microcavity exciton polaritons are the result of strong coupling between excitons and photons inside a lambda sized cavity. These polaritons are quasi-bosons and have a unique dispersion that acts as a trap in momentum space. This interesting dispersion, coupled with the stimulated scattering inherent from boson statistics makes the semiconductor microcavity a superb system for studying phenomena such as optical parametric oscillation and Bose-Einstein condensation. Research in this field is motivated by both the fundamental physics and the potential for technological applications.

The recovery dynamics of a microcavity optical parametric oscillator have been studied. The OPO was set running in steady-state operation before a laser pulse perturbed the system. It was found that under resonant and non-resonant perturbation of the pump state, the primary feature of the dynamics was a decrease in signal emission intensity. A theoretical model was constructed describing the three OPO states including effects such as self interaction. In the case of resonant perturbation the dynamics were too fast to resolve experimentally, however it was clear that the perturbation resulted in a reduction in signal intensity. In accordance with the theoretical work of Whittaker [65] our experimental data and model showed that the main contribution to the observed dynamics was a blue shift of the lower polariton branch which resulted in the OPO moving out of resonance, turning it off.

Experiments exploring non-resonant perturbation, where the perturbation was used to populate an exciton reservoir, showed recovery timescales < 1 ns, a timescale never reported in regards to the microcavity OPO. The theoretical model was adapted to include a fourth state to described this exciton reservoir. The low coupling efficiency of the kick to the excitons meant that the blueshift did not destroy the OPO resonance condition. However it was shown that this smaller blueshift changed the coupling efficiency between the pump laser and the pump OPO state. An blueshift-dependent overlap factor was introduced to the model to describe this effect. This model repreoduced the trends shown in the experimental data. It was then shown experimentally that by changing the energy of the pump laser, one could increase or decrease the OPO emission for > 1 ns upon perturbation.

Experiments were performed to explore the spatio-temporal dynamics of the perturbed OPO. An experiment was built that combined a streak camera with an imaging system to produce spatio-temporal movies with a time resolution $\sim$5 ps. The dynamics were found to vary significantly within the excitation spot. Some areas showed a reduction in signal intensity while others an increase upon perturbation. The real space overlap of the pump and kick spot was found to have the most significant effect on the dynamics, with disorder also playing a role. Theoretical modelling of the spatio-temporal dynamics is beyond the scope of this thesis, however comparisons with the spatially integrated model showed that they qualitatively agree.

A hybrid bulk GaN microcavity was investigated at room temperature. The observation of a low-threshold coherent emission, and the blue shift of the emission line due to polariton-polariton interactions, demonstrated the first room-temperature polariton laser. Further to this, polarisation studies showed that the phase coherent state of bosonic exciton-polaritons in GaN which form above a characteristic density, exhibit spontaneous symmetry breaking at room temperature. The coherent polariton state thus fulfills all the criteria to be classed as BEC. This is the first report of BEC at room temperature.

Now that polariton lasing has been demonstrated at room temperature, future work should focus on achieving the same results using electrical rather than optical injection.

This will pave the way for a new breed of low power opto-electronic devices operating at blue wavelengths.

Appendix A

Hamiltonian of the Optical Parametric Oscillator

The equations used in Chapter 6 for the microcavity optical parametric amplifier were obtained using the following procedure, proposed by Ivan Shelykh:

We restrict our consideration to a three level model (signal s, pump p, and idler i). The model Hamiltonian can be written as:

$$\begin{aligned} H =&(\epsilon_s p_s^+ p_s + \epsilon_p p_p^+ p_p + \epsilon_i p_i^+ p_i) \\ &+ U(X_s p_s^+ p_s + X_s p_p^+ p_p + X_i p_i^+ p_i)(X_s p_s^+ p_s + X_s p_p^+ p_p + X_i p_i^+ p_i) \\ &+ V(p_p^+ p_s^+ p_s p_i + p_p p_s p_s^+ p_i^+) \end{aligned} \tag{A.1}$$

where the first term describes free particles, the second term describes blue shifts (X is the exciton fraction of each of the states), the third term corresponds to the parametric process. The coupling terms U and V are related by V$\simeq X_p\sqrt{X_i X_s}U$. The dynamics of the system can be described by the Liouville equation for the density matrix:

$$i\hbar\frac{d\rho}{dt} = [H;\rho] \tag{A.2}$$

so that for the occupation numbers we have:

$$\begin{aligned}\frac{dN_s}{dt} =& Tr\left(\frac{d\rho}{dt}\right) \\ =& \frac{i}{\hbar} Tr(p_s^+ p_s[\rho : H]) \\ =& -\frac{N_s}{\tau_s} + \frac{2}{\hbar} Im\left\{V\langle p_s^+ p_i^+ p_p p_p\rangle\right\} \\ =& -\frac{N_s}{\tau_s} + \frac{2}{\hbar} IM\left\{VC\right\},\end{aligned} \tag{A.3}$$

where $C = \langle p_s^+ p_i^+ p_p p_p\rangle = Tr(p_s^+ p_i^+ p_p p_p \rho)$ and we have added the polariton lifetime τ. Equation A.3 is exact, no decoupling has been performed.

Equivalent equations for the idler and pump can be written:

$$\frac{dN_i}{dt} = -\frac{N_i}{\tau_i} + \frac{2}{\hbar} IM\left\{VC\right\}, \tag{A.4}$$

$$\frac{dN_p}{dt} = -\frac{N_p}{\tau_i} - \frac{4}{\hbar} IM\left\{VC\right\} + F, \tag{A.5}$$

where for the pump state we have added an external pumping term F.

Calculating the mean value for the commutator $[H;\rho]$ with a product of four operators $p_s^+ p_i^+ p_p p_p$, one obtains the equation for the fourth-order non classical correlator C which governs the dynamics. If we proceed in this way we will obtain the infinite chain of the Bogolubov equations for correlators. Practically, we need to cut this at some point. We choose to decouple at the sixth order correlator and split this into the product of three second order, which in our case are just occupation numbers of the states (mean field approximation). Using this procedure one gets:

$$\begin{aligned}\frac{dC}{dt} =& -\left(\frac{1}{2\tau_s}+\frac{1}{2\tau_i}+\frac{1}{\tau_p}\right)C \\ &+\frac{i}{\hbar}\left[(\epsilon_s+\epsilon_i-2\epsilon_p)+U(X_i+X_s-2X_p)(X_iN_i+X_sN_s+X_pN_p)\right]C \\ &+\frac{iV}{\hbar}\left[N_p^2(N_s+N_i+1)-4N_sN_i(N_p+1)\right]\end{aligned} \tag{A.6}$$

without the blue shift term the system of equations (A.3)-(A.5) is just a damped non-linear oscillator. If in the regime of the continuous pump the resonance is reached (i.e. the second term in Eq (A.3) is minimised), then Equation (A.3) can be rewritten as:

$$\begin{aligned}\frac{dC}{dt} =& -\left(\frac{1}{2\tau_s}+\frac{1}{2\tau_i}+\frac{1}{\tau_p}\right)C \\ &+\frac{i}{\hbar}U(X_i+X_s-2X_p)\left[X_i(N_i-N_{i0})+X_s(N_s-N_{s0})+X_p(N_p-N_{p0})\right]C \\ &+\frac{iV}{\hbar}\left[N_p^2(N_s+N_i+1)-4N_sN_i(N_p+1)\right]\end{aligned} \tag{A.7}$$

where N_0 are the steady state solutions.

Appendix B

Boltzmann Equations for Polariton Relaxation

The polariton relaxation in the case of a pulsed non-resonant optical pumping can be described using the quantum Boltzmann kinetic equations, which allows for bosonic stimulation, pumping, finite lifetime and all kinds of relevant scattering mechanisms. The polariton dispersion curve in bulk GaN is quite complex and includes up to 6 branches [85]. However, GaN cavities are characterized by an inhomogeneous broadening, which mixes all the intermediate polariton branches. For the room temperature simulations two relevant branches of the dispersion have been included in our kinetic simulations: The lower polariton branch which has a photon like 2D dispersion near its bottom and the excitonic-like branch which is characterised by a 3D density of states.

Electron-hole pairs are created by short optical pulses of the excitation source at a relatively high energy. They rapidly relax through their strong interaction with LO phonons to form a cloud of excitons. In the pulsed excitation regime, the input of the simulation is given by the initial distribution of excitons and polaritons which is assumed to follow a Boltzmann distribution with the effective temperature dependent on the energy of LO phonons (92 meV in our case). We then solve a system of quantum Boltzmann equations [12], which reads:

$$\frac{dn_k}{dt} = -\Gamma_k n_k - n_k \sum W_{k\to k'}(n_{k'}+1) + (n_k+1)\sum W_{k'\to k} n_k \tag{B.1}$$

where n_k is the occupation number of a state with wave-vector k, $\Gamma_k n_k$ terms describe pumping and decay of particles, and $W_{k\to k'}$ are the scattering rates between the states with wave-vectors k and k'. We assume a cylindrical symmetry for the exciton and polariton distribution functions, while a full eave-vector conservation is properly accounted for in each intra- and inter-branch scattering processes. The scattering rates are calculated using the Fermi Golden Rule considering exciton-phonon, exciton-exciton and exciton-electron interaction. The inhomogeneous broadening of the polariton line is taken into account while calculating the scattering rates. We account for the three most essential mechanisms of interaction of excitons with the crystal lattice in GaN, which are [96]: The Froehlich interaction (LO phonons), the deformation potential and the piezoelectric field(acoustic phonons). The exciton-exciton and exciton-electron interactions have been considered within the Born approximation. For the exciton-exciton interaction in bulk we have taken the constant of the paraexciton interaction [97], while for the exciton-electron interaction the matrix element in the Born approximation has been calculated in [82]. A free electron density of 2 x 10^{16} cm^{-3} has been considered, in agreement with the experimental data on the residual n-doping in such structures. These simulations allow extraction of the time dependence of the polariton distribution function *vs* pumping power [92], which can be directly compared to the experimental data and used to perform our Monte Carlo modeling describing the polarization dynamics C.3.

Appendix C

Polarization as an Order Parameter

The build-up of spontaneous linear polarisation in quantum well microcavities has been described theoretically in [92][2]. Kavokin and Malpuech [90] have taken this work forward and used it to model the experimental data of section 8.7. This section gives a brief overview of the important theoretical concepts used in the modelling. The essential feature of a bulk microcavity is the absence of a spin quantisation axis leading to spin-isotropic polariton-polariton interactions. The condensate order parameter ψ is a two-component complex vector analogous to the Jones vector of classical light [87]. The time-dependent absolute polarisation degree of the condensate is given by $\rho = \frac{|\psi|^2}{N_0}$, where N_0 is the time-dependent occupation number of the condensate. It is linked with linear, diagonal and circular polarisation degrees ρ_l, ρ_d, ρ_c by $\rho = \sqrt{\rho_1^2 + \rho_d^2 + \rho_c^2}$. The psuedospin components S_x, S_y, S_z are linked with the polarisation degrees by $\rho_{l,d,c} = \frac{2S_{x,y,z}}{N_0}$. Extending the method by [98], the probability of realisation of a given value of the order parameter at a given time $P(\psi, t)$ is described by a non-linear Fokker-Planck equation:

$$\frac{\partial P}{\partial t} = \nabla[P\nabla U(\psi, t) + D(t)\nabla P] \tag{C.1}$$

where the effective potential is given by

$$U = \frac{1}{4}\left\{[W_{out}(t) - W_{in}(t)]|\psi|^2 + \alpha|\psi|^4\right\}, \tag{C.2}$$

and the diffusion coefficient is equal to $D = \frac{1}{4}W_{in}(t)$. Here $W_{in}(t)$ is the rate of scattering-in of exciton-polaritons into the condensate which is dependent on the pumping strength and the coupling efficiency of the condensate with a reservoir of exciton polaritons having large wave-vectors. W_{out} is the depletion rate of the condensate depending mostly on the polariton radiative lifetime. $\alpha > 0$ is the polariton-polariton interaction constant. The population of the condensate N_0 is linked to $W_{in}(t)$ and $W_{out}(t)$ via the Boltzmann equation:

$$\frac{dN_0}{dt} = W_in(t)(N_0 + 1) - W_{out}(t)N_0, \tag{C.3}$$

Above threshold, $W_{in} > W_{out}$ so that the potential [99] has a maximum at $|\psi| = 0$. This allows for an efficient diffusion of the order parameter out of the centre of the effective potential. The build-up of the order parameter results in the polarisation build-up. The resulting value of the absolute polarisation is linked to the minimum of the effective potential [99], which has no privileged polarisation, so that in each experiment the system chooses its polarisation randomly. Once formed the polraisation continues changing due to the diffusion of the order parameter within the effective potential.

Bibliography

[1] H. Deng, G. Weihs, D. Snoke, J. Bloch, and Y. Yamamoto. Polariton lasing vs. photon lasing in a semiconductor microcavity. *Proc. Natl. Acad. Sci. U.S.A*, 100:15318, 2003.

[2] J. Kasprzak, M. Richard, S. Kundermann, A. Baas, P. Jeambrun, J. M. J. Keeling, F. M. Marchetti, M. H. Szyman acuteska, R. Andr, J. L. Staehli, V. Savona, P. B. Littlewood, B. Deveaud, and Le Si Dang. Boseeinstein condensation of exciton polaritons. *Nature*, 443:409, 2006.

[3] T. C. H. Liew, I. A. Shelykh, and A. V. Kavokin. Optical circuits based on polariton neurons in semiconductor microcavities. *Phys. Rev. Lett.*, 101:016402, 2008.

[4] K. Huang. *Proc. Roy. Soc. London*, A208:352, 1951.

[5] J. J. Hopfield. Theory of the contribution of excitons to the complex dielectric constant of crystals. *Phys. Rev.*, 112:1555, 1958.

[6] D. Frohlich, E. Mohler, and P. Wiesner. Observation of exciton polariton dispersion in cucl. *Phys. Rev. Lett.*, 26:554, 1971.

[7] C. Weisbuch and R. G. Ulbrich. Resonant polariton fluoresence in gallium arsenide. *Phys. Rev. Lett.*, 39:654, 1977.

[8] C. Weisbuch, M. Nishioka, A. Ishikawa, and Y. Arakawa. Observation of the coupled exciton-photon mode splitting in a semiconductor quantum well microcavity. *Phys. Rev. Lett.*, 69:3314–3317, 1992.

[9] A. Imamoglu, R. J. Ram, S. Pau, and Y. Yamamoto. Nonequilibrium condensates and lasers without inversion: Exciton-polariton lasers. *Phys. Rev. A*, 53(6):4250–4253, 1996.

[10] P. G. Savvidis, J. J. Baumberg, R. M. Stevenson, M. S. Skolnick, D. M. Whittaker, and J. S. Roberts. Angle-resonant stimulated polariton amplifier. *Phys. Rev. Lett.*, 84(7):1547–1550, 2000.

[11] J. J. Baumberg, P. G. Savvidis, R. M. Stevenson, A. I. Tartakovskii, M. S. Skolnick, D. M. Whittaker, and J. S. Roberts. Parametric oscillation in a vertical microcavity: A polariton condensate or micro-optical parametric oscillation. *Phys. Rev. B*, 62:R16247–R16250, 2000.

[12] D. Porras, C. Ciuti, J. J. Baumberg, and C. Tejedor. Polariton dynamics and bose einstein condensation in semiconductor microcavities. *Phys. Rev. B*, 66(8):085304, 2002.

[13] G. Malpuech, A. Kavokin, A. Di Carlo, and J. J. Baumberg. Polariton lasing by exciton-electron scattering in semiconductor microcavities. *Phys. Rev. B*, 65(15), 2002.

[14] R. Balili, V. Hartwell, D. Snoke, L. Pfeiffer, and K. West. Bose-einstein condensation of microcavity polaritons in a trap. *Science*, 316(5827):1007–1010, 2007.

[15] C. W. Lai, N. Y. Kim, S. Utsunomiya, G. Roumpos, H. Deng, M. D. Fraser, T. Byrnes, P. Recher, N. Kumada, T. Fujisawa, and Y. Yamamoto. Coherent zero-state and pi-state in an excitonpolariton condensate array. *Nature*, 450:529, 2007.

[16] C. Weisbuch and B. Vinter. *Quantum semiconductor structures.* Harcourt Brace Janovich, 1991.

[17] J. Frenkel. On the transformation of light into heat in solids. i. *Phys. Rev.*, 37:17, 1931.

[18] G. H. Wannier. The structure of excitation levels in insulating crystals. *Phys. Rev.*, 52:191, 1937.

[19] N. Bohr. On the constitution of atoms and molecules. *Phil. Mag.*, 26:1–25, 1913.

[20] W. W. Chow and S. W. Koch. *Seminconductor Laser Fundamentals: Physics of the Gain Materials*. Springer-Verlag, 1999.

[21] G. Bastard, E. E. Mendez, L. L. Chang, and L. Esaki. Exciton binding energy in quantum wells. *Phys. Rev. B.*, 26:1974–1979, 1982.

[22] R. Leavitt and J. Little. Simple method for calculating exciton binding energies in quantum-confined semiconductor structures. *Phys. Rev. B*, 42:11774, 1990.

[23] C. Priester, G. Allan, and M. Lannoo. Wannier excitons in gaas-ga(1-x)al(x)as quantum-well structures: influence of the effective-mass mismatch. *Phys. Rev. B*, 30:7302, 1984.

[24] M. Born and E. Wolf. *Principles of Optics*. Cambridge University Press, 7th edition edition, 1999.

[25] M. S. Skolnick, T. A. Fisher, and D. M. Whittaker. Strong coupling phenomena in quantum microcavity structures. *Semicond. Sci. Technol.*, 13:645–669, 1998.

[26] V. Savona, C. Piermarocchi, A. Quattropani, P. Schwindemann, and F. Tassone. Optical properties of microcavity polaritons. *Phase Trans.*, 68:169–279, 1999.

[27] F. London. The l-phenomenon of liquid helium and the bose-einstein degeneracy. *Nature*, 141:643, 1938.

[28] J. Allen and A. Misener. Flow of liquid helium ii. *Nature*, 141:75, 1938.

[29] P. Kapitza. Viscosity of liquid helium below the l-point. *Nature*, 141:74, 1938.

[30] S. A. Moskalenko. Reversible optico-hydrodynamic phenomena in a non ideal exciton gas. *Fiz. Tverd. Tela*, 4:276–284, 1962.

[31] J. T. Warren, K. E. O'Hara, and J. P. Wolfe. Two-body decay of thermalized excitons in cu_2o. *Phys. Rev. B.*, 61:8215–8223, 2000.

[32] K. E. O'Hara and J. P. Wolfe. Relaxation kinetics of excitons in cuprous oxide. *Phys. Rev. B*, 62:12909–12922, 2000.

[33] J. P. Jang. New perspectives on kinetics of excitons in cu_2o. *Sol. Stat. Comm.*, 134:143–149, 2005.

[34] M. H. Anderson, J. R. Ensher, M. R. Matthews, C. E. Wieman, and E. A. Cornell. Observation of bose-einstein condensation in a dilute atomic vapor. *Science*, 269:198, 1995.

[35] K. B. Davis, M. O. Mewes, M. R. Andrews, N. J. van Druten, D. S. Durfee, D. M. Kurn, and W. Ketterle. Bose-einstein condensation in a gas of sodium atoms. *Phys. Rev. Lett.*, 75(22):3969, 1995.

[36] C. C. Bradley, C. A. Sackett, J. J. Tollett, and R. G. Hulet. Evidence of bose-einstein condensation in an atomic gas with attractive interactions [phys. rev. lett. 75, 1687 (1995)]. *Phys. Rev. Lett.*, 79(6):1170, 1997.

[37] A. Griffin, D. W. Snoke, and S. Strinari. *Bose-Einstein Condensation.* Cambridge University Press, 1995.

[38] L. Pitaevskii and S. Stringari. *Bose-Einstein Condensation.* North-Holland, 1974.

[39] A. V. Kavokin, J. J. Baumberg, G. Melpuech, and F. P. Laussy. *Microcavities.* Oxford Science Publications, 2007.

[40] N. Bogolubov. On the theory of superfluidity. *J. Phys.*, 11:23, 1947.

[41] S. T. Beliaev. Energy-spectrum of a non-ideal bose gas. *Sov. Phys. JETP*, 34:299, 1958.

[42] L. P. Pitaevskii. Vortex lines in an imperfect bose gas. *Sov. Phys. JETP*, 13:451, 1961.

[43] A. Griffin. A brief history of our understanding of bec: From bose to beliaev. In M. Ingusicio, S. Stringari, and C. E. Wieman, editors, *Proceedings of the International School of Physics - Enric Fermi.* IOS Press, 1 edition, 1999.

[44] A. Fetter and J. Walecka. *Quantum theory of many-particle systems.* Dover, 2003.

[45] P. Littlewood, P. Eastham, J. Keeling, F. Marchetti, and M. Szymanska. Models of coferent exciton condensation. *J. Phys.: Cond. Matt.*, 16:S3597, 2004.

[46] L. Keldysh and A. N. Kozlov. Collective properties of excitons in semiconductors. *Sov. Phys. JETP*, 27:521, 1968.

[47] C. Comte and P. Nozieres. Exciton bose condensation: The ground state of an electron-hole gas i. mean field description of a simplified model. *J. Phys.*, 43:1069, 1982.

[48] G. Malpuech, Y. Rubo, F. Laussy, P. Bigenwald, and A. Kavokin. Polariton laser: thermodynamics and quantum kinetic theory. *Semicond. Sci. Technol.*, 18:S395, 2003.

[49] D. Sarchi and V. Savona. Kinetic theory of non-equilibrium condensation of microcavity polaritons. *arXiv.org:cond-mat/0411084*, 2006.

[50] G. Malpuech, A. Di Carlo, A. Kavokin, J. J. Baumberg, M. Zamfirescu, and P. Lugli. Room-temperature polariton lasers based on gan microcavities. *App. Phys. Lett.*, 81(3):412–414, 2002.

[51] P. Senellart and J. Bloch. Nonlinear emission of microcavity polaritons in the low density regime. *Phys. Rev. Lett.*, 82:1233, 1999.

[52] A. Kavokin, G. Malpuech, and F. Laussy. Polariton laser and polariton superfluidity in microcavities. *Phys. Lett. A*, 306:187, 2003.

[53] N. D. Mermin and H. Wagner. Absence of ferromagnetism or antiferromagnetism in one-or-two dimensional isotropic heisenberg models. *Phys. Rev. Lett*, 17:1133, 1966.

[54] P. Hohenberg. Existence of long-range order in one and two dimensions. *Phys. Rev.*, 158:383, 1967.

[55] I. M. Khalatnikov. *An Introduction to the Theory of Superfluidity.* New York, 1965.

[56] W. Ketterle and N. J. ven Druten. Bose-einstein condensation of a finite number of particles trapped in one or three dimensions. *Phys. Rev. A*, 54:656, 1996.

[57] M. Leroux, N. Grandjean, M. Lagt, J. Massies, B. Gil, P. Lefebvre, and P. Bigenwald. Quantum confined stark effect due to built-in internal polarization fields in (al,ga)n/gan quantum wells. *Phys. Rev. B*, 58(20):R13371, 1998.

[58] R. Butte, G. Christmann, E. Feltin, J. F. Carlin, M. Mosca, M. Ilegems, and N. Grandjean. Room-temperature polariton luminescence from a bulk gan microcavity. *Phys. Rev. B*, 73(3), 2006.

[59] G. Christmann, D. Simeonov, R. Butte, E. Feltin, J. F. Carlin, and N. Grandjean. Impact of disorder on high quality factor iii-v nitride microcavities. *App. Phys. Lett.*, 89(26), 2006.

[60] M. Richard, J. Kasprzak, R. Romestain, R. Andre, and L. S. Dang. Spontaneous coherent phase transition of polaritons in cdte microcavities. *Phys. Rev. Lett.*, 94(18), 2005.

[61] Z. Y. Ou, H. J. Pereira, and K. C. Peng. Realization of the einstein-podolsky-rose paradox for continuous variables. *Phys. Rev. Lett.*, 68:3663–3666, 1992.

[62] D. M. Whittaker. Classical treament of parametric processes in a trong-coupled planar microcavity. *Phys. Rev. B.*, 63:193305, 2001.

[63] P. G. Savvidis, C. Ciutti, J. J. Baumberg, D. M. Whittaker, and J. S. Roberts. Off-branch polaritons and multiple scattering in semiconductor microcavities. *Phys. Rev. B*, 64:075311, 2001.

[64] C. Ciuti, P. Schwendimann, and A. Quattropani. Parametric luminescence of microcavity polaritons. *Phys. Rev. B*, 63:041303(R), 2001.

[65] D. M. Whittaker. Effects of polariton-energy renormalization in the microcavity optical parametric oscillator. *Phys. Rev. B*, 71:115301, 2005.

[66] R. M. Stevenson, V. N. Astratov, M. S. Skolnick, J. S. Roberts, and G. Hill. Uncoupled excitons in semiconductor microcavities detected in resonant raman scattering. *Phys. Rev. B*, 67:081301R, 2003.

[67] D. M. Whittaker. Numerical modelling of the microcavity opo. *Phys. Stat. Sol. (c)*, 2:733, 2005.

[68] G. Malpuech, D. D. Solnyshkov, H. Ouerdane, M. M. Glazov, and I. Shelykh. Bose glass and superfliud phases of cavity polaritons. *arXiv:cond-mat/0701713v1*, 2008.

[69] A. Amo, D. Sanvitto, D. Ballarini, F. P. Laussy, del Valle. E., M. D. Martin, A. Lemaitre, J. Bloch, D. N. Krizhanovskii, M. S. Skolnick, C. Tejedor, and L. Vina. Quantum fluid dynamics of microcavity polaritons. *arXiv:0711.1539*, 2007.

[70] K. G. Lagoudakis, M. Wouters, M. Richard, A. Baas, I. Carusotto, R. Andre, Le Si Dang, and B. Deveaud-Pledran. Electron-polariton scattering in semiconductor microcavities. *Nature Phys.*, 4, 2008.

[71] D. Sanvitto, D. N. Krizhanovskii, D. M. Whittaker, S. Ceccarelli, M. S. Skolnick, and J. S. Roberts. Spatial structure of the macroscopically occupied polariton state in the microcavity optical parametric oscillator. *Phys. Rev. B*, 73:341308(R), 2006.

[72] M. S. Skolnick, D. Sanvitto, D. N. Krizhanovskii, A. P. D. Love, and Whittaker D. M. Spatial properties and coherence of the high desnity phase in the microcavity optical parametric oscillator. *Phys. Stat. Sol. (b)*, 243:3741, 2006.

[73] J. Wagner, H. Obloh, M. Kunzer, M. Maier, K. Kohler, and B. Johs. Dielectric function spectra of gan, algan, and gan/algan heterostructures. *J. App. Phys.*, 89(5):2779–2785, 2001.

[74] M. Richard, J. Kasprzak, R. Andre, R. Romestain, L. S. Dang, G. Malpuech, and A. Kavokin. Experimental evidence for nonequilibrium bose condensation of exciton polaritons. *Phys. Rev. B*, 72, 2005.

[75] S. Christopoulos, G. B. H. von Hogersthal, A. J. D. Grundy, P. G. Lagoudakis, A. V. Kavokin, J. J. Baumberg, G. Christmann, R. Butte, E. Feltin, J. F. Carlin, and N. Grandjean. Room-temperature polariton lasing in semiconductor microcavities. *Phys. Rev. Lett.*, 98(12), 2007.

[76] N. Antoine-Vincent, F. Natali, D. Byrne, A. Vasson, P. Disseix, J. Leymarie, M. Leroux, F. Semond, and J. Massies. Observation of rabi splitting in a bulk gan microcavity grown on silicon. *Phys. Rev. B*, 68(15), 2003.

[77] F. Binet, J. Y. Duboz, J. Off, and F. Scholz. High-excitation photoluminescence in gan: Hot-carrier effects and the mott transition. *Phys. Rev. B*, 60(7):4715–4722, 1999.

[78] R. A. Taylor, S. Hess, K. Kyhm, J. Smith, J. F. Ryan, G. P. Yablonskii, E. V. Lutsenko, V. N. Pavlovskii, and M. Heuken. Stimulated emission and excitonic bleaching in gan epilayers under high-density excitation. *Phys. Stat. Sol. B*, 216(1):465–470, 1999.

[79] A. E Seigman. *Lasers*. University Science Books, 1st edition edition, 1986.

[80] Y. Yamamoto, S. Machida, and G. Bjork. Microcavity semiconductor laser with enhanced spontaneous emission. *Phys. Rev. A*, 44:657, 1991.

[81] G. Bjork, H. Heitmann, and Y. Yamamoto. Spontaneous-emission coupling factor and mode characteristics of planar dielectric microcavity lasers. *Phys. Rev. A*, 47:4451, 1993.

[82] H. Haug and S. Koch. On the theory of laser action in dense exciton systems. *Phys. Stat. Sol (b)*, 82:531, 1977.

[83] K. P. Korona. Dynamics of excitonic recombination and interactions in homoepitaxial gan. *Phys. Rev. B*, 65(23), 2002.

[84] P. G. Lagoudakis, M. D. Martin, J. J. Baumberg, A. Qarry, E. Cohen, and L. N. Pfeiffer. Electron-polariton scattering in semiconductor microcavities. *Phys. Rev. Lett.*, 90(20), 2003.

[85] P. P. Paskov, T. Paskova, P. O. Holtz, and B. Monemar. Polarized photoluminescence of exciton-polaritons in free-standing gan. *Phys. Stat. Sol (a)*, 201:678, 2004.

[86] P. J. Price. Density fluctuations at low temperatures. *Phys. Rev.*, 94:257, 1954.

[87] I. A. Shelykh, Y. G. Rubo, G. Malpuech, D. D. Solnyshkov, and A. Kavokin. Polarization and propagation of polariton condensates polarization and propagation of polariton condensates. *Phys. Rev. Lett.*, 97(6), 2006.

[88] J. Kasprzak, R. Andre, L. S. Dang, I. A. Shelykh, A. V. Kavokin, Y. G. Rubo, K. V. Kavokin, and G. Malpuech. Build up and pinning of linear polarization in the bose condensates of exciton polaritons. *Phys. Rev. B*, 75, 2007.

[89] T. Aoki, G. Mohs, M. Kuwata-Gonokami, and A. A. Yamaguchi. Influence of exciton-exciton interaction on quantum beats. *Phys. Rev. Lett.*, 82(15):3108–3111, 1999.

[90] J. J. Baumberg, A. K. Kavokin, S. G. Christopoulos, A. J. D. Grundy, R. Butte, G. Christman, D. D. Solnyshkov, G. Malpuech, G. Baldassarri Hoger von Hogersthal, J. F. Feltin, and N. Grandjean. Spontaneous polarisation build up in a room temperature polariton laser. *Phys. Rev. Lett.*, 101:136409, 2008.

[91] G. S. Joyce. Classical heisenberg model. *Phys. Rev.*, 155(2):478, 1967.

[92] F. P. Laussy, I. A. Shelykh, G. Malpuech, and A. Kavokin. Effects of bose-einstein condensation of exciton polaritons in microcavities on the polarization of emitted light. *Phys. Rev. B*, 73(3), 2006.

[93] D. Solnyshkov and G. Mapuech. A polariton laser based on a bulk gan microcavity. *Superlattices and Microstructures*, 41(5-6):279–283, 2007.

[94] D. Porras and C. Tejedor. Linewidth of a polariton laser: Theoretical analysis of self-interaction effects. *Phys. Rev. B*, 67(16), 2003.

[95] P. Senellart, J. Bloch, B. Sermage, and J. Y. Marzin. Microcavity polariton depopulation as evidence for stimulated scattering. *Phys. Rev. B*, 62:R16263–R16266, 2000.

[96] X. B. Zhang and B. Gil. *Low-dimensional nitride semiconductors*. Oxford University Press, 2002.

[97] A. I. Bobrysheva, M. F. Miglei, and Shmiglyuk M. I. On the bi-exciton formation in crystals. *Phys. Stat. Sol (b)*, 53:71, 1972.

[98] Y. G. Rubo. Kinetics of the polariton condensate formation in a microcavity. *Phys. Stat. Sol (a)*, 201:641, 2004.

[99] A. Einstein. Quantum theory of ideal monoatomic gases. *Sitz. Ber. Preuss. Akad. Wiss. (Berlin)*, 22:261, 1924.